



저작자표시-비영리-변경금지 2.0 대한민국

이용자는 아래의 조건을 따르는 경우에 한하여 자유롭게

- 이 저작물을 복제, 배포, 전송, 전시, 공연 및 방송할 수 있습니다.

다음과 같은 조건을 따라야 합니다:



저작자표시. 귀하는 원저작자를 표시하여야 합니다.



비영리. 귀하는 이 저작물을 영리 목적으로 이용할 수 없습니다.



변경금지. 귀하는 이 저작물을 개작, 변형 또는 가공할 수 없습니다.

- 귀하는, 이 저작물의 재이용이나 배포의 경우, 이 저작물에 적용된 이용허락조건을 명확하게 나타내어야 합니다.
- 저작권자로부터 별도의 허가를 받으면 이러한 조건들은 적용되지 않습니다.

저작권법에 따른 이용자의 권리는 위의 내용에 의하여 영향을 받지 않습니다.

이것은 [이용허락규약\(Legal Code\)](#)을 이해하기 쉽게 요약한 것입니다.

[Disclaimer](#)

공학박사 학위논문

A novel methodology
for estimating methane emission
from waste landfills
using unmanned aerial vehicle

무인항공기를 활용한

폐기물매립지 메탄 배출량 산정 방법론 개발

2021년 8월

서울대학교 대학원

건설환경공학부

김 영 민

A novel methodology
for estimating methane emission
from waste landfills
using unmanned aerial vehicle

지도 교수 김 재 영

이 논문을 공학박사 학위논문으로 제출함

2021년 8월

서울대학교 대학원

건설환경공학부

김 영 민

김영민의 공학박사 학위논문을 인준함

2021년 8월

위 원 장 남 경 필

부위원장 김 재 영

위 원 김 승 도

위 원 이 승 목

위 원 최 정 권

ABSTRACT

A novel methodology for estimating methane emission from waste landfills using unmanned aerial vehicle

Yeong Min Kim

Department of Civil and Environmental Engineering

The Graduate School

Seoul National University

Many methods have been applied to monitor fugitive methane gas from landfills. Recently, there have been suggestions to use a framework utilizing an unmanned aerial vehicle (UAV) for landfill gas monitoring, and several field campaigns have proved that a rotary UAV-based measurement has advantages of ease of control and high-resolution concentration mapping on the target planes. Research on the application of rotary UAVs for quantifying the whole-site methane emissions from waste landfills is limited so far. This study aimed to establish the methodology as an efficient and reliable method by developing field measurements and data processing procedure, evaluating errors by potential factors, and field applications.

A measurement system composed of a lightweight methane detector and a rotary UAV, and a procedure from field measurements to data processing were

prepared. Potential error-inducing factors associated with the measurement system and the procedure were experimentally or theoretically assessed. In the detector reliability test, the methane detector had sufficient resolution for field application, and the critical UAV velocity required was obtained to ensure the credibility of the proposed measurement system. When spatial interpolators were applied to field data from the measurement system, the empirical Bayesian kriging demonstrated the best prediction of methane concentrations at unmeasured points. A wind estimation method using GPS/IMU data of UAV was also evaluated. Near-field experiments showed that the method produced wind vector estimates comparable to the wind parameters measured by a mechanical anemometer.

Field campaigns and following analysis demonstrated that it was able to successfully estimate wind vectors at multiple heights in contrast to a fixed anemometer. Estimated parameters in reasonable ranges, and explicable correlations between parameters also supported the validity of the wind estimator. Some of the evaluation results provided representative errors that were used in the comprehensive uncertainty analysis, as well as the validation of components. Multiple field campaigns were conducted at the Dangjin-si Resource Circulation Center, Dangjin, Korea. The estimated methane emission rates from seven campaigns ranged from 406.4 to 3,640 kg/ha/day, which was comparable to the emission rates modeled based on the IPCC guidelines. The total uncertainties combining effects of detection errors, interpolation errors, and wind variations were below 6 % for five cases, and below 23 % for three cases. Although the largest contributor turned out to be interpolation errors in most cases, it would be detection errors to lead to a significant reduction in the uncertainties of this methodology in the near future. There were failures in field

campaigns due to misplacement of measurement planes or weak wind, which presented practical problems in the actual applications.

This work contains a complete description of the methodology, its evaluation, and its showcases both of success and failure. Complementation by near-field, denser measurements allowed to utilize the gas analyzer of compromised performance without a great aggravation of uncertainties. We sought the improvement to the emission estimation accuracy by introducing UAV-based wind estimation method. Messages for the practical applications of the methodology could be drawn from multiple field campaigns. This study could be also useful for other UAV-based studies in the near future, especially in the current situation where UAVs are widely employed for airborne measurement or remote sensing regardless of field.

Keywords : Greenhouse gas emission; Fugitive methane emission; Unmanned aerial vehicle; Wind estimation; Uncertainty analysis

Student number : 2018-30709

This page is intentionally left blank.

TABLE OF CONTENTS

| | |
|--|-------------|
| ABSTRACT | i |
| TABLE OF CONTENTS | v |
| LIST OF FIGURES..... | ix |
| LIST OF TABLES | xiii |
| | |
| Chapter 1. Introduction | 1 |
| 1.1 Background..... | 1 |
| 1.2 Objectives | 5 |
| 1.3 Dissertation structure..... | 6 |
| References | 7 |
| | |
| Chapter 2. Literature review..... | 9 |
| 2.1 Gas transport model..... | 9 |
| 2.1.1 Gaussian dispersion model | 9 |
| 2.1.2 Advection-dispersion model | 12 |
| 2.2 Variability in fugitive emission from waste landfills..... | 16 |
| 2.3 Estimation methods for fugitive gas emission..... | 19 |
| 2.3.1 Simulation models for waste landfills | 19 |
| 2.3.2 Surface measurements of fugitive gas | 21 |
| 2.3.3 Plume measurements from fugitive sources | 23 |

| | |
|--|----|
| 2.4 Gas analyzer | 26 |
| 2.4.1 Principle of gas analyzers | 26 |
| 2.4.2 Considerations based on principles..... | 36 |
| 2.4.3 Commercially available methane analyzers | 37 |
| 2.5 Uncertainty propagation | 40 |
| References | 40 |

Chapter 3. Credibility of rotary UAV-based methane profile acquisition system.....47

| | |
|---|----|
| 3.1 Introduction | 47 |
| 3.2 Materials and methods..... | 50 |
| 3.2.1 Apparatus | 50 |
| 3.2.2 Methane detector reliability test | 51 |
| 3.2.3 Site specification of field measurement..... | 52 |
| 3.2.4 Flight mission for field measurement | 53 |
| 3.2.5 Assessment of spatial interpolation..... | 56 |
| 3.3 Results and discussion | 57 |
| 3.3.1 Reliability of measurement system..... | 57 |
| 3.3.2 Performance of the spatial interpolation models | 65 |
| 3.3.3 Methane distribution above landfill surface | 71 |
| 3.4 Summary | 72 |
| References | 73 |

Chapter 4. Assessment of wind estimation using GPS/IMU data of rotary UAV81

| | |
|---|-----|
| 4.1 Introduction | 81 |
| 4.2 Materials and methods..... | 82 |
| 4.2.1 Wind estimation using GPS/IMU of UAV | 82 |
| 4.2.2 Mechanical anemometers | 91 |
| 4.2.3 Vertical wind gradient model..... | 92 |
| 4.2.4 Comparative experiments | 92 |
| 4.3 Results and discussion..... | 95 |
| 4.3.1 Relationship between flight speed and tilt of UAV | 95 |
| 4.3.2 Comparison of wind determined by UAV and anemometer | 96 |
| 4.3.3 Vertical wind gradient by UAV-assisted wind estimation..... | 99 |
| 4.3.4 Correlation analysis | 104 |
| 4.4 Summary..... | 105 |
| References | 106 |

Chapter 5. Quantification of methane emission: Field applications and uncertainty analyses.....109

| | |
|-----------------------------------|-----|
| 5.1 Introduction | 109 |
| 5.2 Materials and methods..... | 110 |
| 5.2.1 Apparatus | 110 |
| 5.2.2 Field campaigns | 111 |
| 5.2.3 Computational methods | 113 |

| | |
|--|------------|
| 5.3 Results and discussion | 115 |
| 5.3.1 Methane captured on the measurement planes | 115 |
| 5.3.2 Methane emission rates..... | 123 |
| 5.3.3 Uncertainties in emission estimates..... | 126 |
| 5.4 Summary..... | 133 |
| References | 133 |
| Chapter 6. Conclusions | 137 |
| 국문 초록 | 141 |

LIST OF FIGURES

| | |
|---|----|
| Fig. 1.1. Dissertation structure | 6 |
| Fig. 2.1. Schematic diagram illustrating the concept of Gaussian plume model (Turner, 1994)..... | 10 |
| Fig. 2.2. Finite elements defined for deriving the numerical solution of advection- dispersion model..... | 13 |
| Fig. 2.3. Concentration profile at 200 m downwind from the source predicted by the Gaussian dispersion model and a numerical solution of the advection- dispersion model..... | 16 |
| Fig. 2.4. Methane flux maps and mean flux observed over three days, which show both temporal and spatial variations in surface methane emissions of landfills (Gonzalez-Valencia et al., 2021) | 18 |
| Fig. 2.5. Correlation between surface methane flux and concentration (Park et al., 2016)..... | 23 |
| Fig. 2.6. Concept of plume measurements and tracer dispersion method..... | 25 |
| Fig. 2.7. Plume measurement by manned aircraft in shale region (Lavoie et al., 2015) | 26 |
| Fig. 2.8. Typical electrochemical sensor setup (Chou, 2000) | 27 |
| Fig. 2.9. A typical circuit of a catalytic beads sensor (Chou, 2000)..... | 29 |
| Fig. 2.10. Typical solid-state gas sensors: (a) bead-type; and (b) chip-type (Chou, 2000)..... | 30 |
| Fig. 2.11. A basic infrared gas detector layout (Chou, 2000)..... | 32 |
| Fig. 2.12. A typical photoionization detector configuration (Chou, 2000) | 33 |
| Fig. 3.1. Numerically simulated methane concentrations in a container, supposed that | |

| | |
|---|----|
| methane is introduced at the distance zero and the time zero | 52 |
| Fig. 3.2. Summary of flight mission and detected methane concentration ranges: (a) the whole flight mission, (b) horizontal mapping mission, and (c) vertical mapping mission. The deeper color indicates the higher concentration. Actual concentrations were not reported here as they are confidential data of Landfill S, South Korea | 55 |
| Fig. 3.3. Changes in detector response for 10 min following the injection of methane into the cylindrical chamber. The relative response indicates the detector reading relative to the average readings for the final one min | 59 |
| Fig. 3.4. Detector response to (a) low and (b) high concentrations of methane in the cylindrical chamber..... | 59 |
| Fig. 3.5. Conceptual diagram of UAV-based methane measurement system at times, t and $t + \Delta t$ (UAV movement direction: x -axis)..... | 61 |
| Fig. 3.6. Cylindrical control volume of air near a propeller..... | 63 |
| Fig. 3.7. UAV velocity required to ensure the measurement credibility depending on atmospheric temperature and humidity | 64 |
| Fig. 3.8. Methane concentration profiles in a horizontal plane of $300 \text{ m} \times 300 \text{ m}$ depending on spatial interpolation methods: (a) DIB; (b) EBK; (c) GPI; (d) IDW; (e) LPI; (f) RBF; (g) EBK-standard error; and (h) LPI-standard error. The colors indicate methane concentrations. The concentrations are presented in relative values as they are the confidential data of Landfill S, South Korea..... | 69 |
| Fig. 3.9. Methane concentration profiles in a vertical plane that was 50 m high and 800 m long depending on spatial interpolation methods: (a) DIB; (b) EBK; (c) GPI; (d) IDW; (e) LPI; (f) RBF; (g) EBK-standard error; and (h) LPI-standard error. The colors indicate methane concentrations. The concentrations are presented in relative values as they are the confidential data of Landfill S, South Korea..... | 70 |

| | |
|---|-----|
| Fig. 4.1. The relationship between ground, flight, and wind vectors..... | 84 |
| Fig. 4.2. The concept of pitch, θ (a) and roll, φ (b) of a UAV. The hexagon represents a UAV advancing in the direction of the red arrow..... | 84 |
| Fig. 4.3. The concept of total tilt, ψ (a) and direction of total tilt, λ (b) of a UAV. The hexagon represents a UAV advancing in the direction of the red arrow ... | 86 |
| Fig. 4.4. Three types of forces imposed on a UAV flying to the left | 87 |
| Fig. 4.5. Theoretically expected relation between horizontal speed and tilt of a UAV | 89 |
| Fig. 4.6. Excerpt of the MATLAB code run for data pretreatment in advance to wind vectors calculation..... | 90 |
| Fig. 4.7. Excerpt of the MATLAB code for wind vectors calculation | 91 |
| Fig. 4.8. UAV flight trajectory (yellow line) and Davis installation position (red circle) for preliminary experiments on the Google satellite image | 93 |
| Fig. 4.9. Wind measurement locations in the satellite image of the field campaign site. Yellow solid lines include flight trajectories of UAV, and red arrows on vertical sticks indicate the locations for Davis..... | 94 |
| Fig. 4.10. Flight velocity at varying tilt of the UAV resulted from near-field experiments with the UAV and Davis | 96 |
| Fig. 4.11. Time variance in wind speed (a) and wind direction (b) determined by UAV-based estimation and Davis anemometer | 97 |
| Fig. 4.12. Wind rose measured by Davis (a) and estimated by UAV-based method (b) in near-field experiments..... | 98 |
| Fig. 4.13. Wind speed at different heights and Hellman exponent, α : (a) 2020 0219 am; (b) 2020 1021 am; (c) 2020 1021 pm; (d) 2020 1020 pm; (e) 2019 0416 pm; and (f) 2020 0218 pm..... | 100 |
| Fig. 4.14. Wind direction at different heights: (a) 2020 0219 am; (b) 2020 1021 am; (c) 2020 1021 pm; (d) 2020 1020 pm; (e) 2019 0416 pm; and (f) 2020 0218 pm | 102 |

| | |
|---|-----|
| Fig. 4.15. Correlation plots and coefficients between variables from field campaigns | 106 |
| Fig. 5.1. Satellite image of the site. A first landfill cell (a) and leachate reservoirs (b) were the methane source of interest. Another landfill cell (c), food waste treatment facility (d), and manure treatment facility (e) were excluded . | 113 |
| Fig. 5.2. Methane flux at downstream measurement plane at (a) 2019 0416 pm; (b) 2019 0830 am; (c) 2020 0218 pm; (d) 2020 0220 pm; (e) 2020 0512 am; (f) 2020 1020 pm; (g) 2020 1021 am; and (f) 2020 1021 pm | 117 |
| Fig. 5.3. Methane flux from preliminary flights where a single plume appeared at both the upstream (a) and downstream (b) measurement planes..... | 119 |
| Fig. 5.4. Flight trajectory (yellow lines), wind direction (cyan broken lines), and integrated methane flux on the downstream measurement plane at (a) 2019 0416 pm; (b) 2019 0830 am; (c) 2020 0218 pm; (d) 2020 0220 pm; (e) 2020 0512 am; (f) 2020 0512 pm; (g) 2020 1020 pm; (h) 2020 1021 am; and (i) 2020 1021 pm..... | 120 |
| Fig. 5.5. Maximum CH ₄ concentrations at downstream measurement planes: measured at site and simulated by the Gaussian dispersion model | 127 |
| Fig. 5.6. Methane concentrations at steady state simulated by advection-dispersion model with different wind speeds..... | 131 |

LIST OF TABLES

| | |
|--|-----|
| Table 2.1. Pasquill stability categories (Pasquill, 1961) | 11 |
| Table 2.2. Coefficients for use in calculation of dispersion parameters. Equations for σ_y and σ_z are as follows: $\sigma_y = \exp[I_y + J_y \ln x + K_y (\ln x)^2]$; and $\sigma_z = \exp[I_z + J_z \ln x + K_z (\ln x)^2]$ where σ_y , σ_z , and x in m (Seinfeld and Pandis, 2016) | 11 |
| Table 2.3. Comparisons between types of gas analyzers | 35 |
| Table 2.4. Instruments for methane detection in literature | 38 |
| Table 2.5. Specifications of commercial methane analyzers that weigh < 1 kg | 39 |
| Table 3.1. Specification of the UAV and methane detector | 51 |
| Table 3.2. Summary of meteorological data during the field measurement | 54 |
| Table 3.3. Predictive performance of spatial interpolation methods in five times repeated cross-validation (mean \pm standard deviation) | 68 |
| Table 4.1. Average wind determined by different determination methods in near-field experiments | 97 |
| Table 4.2. Typical values of the Hellman exponent depending on the location and air stability (Kaltschmitt et al., 2007) | 101 |
| Table 4.3. Summary of wind estimation from field campaigns | 103 |

| | |
|---|-----|
| Table 5.1. Maximum downwind distance of a measurement plane from the source, which was simulated by the Gaussian dispersion model supposed 3,600 kg/day emission rate and the given measurement unit | 128 |
| Table 5.2. Weather data and estimated methane emissions from successful field campaigns | 133 |

Chapter 1. Introduction

1.1 Background

As it is now told 95 % certain that humans are the major contributor to the climate change (IPCC, 2014), the emission and accumulation of greenhouse gases (GHGs) in the atmosphere is of great concern, and there is increasing needs for monitoring GHG emissions created by a variety of human activities. As an international effort, many countries have been monitoring their GHG emissions and reporting the annual emissions, which was established by the Kyoto Protocol. In 2020, more than 40 countries reported their national GHG inventories to the United Nations Framework Convention on Climate Change (UNFCCC). As a non-Annex I country, Korea has been submitting the national communication and biennial update report to UNFCCC, and also publishing the national inventory every year for domestic report (GIR, 2020). Monitoring emissions also helps improve existing emission estimating models, and encourage mitigation efforts. Current estimation methodologies often do not reflect results from mitigation strategies so that the mitigation efforts cannot get rewards for them.

Methane is a critical GHG that accounts for 16 % of global warming effect (Myhre et al., 2014). Its high global warming potential (28 and 34 without and with including the climate-carbon feedback, respectively) and its short lifetime (12.4 yrs) (Myhre et al., 2014) give methane the priority to be thoroughly managed. As it is a short-lived GHG, it is anticipated that its reduction in emissions will decrease its concentrations in the atmosphere sooner.

An important source of anthropogenic methane is waste landfills. Landfills are the second largest (20%) source in Europe, and the third (20%) in the United States (EEA, 2016; EPA, 2016). GIR (2020) reported that waste landfilling was the largest contributor with 28 % contribution (7.8 million ton-CO₂eq.) to the national emission of anthropogenic methane of Korea in 2018. In landfills, the decomposable organic fraction of disposed waste experience biochemical decomposition for years to centuries, resulting in the generation of methane and carbon dioxide. While gas recovery systems and methane-oxidizing cover materials are applied to prevent the gas release to the atmosphere at some landfill sites, there are still fugitive methane through the surface, wells, vents, cracks, and leaks, which has to be accurately quantified. Whereas methane generation in modern landfills receiving low-organic waste used to be believed negligible, recent studies have reported results that support the probability of significant methane production from low-organic waste disposed at landfills (Duan et al., 2021; Mou et al., 2015).

The main obstacles that challenge the quantification of methane emissions have something to do with the scale and complexity of landfills. Waste landfills are inhomogeneous both spatially and temporally in terms of waste composition, operation, geotechnical properties, etc. Simulation models cannot fully reflect such variability using a finite number of model parameters, and it has been often told that they tend to overestimate emissions (Lee et al., 2020; Raco et al., 2010). From that reason, direct surface measurements like flux chamber can be employed to know more exact emissions. Then, there would be a high possibility of obtaining biased estimation of emissions with a limited number of sample survey (Jeong et al., 2019; Mønster et al., 2019). It is impractical to conduct complete survey because emissions

occur throughout the large area of a whole landfill site. Furthermore, flux chamber is capable of measurements only at flat areas, but not around ditch, uncovered area, and vent, and it is a disturbing method in that coverage by a chamber alters surface conditions that govern gas transport (Oonk, 2010).

A promising alternative for emission quantifications is measuring plumes at downwind of the landfill assisted by mobile platforms, which is a direct measurement method, and quick whole-site survey in contrast to the aforementioned methods. Among mobile platforms, rotary wing unmanned aerial vehicles (UAVs) are an appropriate option for the application for landfills considering the emitter height and the scale of target area. However, trials of methane emission measurement in landfills employing rotary wing UAVs have been scarce. Shah et al. (2019) showed the applicability of rotary UAV-based platform conveying air samples to a gas analyzer on the ground through a long tubing. In spite of the restriction in spatial coverage, this method was adopted because the gas analyzer with satisfying performance was too heavy for rotary UAVs. Very recently, Shah et al. (2020) could assess a lightweight prototype analyzer carried by a rotary UAV in exterior experiments with controlled methane emissions.

In this work, a UAV-based procedure combining plume measurement and mass balance was proposed for quantifying fugitive methane from landfills. The procedure to propose in this study employed following options: (1) Mass balance approach is an option of plume measurement methods, which can take full advantages of aerial measurements, and still needs research and field trials for the establishment. (2) A rotary UAV is a type of UAV appropriate for landfill applications in that it is capable of planned flights and dense sampling. Variables to collect at site in this procedure

include methane concentrations and wind data. (3) An onboard methane sensor allows of collecting methane concentrations at a number of points without adding restrictions to flight. (4) As another input variable for the emission calculation, the average wind direction and vertical wind speed gradient are estimated using the GPS and IMU data of UAV flight logs, so that the accuracy in wind data can increase without additional instrument.

To promote this relatively new method, there is a need for in-depth research addressing all potential error-inducing factors. The proposed procedure can be delved into by dividing into four elements: methane profile acquisition, wind estimation, measurement practice, and emission calculation. First, it is imperative to tackle questions involved in methane profile acquisition. For instance, the reluctance to adopt gas sensors onboard rotary UAVs are attributed to artefacts that may result from propeller downwash, but related research is limited to aerodynamics around the hovering fuselage (Guo et al., 2020). A new option for meteorological data needs to be introduced and tested in the setup around landfills. Although it was pointed out by several research teams that the accuracy of meteorological observation is a critical contributor to uncertainties of plume measurements (Mønster et al., 2019; Nathan et al., 2015), there have been scarce efforts to increase the accuracy of meteorological data. Last but not least, field applications would enable to evaluate the competence of the entire procedure, taking into account the actual practices and the uncertainty propagation in the emission calculation process, as well as delivering successful showcases.

1.2 Objectives

This study aimed to establish a rotary UAV-assisted procedure as an efficient and reliable method for quantifying methane emission from waste landfills. The specific objectives to achieve the goal were as follows:

- 1) To evaluate the reliability of rotary UAV-based measurement system in obtaining airborne methane profile;
- 2) To examine the performance of rotary UAV-based wind estimator to measure wind changes with time and height;
- 3) To assess the entire method for quantifying methane emission in terms of practicality and uncertainty.

1.3 Dissertation structure

This dissertation consists of six chapters (Fig. 1.1). Chapter 1 describes the background and the outline of the proposed methodology. Chapter 2 reviews the previous studies related to this work. Chapters 3 and 4 present and evaluate methods for methane profile acquisition and wind vector estimation, respectively. Chapter 5 reports methane emissions and uncertainties derived from multiple field applications. Chapter 7 provides the summary and conclusions of the entire study.

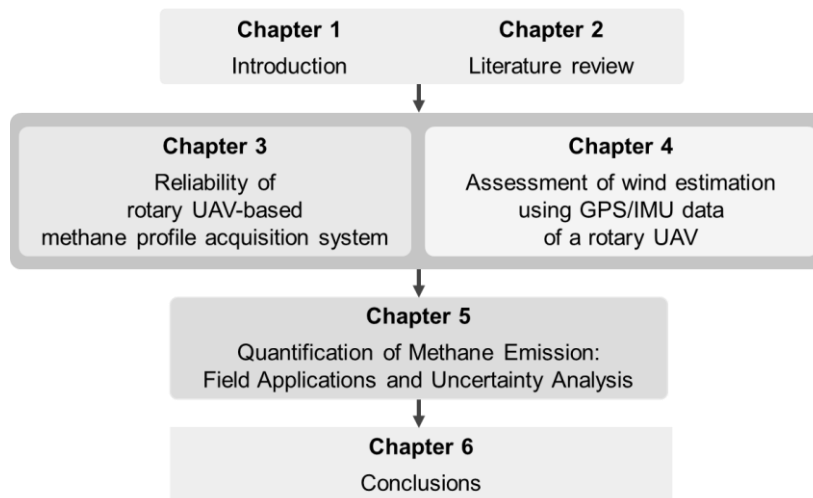


Fig. 1.1. Dissertation structure.

References

- Duan, Z., Kjeldsen, P., Scheutz, C., 2021. Trace gas composition in landfill gas at Danish landfills receiving low-organic waste. *Waste Management* 122, 113-123.
- EEA, 2016. Annual european community greenhouse gas inventory 1990-2014 and inventory report 2016. Submission to the UNFCCC secretariat. EEA Technical report 15.
- EPA, U., 2016. Inventory of U.S. greenhouse gas emissions and sinks: 1990-2014.
- GIR, 2020. 2020 National greenhouse gas inventory report of Korea.
- Guo, Q., Zhu, Y., Tang, Y., Hou, C., He, Y., Zhuang, J., Zheng, Y., Luo, S., 2020. CFD simulation and experimental verification of the spatial and temporal distributions of the downwash airflow of a quad-rotor agricultural UAV in hover. *Comput. Electron. Agric.* 172, 105343.
- IPCC, 2014. Climate change 2014: Synthesis report. Contribution of Working Groups I, II, and III to the fifth assessment report of the Intergovernmental Panel on Climate Change. IPCC, Geneva, Switzerland.
- Jeong, S., Park, J., Kim, Y.M., Park, M.H., Kim, J.Y., 2019. Innovation of flux chamber network design for surface methane emission from landfills using spatial interpolation models. *Sci. Total Environ.* 688, 18-25.
- Lee, K., Jeon, E., Lee, Y., Park, J., 2020. Suggestions for the Estimation of the Methane Emission from a Landfill Site. *Journal of Urban Science* 9, 69-73.
- Mou, Z., Scheutz, C., Kjeldsen, P., 2015. Evaluating the methane generation rate constant (k value) of low-organic waste at Danish landfills. *Waste Management* 35, 170-176.
- Mønster, J., Kjeldsen, P., Scheutz, C., 2019. Methodologies for measuring fugitive

- methane emissions from landfills—A review. *Waste Management* 87, 835-859.
- Myhre, G., Shindell, D., Bréon, F., Collins, W., Fuglestvedt, J., Huang, J., Koch, D., Lamarque, J., Lee, D., Mendoza, B., 2014. Chapter 8: Anthropogenic and Natural Radiative Forcing. *Climate Change 2013: The Physical Science Basis*.
- Nathan, B.J., Golston, L.M., O'Brien, A.S., Ross, K., Harrison, W.A., Tao, L., Lary, D.J., Johnson, D.R., Covington, A.N., Clark, N.N., Zondlo, M.A., 2015. Near-Field Characterization of Methane Emission Variability from a Compressor Station Using a Model Aircraft. *Environ. Sci. Technol.* 49, 7896-7903.
- Oonk, H., 2010. Literature review: methane from landfills. Final report for Sustainable landfill foundation.
- Raco, B., Battaglini, R., Lelli, M., 2010. Gas emission into the atmosphere from controlled landfills: an example from Legoli landfill (Tuscany, Italy). *Environmental Science and Pollution Research* 17, 1197-1206.
- Shah, A., Allen, G., Pitt, J.R., Ricketts, H., Williams, P.I., Helmore, J., Finlayson, A., Robinson, R., Kabbabe, K., Hollingsworth, P., 2019. A near-field gaussian plume inversion flux quantification method, applied to unmanned aerial vehicle sampling. *Atmosphere* 10, 396.
- Shah, A., Pitt, J.R., Ricketts, H., Leen, J.B., Williams, P.I., Kabbabe, K., Gallagher, M.W., Allen, G., 2020. Testing the near-field Gaussian plume inversion flux quantification technique using unmanned aerial vehicle sampling. *Atmospheric Measurement Techniques* 13.

Chapter 2. Literature review

2.1 Gas transport model

2.1.1 Gaussian dispersion model

Gaussian dispersion model simulates three-dimensional gas concentrations under conditions of continuous emission and steady state. The key assumptions are the mass conservation and gaussian distributions of concentration in every direction. None of the material is removed or lost through reaction, gravitational settling or turbulent impaction. The pollutant dispersed close to the ground surface is again dispersed away, which is called eddy reflection (Turner, 1994). The plume appears as if it originated at an equivalent stack height due to the buoyancy of the hot gases and the vertical momentum of the gases (Wark and Warner, 1981)

The concentration equation for an elevated source with reflection is as follows:

$$C(x, y, z) = \frac{Q}{2 \pi u \sigma_y \sigma_z} \exp\left(-\frac{y^2}{2\sigma_y^2}\right) \left\{ \exp\left[\frac{-(z-H)^2}{2\sigma_z^2}\right] + \exp\left[\frac{-(z+H)^2}{2\sigma_z^2}\right] \right\} \quad (2.1)$$

where C : volume concentration [-] or mass-volume concentration [ML^{-3}], x : downwind distance from the source [L], y : distance from the plume centerline [L], z : height above ground level [L], Q : source emission rate [L^3T^{-1} or MT^{-1}], u : wind velocity [LT^{-1}], σ_y : vertical standard deviation of the emission distribution [L], σ_z : horizontal standard deviation of the emission distribution [L], H : effective source height above ground level [L].

Dispersion parameters (σ_y and σ_z) that appear in Eq. (2.1) are determined as functions of downwind distance and Pasquill stability class (Table 2.1). There are more than a few different methods suggested by researchers so far, one of which is provided in Table 2.2.

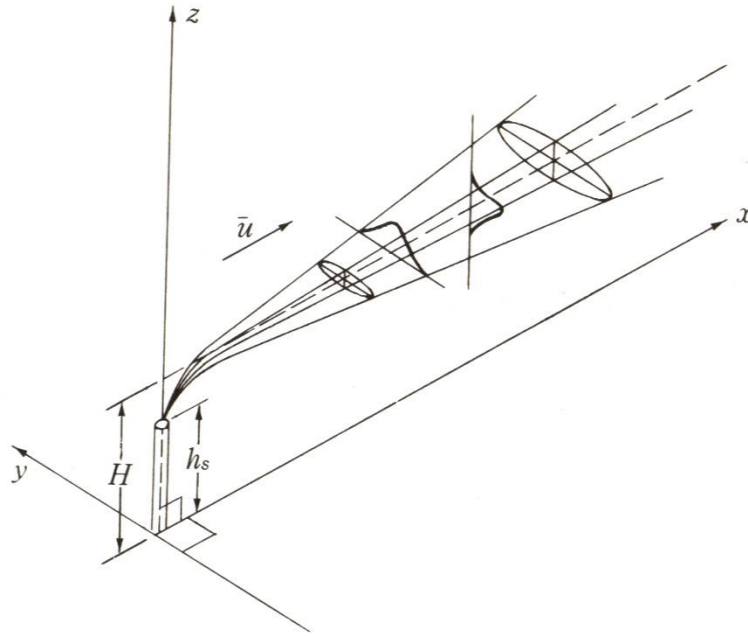


Fig. 2.1. Schematic diagram illustrating the concept of Gaussian plume model (Turner, 1994).

Table 2.1. Pasquill stability categories (Pasquill, 1961).

| Surface wind speed at 10 m, m/s | Insolation | | | Night | |
|---------------------------------------|------------|----------|--------|--------------------------------------|------------|
| | Strong | Moderate | Slight | Thinly overcast or >4/8 low cloud | <3/8 cloud |
| < 2 | A | A – B | B | - | - |
| 2 – 3 | A – B | B | C | E | F |
| 3 – 5 | B | B – C | D | D | E |
| 5 – 6 | C | C – D | D | D | D |
| > 6 | C | D | D | D | D |

Stability classes: strongly unstable, A; moderately unstable, B; slightly unstable, C; neutral, D; slightly stable, E; and moderately stable, F.

Table 2.2. Coefficients for use in calculation of dispersion parameters. Equations for σ_y and σ_z are as follows: $\sigma_y = \exp[I_y + J_y \ln x + K_y (\ln x)^2]$; and $\sigma_z = \exp[I_z + J_z \ln x + K_z (\ln x)^2]$ where σ_y , σ_z , and x in m (Seinfeld and Pandis, 2016).

| | A | B | C | D | E | F |
|-------|---------|---------|---------|---------|---------|---------|
| I_y | -1.104 | -1.634 | -2.054 | -2.555 | -2.754 | -3.143 |
| J_y | 0.9878 | 1.0350 | 1.0231 | 1.0423 | 1.0106 | 1.0148 |
| K_y | -0.0076 | -0.0096 | -0.0076 | -0.0087 | -0.0064 | -0.0070 |
| I_z | 4.679 | -1.999 | -2.341 | -3.186 | -3.783 | -4.490 |
| J_z | -1.7172 | 0.8752 | 0.9477 | 1.1737 | 1.3010 | 1.4024 |
| K_z | 0.2770 | 0.0136 | -0.0020 | -0.0316 | -0.0450 | -0.0540 |

Plume rise occurs due to the momentum and the buoyancy. Among them, the effects of buoyant release are more likely to produce a greater effect, especially if

the exit temperature is about 10 to 15 degrees (K or C) higher than the air temperature (Turner, 1994). The effective height of the plume, H (m) is calculated by adding the physical height of the source, h_s (m) and the plume rise, Δh (m) determined below (Briggs, 1984; Turner, 1994).

$$F_b = g v d^2 \Delta T / (4 T_s) \quad (2.2)$$

Buoyant rise:

$$\Delta h = 21.425 F_b^{3/4} / u \quad (F_b < 55) \quad (2.3)$$

$$\Delta h = 38.71 F_b^{3/5} / u \quad (F_b > 55) \quad (2.4)$$

Momentum rise:

$$\Delta h = 3 d v / u \quad (2.5)$$

where F_b : buoyancy flux (m^4/s^3), g : acceleration of gravity (9.8 m/s^2), v : gas exit velocity (m/s), d : source diameter (m), ΔT : difference between gas temperature and air temperature (K), T_s : gas temperature (K), u : wind velocity (m/s).

2.1.2 Advection-dispersion model

2.1.2.1 Steady state with negligible longitudinal dispersion

Supposed that gas is released at constant rate at $x = 0$, $y = 0$, and $z = 0$, and the gas transport in the x direction is dominated by advective flow with negligible dispersive flow, the governing equation, boundary conditions, and mass conservation at steady state is expressed as follows:

Governing equation:
$$u \frac{\partial C}{\partial x} = D_y \frac{\partial^2 C}{\partial y^2} + D_z \frac{\partial^2 C}{\partial z^2} \quad (2.6)$$

Boundary conditions:
$$C(0, y, z) = 0 \quad (y \neq 0 \text{ or } z \neq 0) \quad (2.7)$$

$$C \rightarrow 0 \quad (y \rightarrow \infty \text{ or } z \rightarrow \infty) \quad (2.8)$$

$$\left. \frac{\partial C}{\partial y} \right|_{y=0} = 0 \quad (2.9)$$

$$\left. \frac{\partial C}{\partial z} \right|_{z=0} = 0 \quad (2.10)$$

Mass conservation:
$$QC_{in} = u \int_{-\infty}^{\infty} \int_{-\infty}^{\infty} C \, dy \, dz \quad (x > 0) \quad (2.11)$$

For the numerical solution, finite elements were defined as every x_n ($n = 0, 1, 2, \dots$), has a matrix with concentrations at y_i ($i = 1, 2, 3, \dots, I$) and z_j ($j = 1, 2, 3, \dots, J$), spatial elements.

| | y_1 | y_2 | y_3 | ... | y_I |
|-------|-------------|-------------|-------------|-----|-------------|
| z_1 | $C_{1,0}^n$ | $C_{2,1}^n$ | $C_{3,1}^n$ | ... | $C_{I,1}^n$ |
| z_2 | $C_{1,1}^n$ | $C_{2,2}^n$ | | ... | |
| z_3 | $C_{1,3}^n$ | | | ... | |
| . | . | . | . | . | . |
| . | . | . | . | . | . |
| . | . | . | . | . | . |
| z_J | $C_{1,J}^n$ | | | ... | $C_{I,J}^n$ |

Fig. 2.2. Finite elements defined for deriving the numerical solution of advection-dispersion model.

Under forward scheme for x , and central scheme for y and z , the model approximates to the following expressions in finite difference method:

$$\text{Governing equation: } u \frac{C_{i,j}^{n+1} - C_{i,j}^n}{\Delta x} = D_y \frac{C_{i+1,j}^n - 2C_{i,j}^n + C_{i-1,j}^n}{(\Delta y)^2} + D_z \frac{C_{i,j+1}^n - 2C_{i,j}^n + C_{i,j-1}^n}{(\Delta z)^2} \quad (2.12)$$

$$\text{Boundary conditions: } C_{i,j}^0 = 0 \quad (i \neq 1 \text{ or } j \neq 1) \quad (2.13)$$

$$C_{1,j}^n = C_{2,j}^n \quad (2.14)$$

$$C_{i,1}^n = C_{i,2}^n \quad (2.15)$$

$$\text{Mass conservation: } C_{1,1}^n = \frac{QC_{in}}{4u \Delta y \Delta z} \quad (2.16)$$

2.1.2.2 Non-steady state with longitudinal dispersion

Supposed that gas is released at constant rate at $x = 0$, $y = 0$, and $z = 0$, and the governing equation, boundary conditions, and mass conservation at non-steady state is expressed as follows:

$$\text{Governing equation: } \frac{\partial C}{\partial t} = D_T \left(\frac{\partial^2 C}{\partial r^2} + \frac{1}{r} \frac{\partial C}{\partial r} \right) + D_L \frac{\partial^2 C}{\partial x^2} - u \frac{\partial C}{\partial x} \quad (2.17)$$

$$\text{Initial condition: } C(0, x, r) = 0 \quad (x \neq 0 \text{ or } r \neq 0) \quad (2.18)$$

$$\text{Boundary conditions: } C \rightarrow 0 \quad (x \rightarrow \pm \infty \text{ or } r \rightarrow \infty) \quad (2.19)$$

$$\left. \frac{\partial C}{\partial r} \right|_{r=0} = 0 \quad (2.20)$$

$$\text{Mass conservation: } QC_{in} = 2\pi \int_{-\infty}^{\infty} \int_0^{\infty} r \frac{\partial C}{\partial t} dr dx \quad (2.21)$$

For the numerical solution, finite elements were defined as every t_n ($n = 0, 1, 2, \dots$), has a matrix with concentrations at x_i ($i = 1, 2, 3, \dots, 2I$) and r_j ($j = 1, 2, 3, \dots, J$), spatial elements.

Under forward scheme for t , backward scheme for first-order derivative of x and r , and central scheme for second-order derivative of x and r , the model approximates to the following expressions in finite difference method:

Governing equation:
$$\frac{C_{i,j}^{n+1} - C_{i,j}^n}{\Delta t} = D_T \left(\frac{C_{i,j+1}^n - 2C_{i,j}^n + C_{i,j-1}^n}{(\Delta r)^2} + \frac{1}{j} \frac{C_{i,j}^n - C_{i,j-1}^n}{\Delta r} \right) + D_L \frac{C_{i+1,j}^n - 2C_{i,j}^n + C_{i-1,j}^n}{(\Delta x)^2} - u \frac{C_{i,j}^n - C_{i-1,j}^n}{\Delta x} \quad (2.22)$$

Initial condition:
$$C_{i,j}^0 = 0 \quad (i \neq I \text{ or } j \neq 1) \quad (2.23)$$

Boundary conditions:
$$C_{1,j}^n = C_{2,j}^n \quad (2.24)$$

$$C_{2I-1,j}^n = C_{2I,j}^n \quad (2.25)$$

$$C_{i,1}^n = C_{i,2}^n \quad (2.26)$$

$$C_{i,j-1}^n = C_{i,j}^n \quad (2.27)$$

Mass conservation:
$$C_{I,1}^n = \frac{Q C_{in}}{4\pi u \Delta r^2} \quad (2.28)$$

As equation 2.17 has not been analytically solved, to the author's knowledge, it was impossible to verify the presented numerical solution through comparing it to the corresponding analytical solution. Instead, supposed steady state, the numerical solution can produce a concentration profile comparable to the Gaussian dispersion model, as shown in [Fig. 2.3](#). The model parameters used for this comparison follow:

$QC_{in} = 3600 \text{ kg/d}$; $u = 2 \text{ m/s}$; $D_T = 4 \text{ m}^2/\text{s}$; $D_L = 2 \text{ m}^2/\text{s}$; $\Delta t = 0.01 \text{ s}$; $\Delta x = 5 \text{ m}$; and $\Delta r = 2 \text{ m}$. The scales of time and space elements were carefully chosen to avoid an oscillation problem.

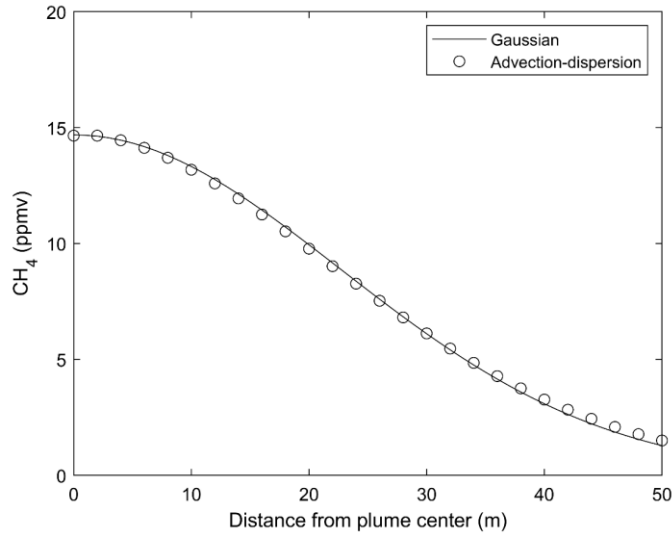


Fig. 2.3. Concentration profile at 200 m downwind from the source predicted by the Gaussian dispersion model and a numerical solution of the advection-dispersion model.

2.2 Variability in fugitive emission from waste landfills

Fugitive methane emission through landfill surface is a complicated issue that involves multiple intertwined processes. Even within a single landfill cell, the inhomogeneous composition of waste and gas inside the cell results in the different rate and composition of landfill gas generation. A greater extent of diversification

often comes during penetration of the gas via cover materials. The flow rate and composition of landfill gas at discharge come to variate from those under cover again, after undergoing a complex combination of multiple processes. The divergency in texture and thickness of cover, gas and liquid permeability, availability of moist, oxygen, and nutrients, abundance of surface vegetation, etc., and consequently heterogeneous gas flow rate and methane oxidation rate lead to temporal and spatial variability in surface methane emission rates (Spokas et al., 2015).

The variability has been reported in lots of literature (Fjelsted et al., 2019; Gonzalez-Valencia et al., 2021; Jeong et al., 2019; Rachor et al., 2013; Raco et al., 2010). There is complete agreement about spatial inequality. A majority of surface emissions are released from just a small portion of surface area, so-called “hot spots,” which is supported by the observations that 20 % of the areas were responsible for 67.7-99.8 % of total surface emissions of the ten landfills tested in Jeong et al. (2019), and only 3 % of the areas were for 80 % of emissions of the landfill investigated in Gonzalez-Valencia et al. (2021). Temporal variation in total methane emissions is considered large for many occasions, ranging from negative—possible with strong gas extraction or oxidation of atmospheric methane—to massive positive flux, even though there are some cases where emissions observed over a time interval fall in the same order of magnitude (Czepiel et al., 2003; Jeong et al., 2019). As for the cases where emissions always exceeded the detection limit, the difference in emissions between measurement times was by up to two orders of magnitude within a few days (Gonzalez-Valencia et al., 2021; Zhang et al., 2013). Moreover, Rachor et al. (2013) presented that the seasonal variability in emissions was greater than daily or diurnal one.

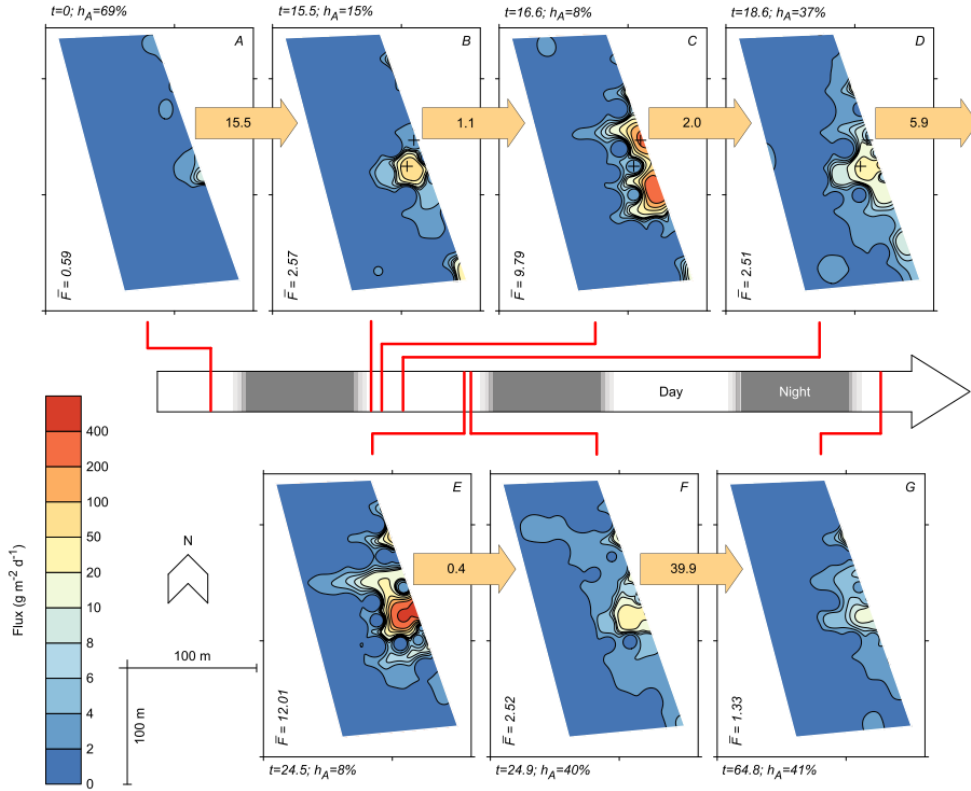


Fig. 2.4. Methane flux maps and mean flux observed over three days, which show both temporal and spatial variations in surface methane emissions of landfills (Gonzalez-Valencia et al., 2021).

Due to the fugitive emissions fluctuating with time and location, sampling in terms of time or location may not provide adequate representativeness. More frequent and denser sampling is a solution for temporal and spatial representativeness, respectively, which usually adds labors and costs. Therefore, time- and cost-efficient methods need to be introduced for measuring the emission from a whole landfill.

2.3 Estimation methods for fugitive gas emission

2.3.1 Simulation models for waste landfills

As it is hard to quantify fugitive greenhouse gas emissions from waste landfills via direct measurements, reporting inventories about landfills has been depending on modeling with conservative parameterization. As a representative model, the current IPCC guidelines present the first order decay model to simulate biochemical decomposition of organic compounds and resulting methane emissions in waste landfills. The most recent refinement allows the model to simulate reactions in landfills in which aerobic decomposition dominates, using a specific correction factor (IPCC, 2006, 2019).

The methane emissions can be estimated by excluding recovered and surface oxidized amounts from total generations.

$$CH_4 \text{ Emissions} = [\sum_x CH_4 \text{ generated}_{x,T} - R_T] \cdot (1 - OX_T) \quad (2.29)$$

where $CH_4 \text{ Emissions}$: methane emitted in year T (Gg); T : inventory year; x : waste category or type/material; R_T : recovered methane in year T (Gg); and OX_T : oxidation factor in year T (fraction). In IPCC (2000), methane generation is determined considering the decomposable portion of disposed waste, landfill condition, and the first order decay.

$$DDOC_m = W \cdot DOC \cdot DOC_f \cdot MCF \quad (2.30)$$

$$L_0 = DDOC_m \cdot F \cdot 16/12 \quad (2.31)$$

where $DDOC_m$: mass of decomposable DOC deposited (Gg); L_0 : methane generation potential (Gg CH_4); W : mass of waste deposited (Gg); DOC : degradable organic carbon (fraction, Gg C/Gg waste); DOC_f : fraction of DOC that can decompose (fraction); MCF : methane correction factor for aerobic decomposition (fraction); F : fraction of methane in generated landfill gas (volume fraction); 16/12: molecular weight ratio of methane to carbon (ratio).

$$CH_4 generated_T = \sum_t A \cdot k \cdot L_{0,t} \cdot e^{-k(T-t)} \quad (2.32)$$

where t : years for which input data should be added, A : normalization factor correcting the summation ($= (1-e^{-k})/k$); k : methane generation rate constant (yr^{-1}). Equation (2.19) was written adjusted in this work so that it is compatible with other equations from the recent refinements.

The refined IPCC guidelines recommend to substitute Equation (2.19), but the basic concept of first order decay model is consistent. While the former version requires the whole history of a site, the new version simplifies it to use the decomposable newly disposed in the year, and remained till the previous year (IPCC, 2006, 2019).

$$DDOCm decomp_T = \{DDOCmd_{T-1} + (DDOCma_{T-2} \cdot e^{-k})\} \cdot (1 - e^{-k}) \quad (2.33)$$

$$CH_4 generated_T = DDOCm decomp_T \cdot F \cdot 16/12 \quad (2.34)$$

where $DDOCma_{T-2}$: $DDOCm$ accumulated at the end of year $T-2$ (Gg); $DDOCmd_{T-1}$: $DDOCm$ deposited in year $T-1$ (Gg); $DDOCm decomp_T$: $DDOCm$ decomposed in

year T (Gg); $k = \ln 2/t_{1/2}$; and $t_{1/2}$: half-life time (yr).

GIR (2020) reported the greenhouse gas emissions from landfills in Korea using the above model of IPCC (2000). The IPCC default values were mostly used as model parameters (MCF 1.0; DOC 0.09; DOC_f 0.5; and OX 0.1), except for two country-specific parameters (k 0.05; and F 0.5629).

Phenomena are extremely difficult to predict when they involve biological reactions, and waste landfills are inherently inhomogeneous in terms of waste composition, operation, geotechnical properties, etc. Therefore, it is questionable if a combination of model parameters picked from the given sets of values would sufficiently explain the variety of conditions. The Sudokwon Landfill, the largest well-managed landfill in Korea, has consistently maintained that modeling based on the IPCC guidelines overestimated its methane emissions compared to the results of extensive monitoring for years (Lee et al., 2020). They suggested that the reason would be the effects of constituents other than organic carbon in the waste, and high oxidation factor that are not found in the IPCC guidelines. The difference was more evident in cases of closed landfills with complete final cover, which means that various efforts for reducing emissions cannot be acknowledged using the IPCC model. Raco et al. (2010) provided another explicit evidence of the weak point of simulation models. They showed that a significant reduction in actual emissions followed remedial works on covers and gas recovery system in comparison with still increasing emissions estimated using several simulation models.

2.3.2 Surface measurements of fugitive gas

Flux chamber is the most common method to directly measure surface emissions.

With a chamber sealed on a surface, the surface emission can be estimated using changes in gas composition inside the chamber. Although it is the most verified method for direct measurement, it contains several disadvantages. Flux chamber is likely to underestimate emissions from waste landfills, because a limited number of point measurements cannot include all hotspots that dominate emission routes, and chambering is disable to measure emissions through wells and vents (Mønster et al., 2019). According to the equation proposed by Jeong et al. (2019), a chambering for every 40 m² is required to ensure < 20% error, which will be extremely labor-intensive due to considerable time required for a single measurement—a few tens of minutes at least. Furthermore, flux chamber is surprisingly a disturbing method in that coverage by a chamber alters surface conditions, e.g. pressure, air flow, and concentration gradient, that govern gas transport (Oonk, 2010).

Utilizing relationships between surface flux and easily detectable variables is an alternative that would be rapid and less disturbing. Park et al. (2016) and Gonzalez-Valencia et al. (2021) tried to correlate surface methane concentration and flux. Their results showed good linear relationships within a few days, but the relations were not universal over months or years even in the same landfill cell (Fig. 2.5). Another type of trials involved surface temperature, which could be convincing in consideration that landfill gas usually has higher temperature than surroundings. Field studies testing the applicability showed weak or no relationships between surface temperature and methane flux (Fjelsted et al., 2019; Ishigaki et al., 2005). Those methods seem insufficient to be used for the estimation of methane emission, but can be useful as a complementary tool to the flux chamber.

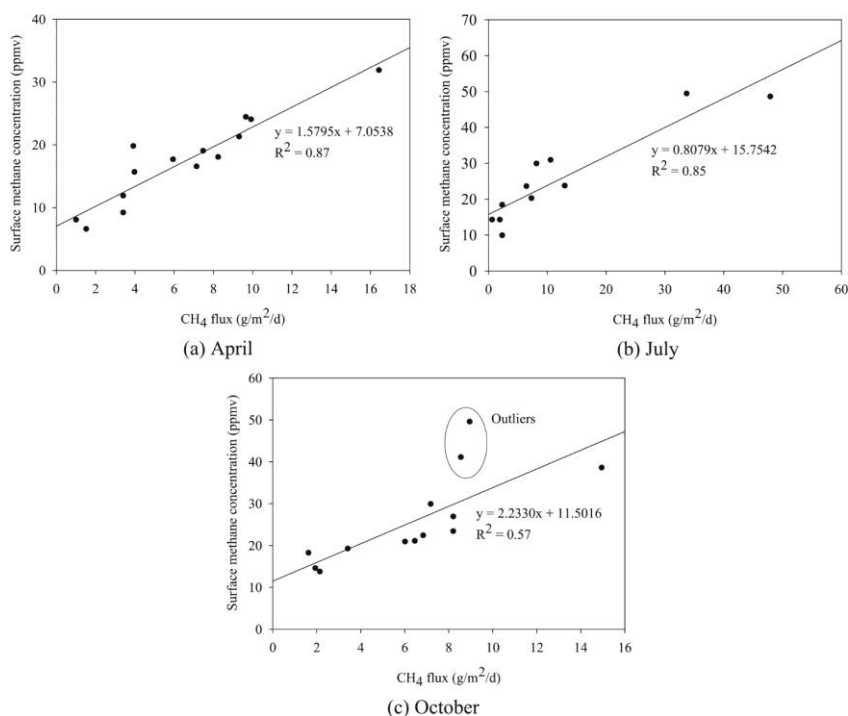


Fig. 2.5. Correlation between surface methane flux and concentration (Park et al., 2016).

2.3.3 Plume measurements from fugitive sources

Fugitive gas can be measured at the downstream of the sources. With a clear advantage that it can offer an integrated emission from the whole site, this strategy has been vigorously studied for the application for natural gas region and processing facilities, and waste landfills. Gas concentrations measured at the downstream are used to compute the gas release rates based on mass balance, inverse modeling, or tracer dispersion. Sharing the strong point of plume measurement method, the three approaches involve different challenges.

Mass balance method considers integrated gas flux through downwind plane as the emission from a source, and subtracting gas flux through upwind plane would

add the estimation accuracy when available (Allen et al., 2016; Lavoie et al., 2015; Nathan et al., 2015). The largest challenge for applying the mass balance method is that the whole plume should be covered, which is achievable not by ground-based measurements, but only by aerial measurements. Gas flux estimated by mass balance is highly sensitive to wind data, therefore, the method requires the good measurements of wind as well as gas of interest.

Inverse modeling of concentrations at downwind plane also allows of computing the emission rates. Gaussian model (Shah et al., 2020; Yacovitch et al., 2015), Lagrangian model (Zhu et al., 2013), and EPA AERMOD (Lan et al., 2015) were used in inverse modeling in literature. Extensive data works are required during modeling with multiple unknown parameters. This method also requires accurate wind data, like mass balance method.

In tracer dispersion method, tracer gas, e.g. C_2H_2 , N_2O , SF_6 , is released at a known flow rate near an emission source, and the target gas and the tracer gas are measured at downwind. The emission rate of the target gas is then estimated using the reduction rate of tracer gas (Mitchell et al., 2015; Mønster et al., 2015). The last methodology is well proven among three kinds of plume measurement methods, but its shortcomings include a challenge in proper tracer placement and the requirement of potent greenhouse gas release.

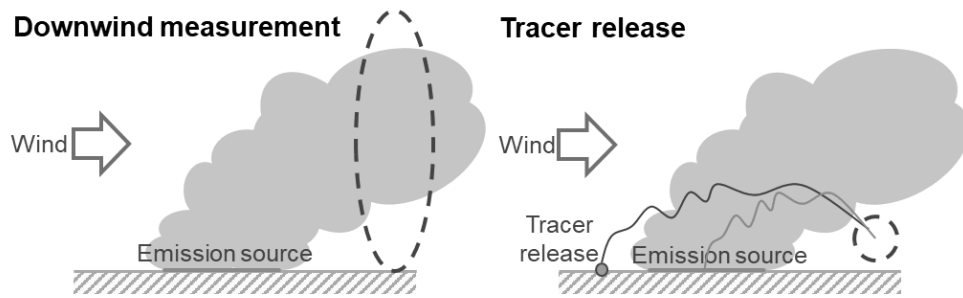


Fig. 2.6. Concept of plume measurements and tracer dispersion method.

Linear (or, open-path) gas analyzers and point gas analyzers are option to use to measure gas concentrations at downwind. Linear analyzers are widely used to achieve rapid, accurate gas detection on ground. Depending on occasions, point analyzers can be preferred for higher dimensional information. Employment of mobile platforms is required to operate point analyzers throughout downwind measurement planes. Currently available mobile platforms include vehicle (Mitchell et al., 2015; Mønster et al., 2015), manned aircraft (Lavoie et al., 2015; Mays et al., 2009), and UAV (Allen et al., 2016; Nathan et al., 2015; Shah et al., 2020), which should be selected depending on the emitter type, flight speed, practical restrictions, and cost (Shah et al., 2019).

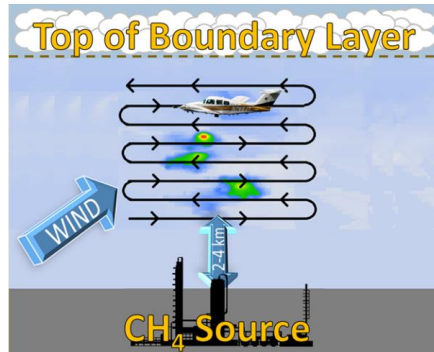


Fig. 2.7. Plume measurement by manned aircraft in shale region (Lavoie et al., 2015).

2.4 Gas analyzer

2.4.1 Principles of gas analyzers

Gas detectors can be classified according to the operation principles, e.g., electrochemical, catalytic combustible, solid-state (semiconductor), infrared, photoionization, etc.

A. Electrochemical sensors

Gas first passes through a small capillary-type opening and then diffuses through a hydrophobic barrier (membrane), and eventually reaches the electrode surface. The barrier allows the proper amount of gas to react at the electrode, and sometimes filters out unwanted gases, while preventing the electrolyte from leaking out of the sensor. Then, the gas either oxidizes or reduces at the surface of the sensing electrode with specific catalysis by the electrode materials. The current generated in the process is measured to determine the gas concentration, which is proportional to the

gas concentration.

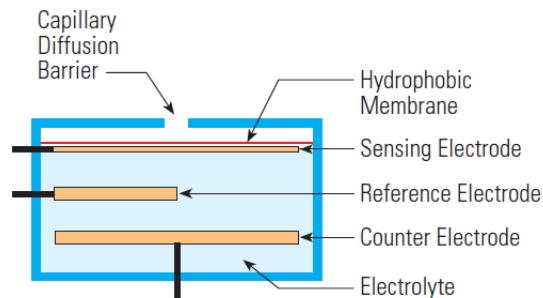


Fig. 2.8. Typical electrochemical sensor setup (Chou, 2000).

The characteristics of electrochemical sensors are as follows:

- 1) Typical detectable gases: NH_3 , CO , H_2 , H_2S , NO , NO_2 , O_2 , SO_2 (from ppm levels up to 2-10 times permissible exposure limit).
- 2) Some sensors that require an external voltage cannot be removed from power for an appreciable time.
- 3) Most of the toxic gas sensors require oxygen.
- 4) Humidity: For the sensors with high sensitivity, high humidity can cause the electrolyte to leak out and low humidity can dry it out. Relatively stable operation is possible at relative humidity 15-95 %.
- 5) Pressure: Electrochemical sensors are minimally affected by pressure.
- 6) Temperature: Electrochemical sensors quite sensitive to temperature and therefore are typically internally temperature-compensated, resulting in the

operation temperature from -40 to $+45$ ° C. In general, when the temperature is above 25 ° C, the sensor will read higher; when it is below 25 ° C, it will read lower.

- 7) Selectivity: Electrochemical sensors are generally fairly selective to the target gas because they are specifically designed by selecting the membranes and the sensing electrode materials. But the sensors other than O₂ sensor are subject to interference from other gases.
- 8) Life expectancy: Generally, the sensors have a one- to three-year life expectancy with susceptibility for corrosive elements and contamination.
- 9) Power consumption: The power consumption is the lowest among all gas sensors available.
- 10) Response time: $T_{80} < 50$ s.

B. Catalytic combustible (catalytic beads) sensors

When gas oxidizes at a much lower temperature than its normal ignition temperature on the active sensor surface that consists of catalysts (e.g., platinum), the heat of combustion causes the temperature to rise, which in turn changes the resistance of the sensor. As the reference (passive) bead maintains a constant resistance, the offset voltage is measured as the signal. The sensor's output is directly in proportion to the rate of oxidation.

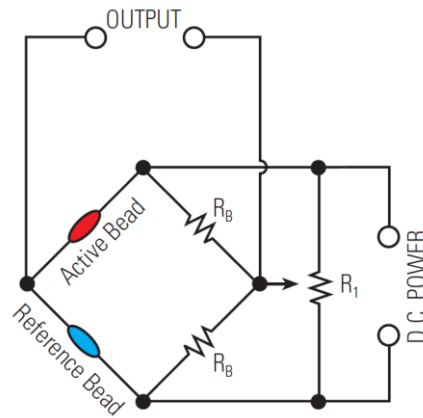


Fig. 2.9. A typical circuit of a catalytic beads sensor (Chou, 2000).

The characteristics of catalytic beads sensors are as follows:

- 1) Detectable gases: combustible gases (from a few hundred ppm to a few volume percent).
- 2) The sensors require oxygen for combustion.
- 3) There are chemicals that will poison the catalyst (e.g., silicon compounds, sulfur compounds, chlorine, heavy metals, etc.) or temporarily inhibit the sensor (e.g., halogen compounds, Freon).
- 4) Selectivity: Catalytic combustible sensors cannot provide selective detection among combustible gases. The users can measure different hydrocarbons by using correction factors that the manufacturers provide or by directly calibrating the sensor to the gas of interest.
- 5) Operation temperature: -40 to $+60$ ° C.
- 6) Response time: T_{90} 10–15 s.

7) Life expectancy: < 3 years.

C. Solid-state (semiconductor) sensors

The absorption or desorption of gas on a metal oxide surface alters the free electron density of the surface of metal oxides and results in the conductivity change. A pair of biased electrodes are imbedded into the metal oxide to measure this change, which is a linear relationship with the gas concentration. In addition, a heating element is used to heat the sensor to an optimal temperature so that the chemical processes are selectively hastened and the effects of fluctuating external temperatures is minimized.

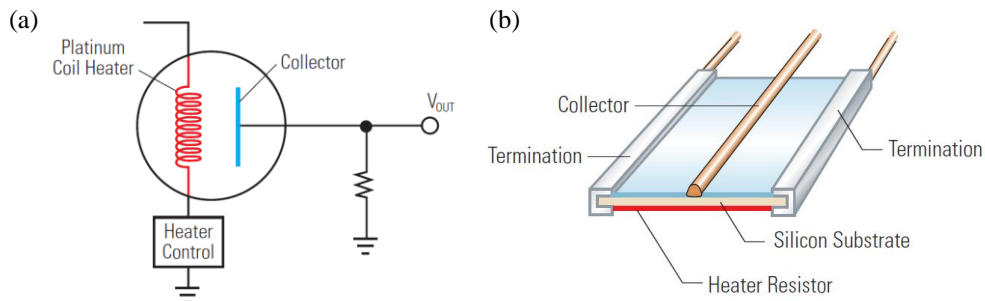


Fig. 2.10. Typical solid-state gas sensors: (a) bead-type; and (b) chip-type (Chou, 2000).

The characteristics of solid-state gas sensors are as follows:

- 1) Solid-state sensors are the most versatile among gas sensors in terms of detectable gas types and ranges (from low ppm levels to high combustible levels).

- 2) Life span: The main strength of the solid-state sensor is its long life expectancy, as the sensor typically lasts 10 years or more in clean applications.
- 3) Drift: One of the important drawbacks of semiconductor sensors is a baseline drift caused by the alteration of the microstructure and by irreversibly adsorbed gases.
- 4) Interference: The sensors are more susceptible to interference gases than the other types of sensors. In certain instances, the interferences are minimized by using appropriate filtering materials.
- 5) Response time: T_{80} 20–90 s.

D. Infrared sensors

Among electromagnetic waves from gamma rays to radio waves, the infrared (IR) region that has wavelength in microns is most useful for gas analysis because absorption by gas molecules is unique and selective in this region. Gas molecules are made up of a number of atoms bonded to one another and the bonding vibrates with a fixed frequency called the natural frequency. When infrared radiation interacts with gas molecules, part of the energy that has the same frequency as the molecule's natural frequency is absorbed while the rest of the radiation is transmitted. Then, the temperature rise resulted from increased vibration of the molecule or the radiation decrease from the light absorption is detected as a signal.

There are two types of IR gas analyzers, namely dispersive and nondispersive, depending on the way in which the specific wavelength of interest is extracted from the infrared source. Dispersive types utilized grating or prism to spread the light spectrum and nondispersive types (nondispersive infrared, NDIR) use discrete

optical bandpass filters. Almost all commercial IR instruments are of the nondispersive type.

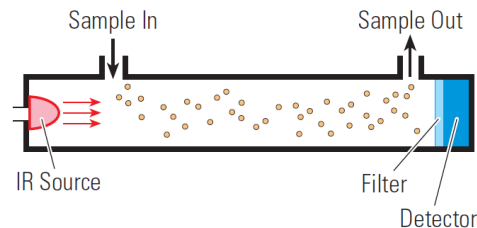


Fig. 2.11. A basic infrared gas detector layout (Chou, 2000).

The characteristics of infrared gas sensors are as follows:

- 1) Detectable gases include hydrocarbons, water vapor, CO₂, etc. (ppm levels to 100 %)
- 2) Selectivity: IR sensors are highly selective. Optical filters determine the selectivity of the instruments.
- 3) Temperature: An IR detector is essentially a temperature sensor and is, therefore, potentially very sensitive to changes in the ambient temperature. However, a properly designed detector can be operated between -40 and 60 ° C.
- 4) Humidity: Normal environmental humidity has very little effect. However, high humidity could promote corrosion and contamination.
- 5) Life span: It has a long life expectancy mainly because it does not directly interact with the gas to be detected. The IR light source typically has a life expectancy on the order of 3 to 5 years.

- 6) Additional advantages over the other sensor types: a) Poisoning by some compounds and burn out by high gas concentrations are the main problems with catalytic sensors, from which IR detectors do not suffer. b) IR units are assured a good response and accuracy as long as the zero is maintained. c) IR instruments can be used to monitor a gas stream continuously over a long period of time whereas constant exposure to gas will shorten life spans of catalytic and solid-state sensors.

E. Photoionization sensors

Excited molecules of inert gas, such as argon, krypton and xenon, in a lamp emit ultraviolet (UV) light, returning to the ground state. A pair of electrode plates are placed in close proximity to the lamp window where the light comes out. As gas molecules of interest move into the radiated field, they are ionized and the free electrons are collected at the electrodes resulting in a current flow whose magnitude is directly proportional to the gas concentration.

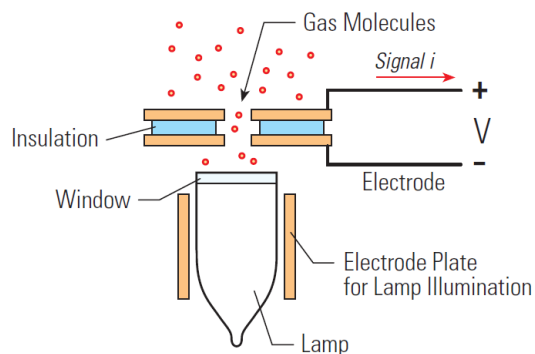


Fig. 2.12. A typical photoionization detector configuration (Chou, 2000).

Photoionization detectors have the following characteristics:

- 1) Detectable gases: aromatic hydrocarbons, alkyl iodides, sulfur compounds, amines, etc. (a few ppb to a few thousand ppm)
- 2) Response time: T_{90} 3 s.
- 3) Selectivity: Photoionization detectors (PIDs) respond to all gases that have ionization potentials equal to or less than the eV output of their lamps. They are typically calibrated with isobutylene and readings for other gases are obtained by multiplying the reading by a correction factor.
- 4) Humidity: High humidity decreases the response by up to 30% compared to dry air.
- 5) Quenching effect: Some gases that are ionizable but not ionized can scatter and absorb the UV rays, resulting in a lower output reading. Such quenching gases are water vapor, carbon dioxide, methane, carbon monoxide, etc.
- 6) Response characteristics: The output of the PID sensor is relatively linear below 200 ppm and the output becomes saturated above 2,000 ppm.
- 7) Maintenance: The major shortcoming of the instruments is that the PID lamp requires frequent cleaning. Because the lamp window is directly exposed to the sample stream and a dirty window will produce much different results than a clean window.
- 8) Life span: Due to periodic cleaning required, PID sensors have limited life expectancies and therefore they are not practical choices for use in stationary monitors.
- 9) Sensitivity: 0.1 ppm isobutylene.

10) Temperature: -20 to +50 ° C.

11) Humidity: 0-95% relative humidity.

Table 2.3. Comparisons between types of gas analyzers.

| Sensor type | Electrochemical | Catalytic combustible | Solid-state | Infrared | Photoionization |
|-------------------|--|--|----------------------------------|------------------------------------|--|
| Detectable gases | NH ₃ , CO, H ₂ , NO, O ₂ , etc. | Combustible gases | A wide variety of gases | HCs, water, CO ₂ , etc. | VOCs, etc. |
| Detectable ranges | ppm to 2-10 times PEL | Hundreds of ppm to a few % | ppm to combustible level | ppm to 100% | ppb to thousands of ppm |
| Selectivity | Fair Interference | Poor | Poor Susceptible to interference | High | Poor |
| Response time | T ₈₀ 50 s | T ₉₀ 10-15 s | T ₉₀ 20-90 s | Slow response | T ₉₀ 3 s |
| Humidity | 15-95% Caution needed for high sensitivity sensor | | | | 0-95% High humidity decreases output |
| Temperature | -40 to +45°C Higher reading at higher T | -40 to +60°C | Minimal effect | -40 to +60°C | -20 to +50°C |
| Pressure | Minimal effect | | | Minimal effect | |
| Longevity | 1-3 yrs | 3 yrs | 10 yrs | 3-5 yrs | |
| Notes | Oxygen required for toxic gas detection Susceptible to corrosive elements and contamination | Oxygen required Poisoning and inhibition problems | | | Quenching effect Nonlinear response curves Frequent lamp cleaning required |

F. Sensor selectivity improvement by filters (Ryzhikov et al., 2009)

The selectivity of gas sensors can be enhanced by several different approaches. In sensing with semiconductor detectors, a choice of optimal detection temperature, the doping of the sensing material with catalytic and electroactive admixtures and the use of multiple sensors having different responses to each gas allow significant improvements of the sensor selectivity. The placement of gas filters before the sensing material is another manner that can be used not only in semiconductor sensors but also with other types of gas sensor.

There are two main types of filters: passive (physical) and active (chemical) filters. Passive filters can separate the gases by the different adsorption affinity of the gas molecules on the sieve material or by the size fractionation using the size of the gas molecules and the diameter of the filter pores. The working principle of active filters is based on selective chemical interactions of the gas molecules with the filter material or on catalytic decomposition of the interfering gases on the filter surface with formation of low active products.

One example of selectivity improvement by using filters is the use of a platinum filter for methane detection by semiconductor gas sensor that was proposed by Logothetis et al. (1986). It was suggested that, at 400° C, the platinum should hardly activate the combustion of methane, whereas other reducing gases, less stable than methane would be completely oxidized on the platinum filter.

2.4.2 Considerations based on principles

For the application around waste landfills in this study, continuous measurement of

atmospheric concentrations of CH₄ (2–100 ppm) is required. In terms of detectable gases and ranges, electrochemical, semiconductor and infrared sensors are applicable. In terms of selectivity, electrochemical and infrared sensors seem a better choice. If a sensor's selectivity is limited, the minimum requirement is the capability of differentiate CH₄ from the major components of the air and landfill gas, i.e., N₂, O₂, Ar, CO₂, Ne, and He. Effects of humidity, temperature and pressure may not be an issue because sensors will work under normal weather conditions. For continuous measurements, an infrared detector is the best choice since constant exposure to gases and extended chemical reactions involved in gas sensing by electrochemical and semiconductor sensors shorten their life span.

2.4.3 Commercially available methane analyzers

Literature that has reported direct measurements of fugitive methane commonly told that the required detection limit is < 2 ppmv. However, the instruments with sufficiently low detection ranges were too heavy, while portable one had a high detection range (Table 2.4).

Commercially available, light-weight (< 1 kg) methane detectors were summarized in Table 2.5. Among them, Testo Gas Detector was the best choice in terms of the detection range, response time, and sampling rate.

Table 2.4. Instruments for methane detection in literature.

| Reference | Analyzer | Principle | Range (ppmv) | |
|----------------------------|--|---|-----------------|---|
| Allen et al. (2019) | Los Gatos Research ultraportable greenhouse gas analyzer | Spectroscopy | < 30 | 15 kg CH ₄ , CO ₂ , H ₂ O |
| Mønster et al. (2015) | Picarro G2203 analyzer | Spectroscopy | 0.1-20 | 27.4 kg C ₂ H ₂ , CH ₄ , H ₂ O |
| Xu et al. (2014) | LI-COR Biosciences LI- 7700 | Spectroscopy | < 60 | (looks heavy) |
| Lavoie et al. (2015) | Picarro G2401-m | Spectroscopy | 2-3 | 31.75 kg CH ₄ , CO ₂ , CO, H ₂ O |
| Nathan et al. (2015) | Customized methane sensor | Spectroscopy | 2-5 | 3.1 kg |
| Yacovitch et al. (2015) | Picarro CRDS | Spectroscopy | 2-3 | CH ₄ , CO ₂ , H ₂ O |
| Johnson et al. (2015) | Eagle II methane detector (RKI Instruments) | Catalytic, spectroscopy, thermal conductivity | -4,000 | 1.72 kg Monitor up to 6 gases |
| Rella et al. (2015) | Picarro G2301 | Spectroscopy | 2-3 | 25.4 kg CH ₄ , CO ₂ , H ₂ O |
| Lan et al. (2015) | Picarro G2201-i and G2132-i | Spectroscopy | 2-15 | |
| Zhu et al. (2013) | GasFinder2.0 | Spectroscopy | 2-700 | 5 kg 6 gases STD and 4 gases custom |

Table 2.5. Specifications of commercial methane analyzers that weigh < 1 kg.

| Model | Testo Gas Detector | SKT-9300 | Aeroqual Series 500 | Gas Tiger 2000 |
|------------------------|--|--------------------|--|---|
| Manufacturer | Testo (Germany) | Testaution (China) | Aeroqual (New Zealand) | |
| Principle | Semiconductor | Electrochemical | Semiconductor | Infrared |
| Gas type | CH ₄ , C ₃ H ₈ , H ₂ | CH ₄ | CH ₄ , CO ₂ etc. (Interchangeable sensor head) | CH ₄ , CO ₂ , etc. (Multigas) |
| Range (ppm) | 1-999 1,000-44,000 | 5-50,000 | 0-10,000 | 0-10,000 0-50,000 |
| LDL (ppm) | 10 | | 10 | 50 |
| Resolution (ppm) | 1 | 5 | 1 | 1 |
| Response time (s) | 2–3 | 20 | 60 | 30 |
| Battery time (hr) | 8 | | 8 | 30 |
| Weight (kg) | 0.32 | 0.3 | 0.46 | 0.52 |
| Data logging | X | O | O | O |
| Pump | X | O | X | O |
| Continuous measurement | O (1 s) | | O (40 s) | O (1 s) |
| Protection | | IP66 | IP20 | IP66 |
| Stability | | | T/H effects Vibration can affect durability | T/H effects Vibration can affect durability |

2.5 Uncertainty propagation

With nonlinear transformation involved, it is difficult or impossible to find the probability density function of the derived quantities. In this case, approximations based on Taylor series expansion can be adopted to expect the mean and variance. The approximations are exact only for linear transformations. When $x = f(x_1, x_2, \dots, x_n)$,

$$\mu = f(\mu_1, \mu_2, \dots, \mu_n) + \frac{1}{2} \sum_{i=1}^n \sum_{j=1}^n \frac{\partial^2 f}{\partial x_i \partial x_j} \sigma_{ij} \quad (2.35)$$

$$\sigma = \sqrt{\sum_{i=1}^n \sum_{j=1}^n \frac{\partial f}{\partial x_i} \frac{\partial f}{\partial x_j} \sigma_{ij}} \quad (2.36)$$

If x_1, x_2, \dots, x_n are independent variables to one another, Equations (2.35) and (2.36) reduce to Equations (2.37) and (2.38), respectively (Ku, 1966):

$$\mu = f(\mu_1, \mu_2, \dots, \mu_n) + \frac{1}{2} \sum_{i=1}^n \frac{\partial^2 f}{\partial x_i^2} \sigma_i^2 \quad (2.37)$$

$$\sigma = \sqrt{\sum_{i=1}^n \left(\frac{\partial f}{\partial x_i} \right)^2 \sigma_i^2} \quad (2.38)$$

References

- Allen, G., Hollingsworth, P., Kabbabe, K., Pitt, J.R., Mead, M.I., Illingworth, S., Roberts, G., Bourn, M., Shallcross, D.E., Percival, C.J., 2019. The development and trial of an unmanned aerial system for the measurement of methane flux from landfill and greenhouse gas emission hotspots. *Waste Management* 87, 883-892.

Allen, M., Hollingsworth, P., Mead, I., Kabbabe, K., Roberts, G., Percival, C., 2016.

Measuring landfill methane emissions using unmanned aerial systems: field trial and operational guidance. Environment Agency: Horizon House, Deanery Road, Bristol, BS1 5AH.

Briggs, G.A., 1984. Plume rise and buoyancy effects. Atmospheric science and power production, 327-366.

Chou, J., 2000. Hazardous gas monitors: a practical guide to selection, operation and applications. McGraw-Hill Professional Publishing.

Czepiel, P., Shorter, J., Mosher, B., Allwine, E., McManus, J., Harriss, R., Kolb, C., Lamb, B., 2003. The influence of atmospheric pressure on landfill methane emissions. Waste Management 23, 593-598.

Fjelsted, L., Christensen, A., Larsen, J., Kjeldsen, P., Scheutz, C., 2019. Assessment of a landfill methane emission screening method using an unmanned aerial vehicle mounted thermal infrared camera—A field study. Waste Management 87, 893-904.

GIR, 2020. 2020 National greenhouse gas inventory report of Korea.

Gonzalez-Valencia, R., Magana-Rodriguez, F., Martinez-Cruz, K., Fochesatto, G.J., Thalasso, F., 2021. Spatial and temporal distribution of methane emissions from a covered landfill equipped with a gas recollection system. Waste Management 121, 373-382.

IPCC, 2000. Good practice guidance and uncertainty management in national

- greenhouse gas inventories. Intergovernmental Panel on Climate Change (IPCC), IPCC/OECD/IEA/IGES, Hayama, Japan.
- IPCC, 2006. 2006 IPCC guidelines for national greenhouse gas inventories. IGES, Japan.
- IPCC, 2019. Refinement to the 2006 IPCC guidelines for national greenhouse gas inventories. IPCC, Switzerland.
- Ishigaki, T., Yamada, M., Nagamori, M., Ono, Y., Inoue, Y., 2005. Estimation of methane emission from whole waste landfill site using correlation between flux and ground temperature. *Environ. Geol.* 48, 845-853.
- Jeong, S., Park, J., Kim, Y.M., Park, M.H., Kim, J.Y., 2019. Innovation of flux chamber network design for surface methane emission from landfills using spatial interpolation models. *Sci. Total Environ.* 688, 18-25.
- Johnson, D.R., Covington, A.N., Clark, N.N., 2015. Methane Emissions from Leak and Loss Audits of Natural Gas Compressor Stations and Storage Facilities. *Environ. Sci. Technol.* 49, 8132-8138.
- Ku, H.H., 1966. Notes on the use of propagation of error formulas. *Journal of Research of the National Bureau of Standards* 70, 263-273.
- Lan, X., Talbot, R., Laine, P., Torres, A., 2015. Characterizing Fugitive Methane Emissions in the Barnett Shale Area Using a Mobile Laboratory. *Environ. Sci. Technol.* 49, 8139-8146.
- Lavoie, T.N., Shepson, P.B., Cambaliza, M.O., Stirm, B.H., Karion, A., Sweeney,

- C., Yacovitch, T.I., Herndon, S.C., Lan, X., Lyon, D., 2015. Aircraft-Based Measurements of Point Source Methane Emissions in the Barnett Shale Basin. *Environ. Sci. Technol.* 49, 7904-7913.
- Lee, K., Jeon, E., Lee, Y., Park, J., 2020. Suggestions for the Estimation of the Methane Emission from a Landfill Site. *Journal of Urban Science* 9, 69-73.
- Logothetis, E., Hurley, M., Kaiser, W., Yao, Y., 1986. Selective methane sensors. *Proceedings of the 2nd International Meeting on Chemical Sensors, Bordeaux, France,*
- Mays, K.L., Shepson, P.B., Stirm, B.H., Karion, A., Sweeney, C., Gurney, K.R., 2009. Aircraft-based measurements of the carbon footprint of Indianapolis. *Environ. Sci. Technol.* 43, 7816-7823.
- Mitchell, A.L., Tkacik, D.S., Roscioli, J.R., Herndon, S.C., Yacovitch, T.I., Martinez, D.M., Vaughn, T.L., Williams, L.L., Sullivan, M.R., Floerchinger, C., Omara, M., Subramanian, R., Zimmerle, D., Marchese, A.J., Robinson, A.L., 2015. Measurements of methane emissions from natural gas gathering facilities and processing plants: measurement results. *Environ. Sci. Technol.* 49, 3219-3227.
- Mønster, J., Kjeldsen, P., Scheutz, C., 2019. Methodologies for measuring fugitive methane emissions from landfills—A review. *Waste Management* 87, 835-859.
- Mønster, J., Samuelsson, J., Kjeldsen, P., Scheutz, C., 2015. Quantification of methane emissions from 15 Danish landfills using the mobile tracer dispersion method. *Waste Management* 35, 177-186.

- Nathan, B.J., Golston, L.M., O'Brien, A.S., Ross, K., Harrison, W.A., Tao, L., Lary, D.J., Johnson, D.R., Covington, A.N., Clark, N.N., Zondlo, M.A., 2015. Near-Field Characterization of Methane Emission Variability from a Compressor Station Using a Model Aircraft. *Environ. Sci. Technol.* 49, 7896-7903.
- Oonk, H., 2010. Literature review: methane from landfills. Final report for Sustainable landfill foundation.
- Park, J.-K., Kang, J.-Y., Lee, N.-H., 2016. Estimation of methane emission flux at landfill surface using laser methane detector: Influence of gauge pressure. *Waste Manage. Res.* 34, 784-792.
- Pasquill, F., 1961. The estimation of the dispersion of windborne material. *Meteorol. Magazine* 90, 33-49.
- Rachor, I., Gebert, J., Gröngroft, A., Pfeiffer, E.M., 2013. Variability of methane emissions from an old landfill over different time-scales. *Eur. J. Soil Sci.* 64, 16-26.
- Raco, B., Battaglini, R., Lelli, M., 2010. Gas emission into the atmosphere from controlled landfills: an example from Legoli landfill (Tuscany, Italy). *Environmental Science and Pollution Research* 17, 1197-1206.
- Rella, C.W., Tsai, T.R., Botkin, C.G., Crosson, E.R., Steele, D., 2015. Measuring emissions from oil and natural gas well pads using the mobile flux plane technique. *Environ. Sci. Technol.* 49, 4742-4748.
- Ryzhikov, A., Labeau, M., Gaskov, A., 2009. Selectivity improvement of

- semiconductor gas sensors by filters. *Sensors for Environment, Health and Security*, 141-157.
- Seinfeld, J.H., Pandis, S.N., 2016. *Atmospheric chemistry and physics: from air pollution to climate change*. John Wiley & Sons.
- Shah, A., Allen, G., Pitt, J.R., Ricketts, H., Williams, P.I., Helmore, J., Finlayson, A., Robinson, R., Kabbabe, K., Hollingsworth, P., 2019. A near-field gaussian plume inversion flux quantification method, applied to unmanned aerial vehicle sampling. *Atmosphere* 10, 396.
- Shah, A., Pitt, J.R., Ricketts, H., Leen, J.B., Williams, P.I., Kabbabe, K., Gallagher, M.W., Allen, G., 2020. Testing the near-field Gaussian plume inversion flux quantification technique using unmanned aerial vehicle sampling. *Atmospheric Measurement Techniques* 13.
- Spokas, K., Bogner, J., Corcoran, M., Walker, S., Helmig, D., Bruhwiler, L., 2015. From California dreaming to California data: Challenging historic models for landfill CH₄ emissions. *California landfill emissions. Elementa: Science of the Anthropocene* 3.
- Turner, D.B., 1994. *Workbook of atmospheric dispersion estimates: an introduction to dispersion modeling*. CRC press.
- Wark, K., Warner, C.F., 1981. *Air pollution: its origin and control*.
- Xu, L., Lin, X., Amen, J., Welding, K., McDermitt, D., 2014. Impact of changes in barometric pressure on landfill methane emission. *Global Biogeochem. Cycles*

28, 679-695.

Yacovitch, T.I., Herndon, S.C., Petron, G., Kofler, J., Lyon, D., Zahniser, M.S., Kolb, C.E., 2015. Mobile Laboratory Observations of Methane Emissions in the Barnett Shale Region. *Environ. Sci. Technol.* 49, 7889-7895.

Zhang, H., Yan, X., Cai, Z., Zhang, Y., 2013. Effect of rainfall on the diurnal variations of CH₄, CO₂, and N₂O fluxes from a municipal solid waste landfill. *Sci. Total Environ.* 442, 73-76.

Zhu, H., Letzel, M.O., Reiser, M., Kranert, M., Bächlin, W., Flassak, T., 2013. A new approach to estimation of methane emission rates from landfills. *Waste management* 33, 2713-2719.

Chapter 3. Credibility of rotary UAV-based methane profile acquisition system

3.1 Introduction

Solid waste landfills are considered major sources of anthropogenic methane emission (Scheehle and Kruger, 2006), and methane is a major greenhouse gas (GHG) with a global warming potential 28 times that of carbon dioxide (Stocker et al., 2013). Landfill gas (LFG) is usually comprised of 45–60 % methane and 40–60 % carbon dioxide as a result of anaerobic degradation of organic matter (Theisen and Vigil, 1993). A large proportion of methane allows for LFG to be used as a clean energy source (Boyle, 1977), with an estimated fuel value of 18–22 MJ m⁻³ (Spokas et al., 2006). A major challenge in LFG management and utilization is the uncertainty in estimating LFG loss from a large area that may span hundreds of hectares (Amini et al., 2012; Amini and Reinhart, 2011). Without accurate quantification, it is not possible to develop appropriate policies and plans for LFG recovery. In addition, an international collaboration for GHG mitigation such as an emissions trading system will become ineffective under uncertainty (Rypdal and Winiwarter, 2001). However, current methods to quantify methane emissions from landfills are limited in terms of their accuracies (Allen et al., 2019).

Various methods have been used to estimate fugitive methane from landfills.

A significant portion of this chapter were published in the following article: Kim, Y.M., Park, M.H., Jeong, S., Lee, K.H., Kim, J.Y., 2021. Evaluation of error inducing factors in unmanned aerial vehicle mounted detector to measure fugitive methane from solid waste landfill, *Waste Management*, 124, 368–376.

The flux chamber method is the most popular as it does not require high-level of technology in practice compared to other methods such as micrometeorological method, or tracer plume measurement (Di Trapani et al., 2013; Klenbusch, 1986; Oonk, 2010). However, as the area coverage by the unit chamber is small, the flux chamber method requires labor and time-intensive efforts to cover the entire area. This limits the effectiveness of the method in field applications. The representativeness of the chamber method has also been criticized as the results are significantly affected by slight differences in chamber network design and operation (Börjesson et al., 2000). To deal with spatial heterogeneity, mobile measurement systems have been introduced. LFG sampling and measurement by automobiles has been investigated as an alternative method (Mønster et al., 2014; Mønster et al., 2015; Yacovitch et al., 2015). As automobiles require roads for operation, accessibility restriction was a major limitation. Methane detection using aircraft could be conceived for another alternative as this method has demonstrated successful methane detection in areas larger than a city (Lavoie et al., 2015; Mays et al., 2009); however, landfills are too small of an area to conduct aircraft-based measurements.

With the development of technology in unmanned aerial vehicles (UAVs), the use of UAVs in gas monitoring has recently been proposed as an up-shooting technology (Kersnovski et al., 2017; Rossi and Brunelli, 2015). Allen et al. reported examples of successful LFG measurement employing UAVs (Allen et al., 2014, 2016, 2019), where they measured carbon dioxide concentrations using a fixed-wing UAV. Then, these concentrations were converted to methane concentrations based on an empirical relationship between the compositions of the two gases. A potential to use the rotary wing UAV in LFG emissions monitoring was tested by Fjelsted et al. (2019)

and Shah et al. (2019). Fjelsted et al. (2019) conducted a field study to screen LFG emission hotspot using a thermal infrared camera mounted on a rotary UAV. Shah et al. (2019) showed the applicability of rotary UAV-based platform conveying air samples from 24 ± 3 m above the ground to a gas analyzer on the ground through the 150 m long tubing. The sampling method using tubing connected with a UAV was restricted to a space scale due to the connected tubing length. The limited spatial coverage for a single flight leads to temporal discontinuity between flight missions.

A UAV-mounted detector is able to extend the area of coverage for methane measurements in a single flight; this may enhance the degree of freedom in data acquisition. However, the applicability of direct methane measurement in the air using a UAV-mounted detector has not been fully assessed despite this potential. Recently, Shah et al. (2020) tested a prototype analyzer carried by a UAV in exterior experiments with controlled methane emissions. They calibrated the analyzer in the laboratory and reported that the tested instrument yielded successful results in estimating emission. To promote this relatively new method, there is a need for in-depth research addressing all potential error-inducing factors, as well as a successful showcase. The primary aim of this study is to propose and validate a fugitive methane measurement framework using a rotary UAV-mounted detector. The first specific objective of this study is to examine the impacts of error-inducing factors during measurement including the errors relating to the detector and flight condition. The second objective is determining means to minimize error originating from data handling. Concentration mapping supported by spatial interpolation is the most widely applied technique for data obtained from UAV field campaigns; thus, we defined the most preferable spatial interpolation method to assimilate UAV-derived

field data.

3.2 Materials and methods

3.2.1 Apparatus

Methane concentration was measured using a semiconductor-type real-time gas detector (Testo Gas Detector, Testo SE & Co. KGaA, Germany), and the Matrice 600 Pro (SZ DJI Technology Co., Ltd, People's Republic of China) was used for airborne methane monitoring. The specifications of the detector and UAV are summarized in Table 3.1. During flight missions, the detector was attached to the UAV, and detector readings were recorded by an installed camera. Readings from flights were corrected to account for response time.

The detector was placed at the center, 340 mm below the aircraft. There are a couple of options for the detector placement to minimize the effects of rotor turbulence. To place a detector or an air inlet outside the range of the rotor turbulence could be ideal options, but those options require compromises in terms of flight instability or response time. Another option is the center above or below the aircraft. Guo et al. (2020) showed through CFD analysis and experimental verification that air turbulence is insignificant at the centerline just above and below an aircraft in hover.

Table 3.1. Specification of the UAV and methane detector.

| | |
|------------------------------------|----------------|
| UAV: Matrice 600 Pro | |
| Rotor diameter | 540 mm |
| Overall diameter with rotors | 1,668 mm |
| Weight with the measurement system | 11.5 kg |
| Maximum takeoff weight recommended | 15.5 kg |
| Maximum velocity | 18 m/s |
| Wind speed limit* | 12 m/s |
| Maximum connection range | 3 km |
| Detector: Testo Gas Detector | |
| Weight | 0.32 kg |
| Concentration range | 10–40,000 ppmv |
| Resolution | 1 ppmv |
| Response time | 2–3 s |

* A rule of thumb says that a drone can be flown in wind speed up to two-thirds of its maximum speed.

3.2.2 Methane detector reliability test

The methane detector used in this study was not originally intended for outdoor atmospheric monitoring, rather for indoor gas leakage monitoring. As such, it was necessary to verify the performance of the detector for its given use. The device resolution was examined by conducting a laboratory-scale gas contact experiment. A standard gas with 44.05 vol% of methane was injected using a (micro)syringe into a cylindrical chamber equipped with the gas detector. When the chamber was opened, two valves allowed for gas injection, and when closed, these valves ensured the airtight sealing of the chamber. The volume of the chamber was approximately 20 L, and the volumes of the injected standard gas varied from 0.1 to 10 mL. Following gas injection, methane concentrations measured using the detector were recorded for 10 min. The test duration was determined based on a numerical simulation via

MATLAB 2017a in which the free diffusion of methane was assumed within a spherical space with an equivalent volume. When the molecular diffusivity of methane was set to $0.1942 \text{ cm}^2 \text{ s}^{-1}$ (Massman, 1998), the variation in methane concentration fell below 0.5 parts per million by volume (ppmv) at an elapsed time between 8 and 9 min (Fig. 3.1). Measured values during the final 1 min were averaged and compared with the intended concentrations.

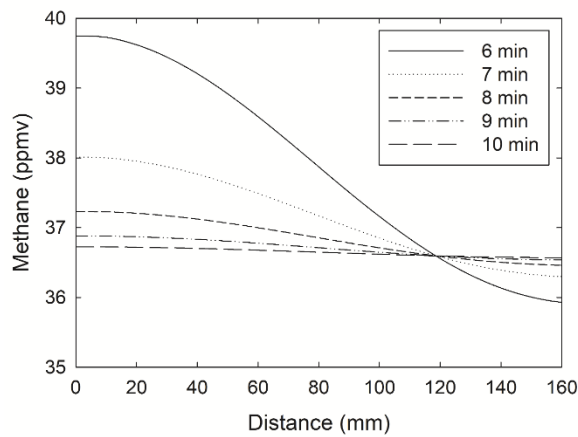


Fig. 3.1. Numerically simulated methane concentrations in a container, supposed that methane is introduced at the distance zero and the time zero.

3.2.3 Site specification of field measurement

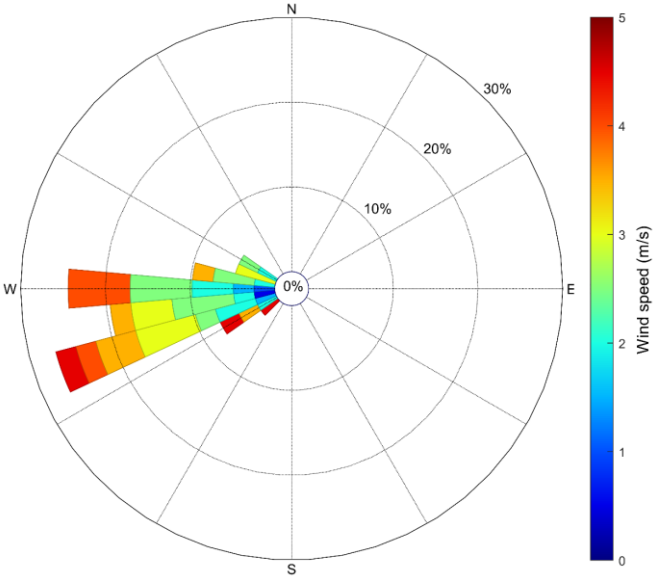
Field measurements were conducted around a cell with an area of approximately 9 ha located near the center of the second landfill site in Landfill S, South Korea; this is a major engineered landfill in South Korea. The whole area of the second landfill site spans 262 ha (Sudokwon Landfill Site Management Corporation, 2019). The site

received municipal solid waste from a large metropolitan area including Seoul, Incheon, and Gyeonggi-Province from October 2000 to October 2018, and is currently in after-care status. The overall landfill configuration was a mountain with a vast leveled top area and side slopes.

3.2.4 Flight mission for field measurement

Flight missions were conducted for approximately 40 min on November 22nd, 2018. The wind characteristics during the flight time were approximately 3 m/s from the west. Further meteorological data is provided in Table 3.2. Fig. 3.2 shows trajectories of two flight missions plotted by ArcGIS Pro 2.0 based on the global positioning system (GPS) data in automatically saved flight logs. Black and white points with gradation demonstrate the first mission, and red points with gradation demonstrate the second mission. The first mission was aimed at the horizontal mapping of the target cell approximately 10 m above the surface (Fig. 3.2b). The second mission was aimed at mapping the western vertical plane of the cell (Fig. 3.2c). The length and maximum height of the vertical plane in the second mission were 400 m and 20 m, respectively.

Table 3.2. Summary of meteorological data during the field measurement.

| | |
|-------------------------------|---|
| Average temperature | 6.1 °C |
| Average wind direction | 261.6° (W) |
| Average wind speed | 3.0 m/s |
| Wind rose |  |
| Relative humidity | 43.8 % |
| Pressure | 1025.2 hPa |

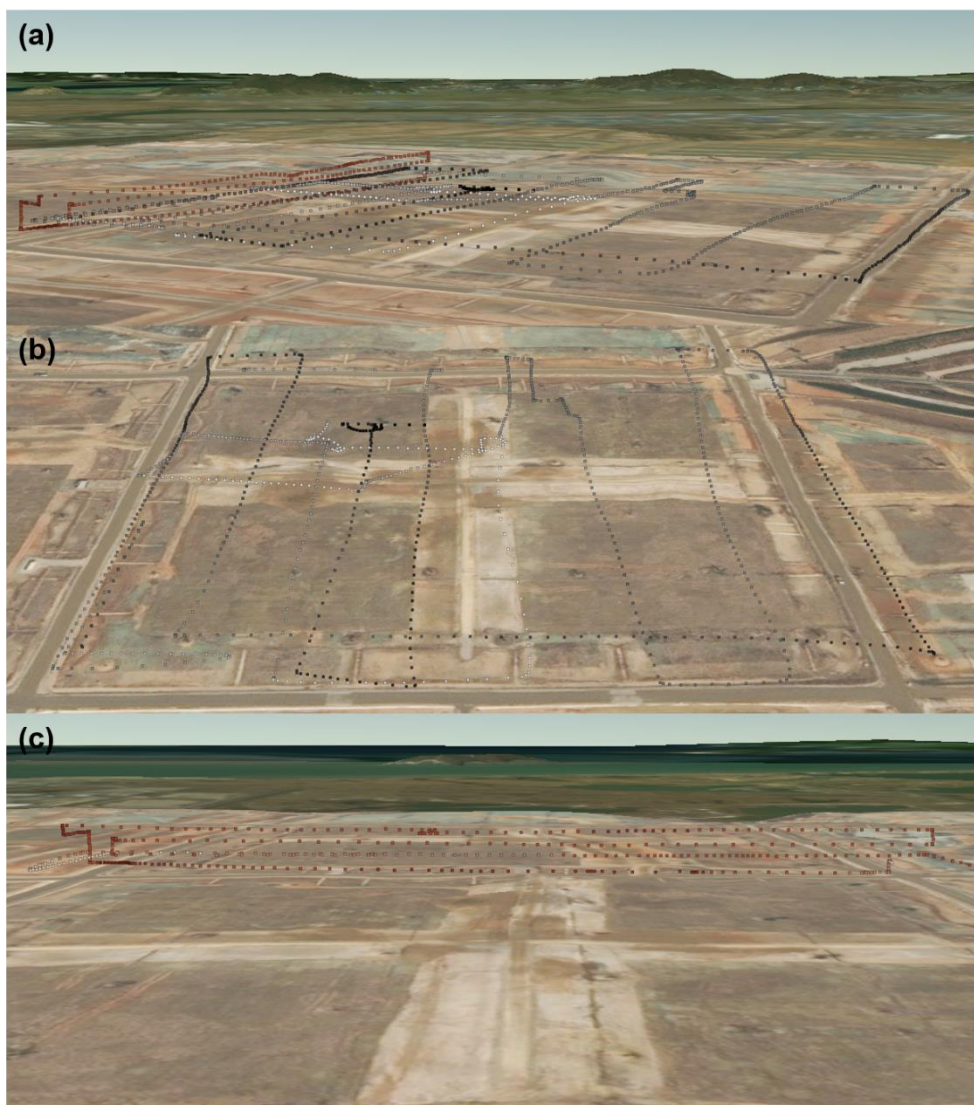


Fig. 3.2. Summary of flight mission and detected methane concentration ranges: (a) the whole flight mission, (b) horizontal mapping mission, and (c) vertical mapping mission. The deeper color indicates the higher concentration. Actual concentrations were not reported here as they are confidential data of Landfill S, South Korea.

3.2.5 Assessment of spatial interpolation

To estimate methane concentrations at locations other than sample points, spatial interpolation was conducted with methane concentrations obtained from field measurements. Six methods provided by ArcGIS Pro 2.0 were applied, and their interpolated results were compared. The six methods include diffusion interpolation with barriers (DIB), empirical Bayesian kriging (EBK), global polynomial interpolation (GPI), inverse distance weighted (IDW), local polynomial interpolation (LPI), and radial basis functions (RBF).

The best predictive model was determined based on measures of accurate prediction in cross-validation and visual inspection of the contour graphs. It has previously been reported that screening an appropriate spatial interpolation model based only on statistical measures cannot verify the optimal choice. As such, a visual inspection of the modeling results should be followed (Mitas and Mitasova, 1999). Cross-validation was conducted against spatial interpolation techniques using the methane concentration at position k , X_k (e.g., $k = 1, 2, 3, \dots, 100$), acquired by the field measurements in Section 3.2.4. The total X_k was divided into two subsets by random sampling, resulting in 80 % of the data as a modeling set and 20 % as a testing set: x_j (e.g., $j = 1, 2, 3, \dots, 80$) and y_i (e.g., $i = 1, 2, 3, \dots, 20$). The dataset, x_j was interpolated to predict methane concentrations at positions i , and predicted values were represented by f_i . To quantitatively assess prediction accuracy, four accuracy measures, including the coefficient of determination (R^2), mean absolute error (MAE), root mean square error (RMSE), and normalized root mean square error (NRMSE) were calculated as follows:

$$R^2 = 1 - \frac{\sum_{i=1}^n (y_i - f_i)^2}{\sum_{i=1}^n (y_i - \bar{y})^2} \quad (3.1)$$

$$\text{MAE} = \frac{\sum_{i=1}^n |y_i - f_i|}{n} \quad (3.2)$$

$$\text{RMSE} = \sqrt{\frac{\sum_{i=1}^n (y_i - f_i)^2}{n}} \quad (3.3)$$

$$\text{NRMSE} = \sqrt{\frac{\sum_{i=1}^n (y_i - f_i)^2}{\sum_{i=1}^n (y_i)^2}} \quad (3.4)$$

where n is the size of the testing dataset. Better prediction performance is indicated by an R^2 closer to 1, and other indices with smaller values.

3.3 Results and Discussion

3.3.1 Reliability of measurement system

The reliability of the measurement system is dependent on two factors; the reliability of the detector and stability of measured values during the flight. The first term is related to the calibration credibility and sensitivity of the detector, whilst the second term is associated with the effect of air advection due to the propellers. If air advection is significant, a temporary pressure change induces the measurement bias. This means that the measured value would not be able to represent the concentration at the measured location.

3.3.1.1 Credibility of methane detector

Fig. 3.3 shows the detector readings depending on the time and target methane concentration in a cylindrical chamber. The reading values changed with time and stabilized after approximately 9 min. Fluctuations over this protracted period of time

may be observed due to the slow diffusion of concentrated methane in the chamber and gradual response of the detector, the effects of which could not be separated in Fig. 3.3. Based on the theoretical diffusion time of 8–9 min (Fig. 3.1) and instrumental response time of 2–3 sec, it may be inferred that the time for gas homogenization accounts for the majority time. The readings observed from 9 to 10 min during each experiment were averaged as representative values. Fig. 3.4 presents plots of the target methane concentration and 1-min-averaged readings after stabilization. The calibration curve was divided into two plots to eliminate concerns associated with leverage due to points in the higher range (Cuadros-Rodríguez et al., 2007). The calibrations were conducted by weighting the dividing point to ensure the two calibration curves were continuous. Based on the linear regression, the methane detector showed credible methane readings with high coefficients of determination (R^2) for both low and high concentration ranges as follows:

$$y = 7.44 + 0.49 x \quad (x \leq 24 \text{ ppmv}, R^2 = 0.96) \quad (3.5)$$

$$y = 9.52 + 0.40 x \quad (x \geq 24 \text{ ppmv}, R^2 = 0.98) \quad (3.6)$$

where x is the actual methane concentration (ppmv), and y is the detector response (ppmv). The high correlation between these variables serves as evidence of the credibility of the methane detector.

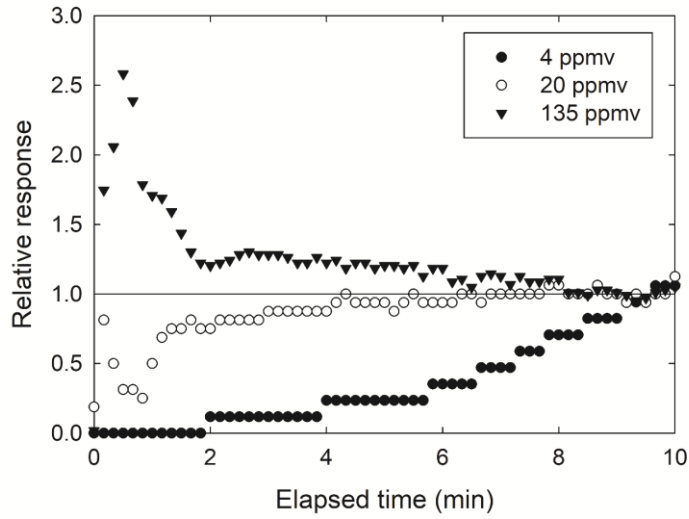


Fig. 3.3. Changes in detector response for 10 min following the injection of methane into the cylindrical chamber. The relative response indicates the detector reading relative to the average readings for the final one min.

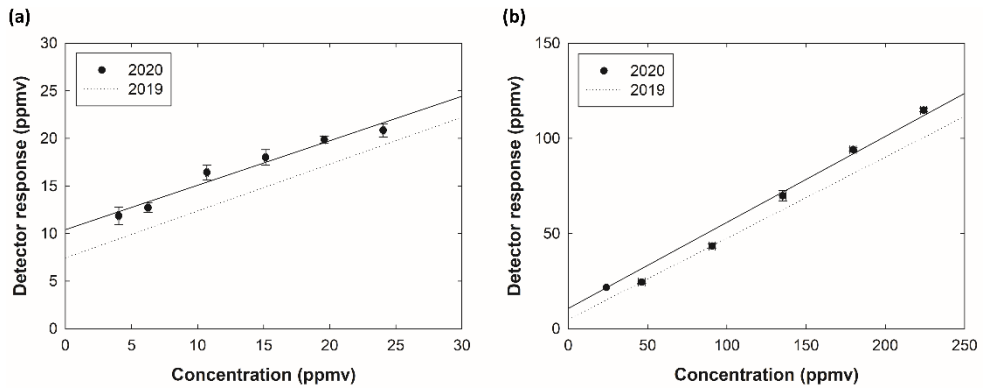


Fig. 3.4. Detector response to (a) low and (b) high concentrations of methane in the cylindrical chamber.

3.3.1.2 Critical velocity of UAV

The problem related to air advection driven by propeller rotation was verified based on classic fluid dynamics. Fig. 3.5 demonstrates the state of the UAV-based methane measurement system at times, t and $t + \Delta t$, where Δt is the time elapsed from time t . Let the displacement of a methane molecule near the propeller and that of the methane detector during Δt be Δh and Δl , respectively. The vertical motion of the UAV and the effect of natural wind were considered negligible. Then, the effect of advection from the propeller on the measurement system may be neglected when the following inequality is satisfied:

$$\Delta l > L, \text{ when } \Delta h = H \quad (3.7)$$

where L (m) is the horizontal distance between the detector and the end of the propeller; and H (m) is the vertical distance between the detector and the propeller.

If Δl is shorter than L , the dense air layer formed by advection will come into contact with the methane detector. In this case, the measured methane concentration will be affected by the variation in density, and the credibility of the measurement will be compromised. If Δl is longer than L , the detector will surpass the reach of air advection, and the effect of air advection on the measurement will be insignificant. This means there is a critical velocity of the UAV that ensures the reliability of the measurement system.

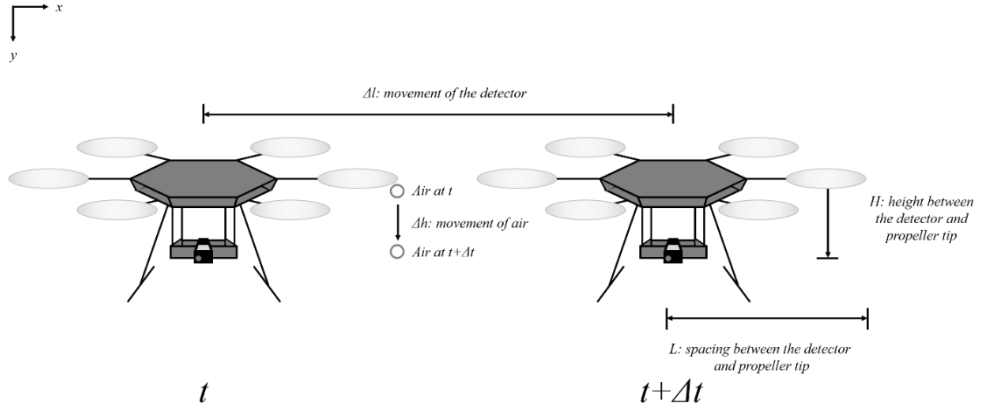


Fig. 3.5. Conceptual diagram of UAV-based methane measurement system at times, t and $t + \Delta t$ (UAV movement direction: x -axis).

Applying v_a (m/s) and v_d (m/s) as air and UAV velocities during the flight to Equation (3.7) yields the following condition:

$$v_d > v_a L H^1 \quad (3.8)$$

As such, the velocity of the UAV required to prevent the effect of advection by the propeller may be calculated using the aforementioned relationship.

To complete the formula, v_a needs to be defined; the control volume near a propeller was defined as shown in Fig. 3.6. According to impulse-momentum theorem (Street et al., 1996), the required net force, F , for the levitating UAV is summarized as follows:

$$F = \sum_{\text{downside}} Q \rho v - \sum_{\text{upper side}} Q \rho v \quad (3.9)$$

where Q (m^3/s), ρ (kg/m^3), and v (m/s) are the flow rate, density, and velocity of air,

respectively. As the velocity of air around the upper side of the propeller is assumed to be zero based on CFD simulation reported by Guo et al. (2020), and the required net force is equivalent to the weight of the UAV itself, Equation (3.9) may be converted to Equation (3.10):

$$m g = \sum_{\text{downside}} Q \rho v_a \quad (3.10)$$

where m (kg) is the mass of the UAV; and g (m/s²) is the gravitational acceleration (9.81 m/s²). The application of the continuity equation and the N -propeller condition yields Equation (3.11):

$$m g = N \rho A v_a^2 \quad (3.11)$$

where A (m²) is the area of the circle formed by the propeller during rotation. As such, the air velocity downside the propeller is expressed as follows:

$$v_a = \sqrt{\frac{m g}{N \rho A}} \quad (3.12)$$

Combining Equations (3.8) and (3.12) gives Equation (3.13):

$$v_d > \frac{L}{H} \sqrt{\frac{m g}{N \rho A}} \quad (3.13)$$

Applying all specifications of the UAV and air density (1.293 kg/m³ at 0 °C) shows that the UAV velocity required to ignore the wind effect was larger than 8.46 m/s at 0 °C. If the temperature effect is considered, the required velocity follows the inequality, as expressed by Equation (3.14):

$$v_d > \frac{L}{H} \sqrt{\frac{m g (T + 273)}{273 N \rho A}} \quad (3.14)$$

where T indicates the temperature in degrees Celsius. It may be practical to ignore the effect of humidity as v_d was observed to be relatively insensitive to humidity. The v_d distribution due to changes in temperature and humidity was calculated and depicted in Fig. 3.7. An increase in temperature and decrease in humidity makes the air lighter, leading to a larger v_d . The effect of humidity on critical velocity is much less significant. This is because 100 % of relative humidity is equal to the water saturation pressure (4.245 kPa at 30 °C (Wexler, 1976)), this is small compared to the atmospheric pressure.

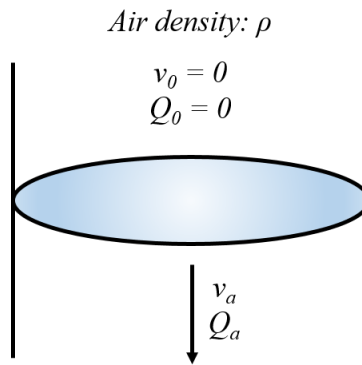


Fig. 3.6. Cylindrical control volume of air near a propeller.

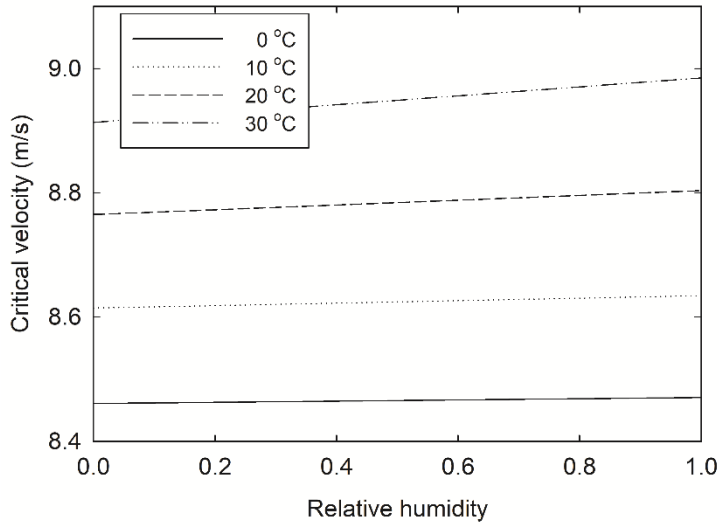


Fig. 3.7. UAV velocity required to ensure the measurement credibility depending on atmospheric temperature and humidity.

If the critical velocity is properly derived by Equation (3.14) and the UAV moves faster than the limit, the credibility of the methane detector reading is ensured. This indicates the elimination of the uncertainty associated with the potential that downwash air flow by rotary UAV influences the detector readings. When the rotary UAV moves forward, the front propellers rotate slower than the rear propellers to ensure thrust in the forward direction. The slower rotation of the front propellers creates weaker winds than v_a calculated using Equation (3.12). In addition, two studies in CFD simulation of downwash flow by a UAV showed that the downwash current slows after leaving the propeller due to the friction caused by mixing (Guo et al., 2020; Zheng et al., 2018). Therefore, the average velocity of the downwash airflow along with its streamline would be lower than v_a in Equation (3.12). This

means that v_d suggested by equation (3.14) was considered a conservative value.

3.3.1.3 Pressure on gas sensor by flight velocity

A semiconductor type gas sensor measures partial pressure using conductivity change of metal oxide caused by adsorption of gas molecules on the surface of the metal oxide (Chou, 2000; Ryzhikov et al., 2009). Such principle implies that a volumetric gas concentration would be overestimated with elevated pressure. Thus, pressure increase during flight needs to be estimated.

Pressure elevation relative to the atmospheric pressure was expected on the basis of the Bernoulli's equation. Supposed that a sensor is horizontally moving in the velocity of v and the air velocity at the surface of the sensor is zero, the Bernoulli's equation gives equation (3.15):

$$\Delta P = (\gamma v^2)/(2g) \quad (3.15)$$

where ΔP is the pressure elevation relative to the atmospheric pressure, and γ is the specific density of the air. Applying the flight velocity of 10 m/s, the additional pressure is expected to be 64.65 Pa, which is less than 0.1 % of the typical atmospheric pressure. Flying at approximately 90 m/s will make a significant pressure difference by 5 %, but that high flight velocity cannot be achieved by a current rotary UAV. Therefore, additional pressure on a gas sensor caused by flight velocity would have negligible effects on the sensor response.

3.3.2 Performance of the spatial interpolation models

The performance of the six spatial interpolation models, (i.e., DIB, EBK, GPI, IDW, LPI, and RBF), was evaluated using cross-validation and visual inspection. Table 3.3

shows the measures of predictive ability from the cross-validation in the horizontal and vertical mappings. In the case of horizontal mapping, LPI was the most optimum model, and EBK was the second-most optimum in terms of the accuracy indices, with the exception of MAE. For vertical mapping, EBK and LPI were the first and second-best interpolators, respectively, in terms of all the indices. To summarize, LPI and EBK were ranked as high priorities for the horizontal and vertical mappings in cross-validation.

Figs. 3.8 and 3.9 show the horizontal and vertical methane concentration profiles, respectively, estimated using the six spatial interpolation methods. These figures also include the standard error maps of EBK and LPI. The error maps were presented by these two methods only because the remaining methods were deterministic interpolators. In horizontal and vertical mappings, EBK, IDW, and RBF produced similar graphical expressions, while the DIB, GPI, and LPI predictions appeared discrete from the others. The poor fitness (Table 3.3) and the typical prediction surface (Figs. 3.8c and 3.9c) of GPI are apprehensible considering that GPI captures a large-scale pattern (ESRI, 2020c). This interpolator may be a good option to understand and remove global trends prior to spatial interpolation. The methane profiles produced by DIB appeared to be plausible. Although DIB refers to a heat equation analogous to molecular diffusion (ESRI, 2020b), it demonstrated relatively poor performance in cross-validation. IDW and RBF were other interpolators that produced plausible contour graphs, although they were not suitable for this application because of their exact interpolation (ESRI, 2020a). Generally, exact interpolators are not recommended for values involving measurement errors (Mitas and Mitasova, 1999).

Among the two best interpolators in cross-validation, LPI provided an unrealistic prediction surface (Figs. 3.8e and 3.9e). The predicted concentrations at some unmeasured locations far exceeded the range actually measured by the detector in the horizontal plane, and were six times higher than the highest one of measured values. Such extreme peaks led to steep slopes; this rarely occurs in gaseous matter that consistently experiences dispersion in the air. The interpolation results by LPI were associated with substantial uncertainty, comparable to the entire range of the estimated values (Figs. 3.8h and 3.9h). Due to such spurious discontinuities in concentration profiles and the huge uncertainty, it is inappropriate to employ LPI to estimate methane profiles and use the resulting information for further analysis or decision making. EBK displayed reasonable features with a close reproduction of the observed concentration range. Therefore, it was concluded that the most appropriate model to estimate methane concentration profiles was EBK for both horizontal and vertical planes.

Many researchers have utilized kriging to predict the spatial distribution of methane (Ishigaki et al., 2005; Mays et al., 2009; Nathan et al., 2015). However, the sound justification for the use of kriging has not yet been provided. An important feature of kriging is that it is a stochastic method distinct from the other deterministic methods tested in this study (Williams, 1998). It seems that the probabilistic motion of gas molecules may be better explained by a stochastic method opposed to a deterministic method. In addition to stochastic characteristics, the concept of spatial covariance that governs kriging (Matheron, 1963) is also parallel to the spatial continuity of gaseous matter distribution.

Table 3.3. Predictive performance of spatial interpolation methods in five times repeated cross-validation (mean \pm standard deviation).

| | Horizontal methane distribution | | | |
|-----|---------------------------------|-----------------|-----------------|-----------------|
| | R ² | MAE | RMSE | NRMSE |
| DIB | 0.51 \pm 0.05 | 2.95 \pm 0.10 | 3.79 \pm 0.19 | 0.58 \pm 0.02 |
| EBK | 0.78 \pm 0.06 | 1.30 \pm 0.20 | 2.45 \pm 0.36 | 0.37 \pm 0.05 |
| GPI | 0.02 \pm 0.00 | 4.39 \pm 0.12 | 5.17 \pm 0.21 | 0.79 \pm 0.01 |
| IDW | 0.71 \pm 0.07 | 1.56 \pm 0.22 | 2.80 \pm 0.38 | 0.43 \pm 0.05 |
| LPI | 0.81 \pm 0.04 | 1.32 \pm 0.16 | 2.28 \pm 0.21 | 0.35 \pm 0.03 |
| RBF | 0.74 \pm 0.06 | 1.61 \pm 0.18 | 2.66 \pm 0.35 | 0.41 \pm 0.05 |
| | Vertical methane distribution | | | |
| | R ² | MAE | RMSE | NRMSE |
| DIB | 0.40 \pm 0.22 | 3.27 \pm 0.83 | 4.53 \pm 1.13 | 0.41 \pm 0.10 |
| EBK | 0.80 \pm 0.07 | 1.75 \pm 0.25 | 2.63 \pm 0.42 | 0.24 \pm 0.04 |
| GPI | 0.01 \pm 0.02 | 4.51 \pm 0.30 | 5.90 \pm 0.33 | 0.53 \pm 0.03 |
| IDW | 0.58 \pm 0.07 | 2.65 \pm 0.13 | 3.92 \pm 0.17 | 0.35 \pm 0.02 |
| LPI | 0.73 \pm 0.07 | 1.97 \pm 0.21 | 3.00 \pm 0.36 | 0.27 \pm 0.04 |
| RBF | 0.58 \pm 0.09 | 2.63 \pm 0.15 | 3.85 \pm 0.40 | 0.35 \pm 0.03 |

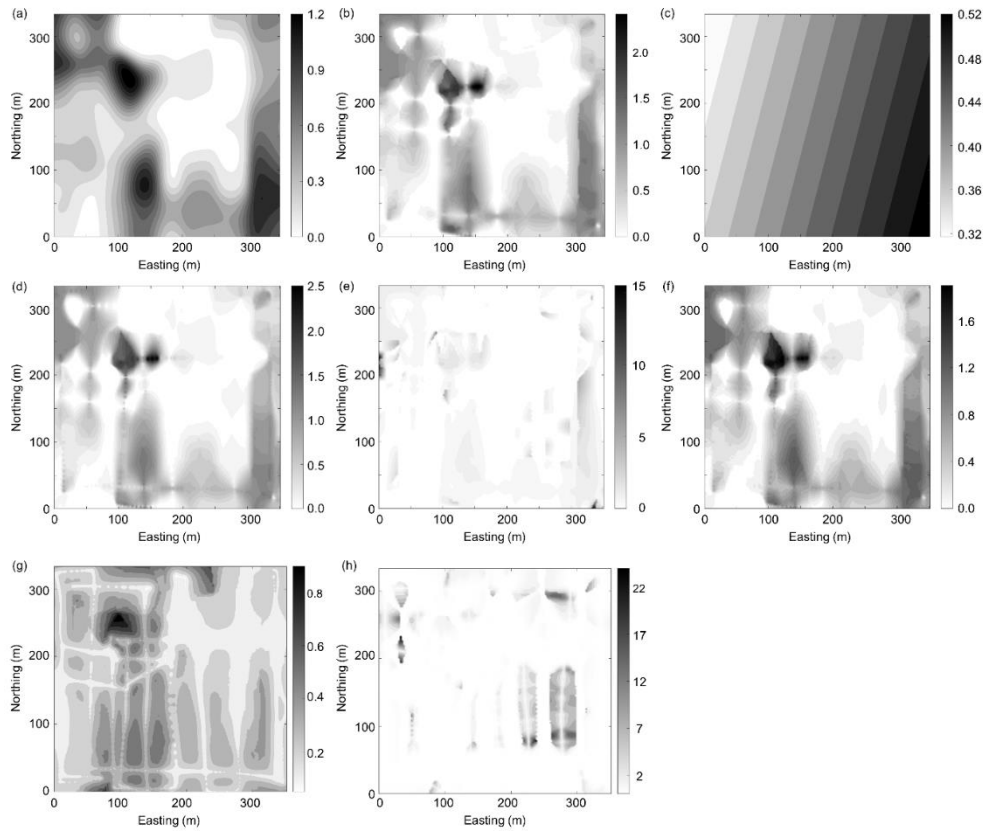


Fig. 3.8. Methane concentration profiles in a horizontal plane of 300 m \times 300 m depending on spatial interpolation methods: (a) DIB; (b) EBK; (c) GPI; (d) IDW; (e) LPI; (f) RBF; (g) EBK-standard error; and (h) LPI-standard error. The colors indicate methane concentrations. The concentrations are presented in relative values as they are the confidential data of Landfill S, South Korea.

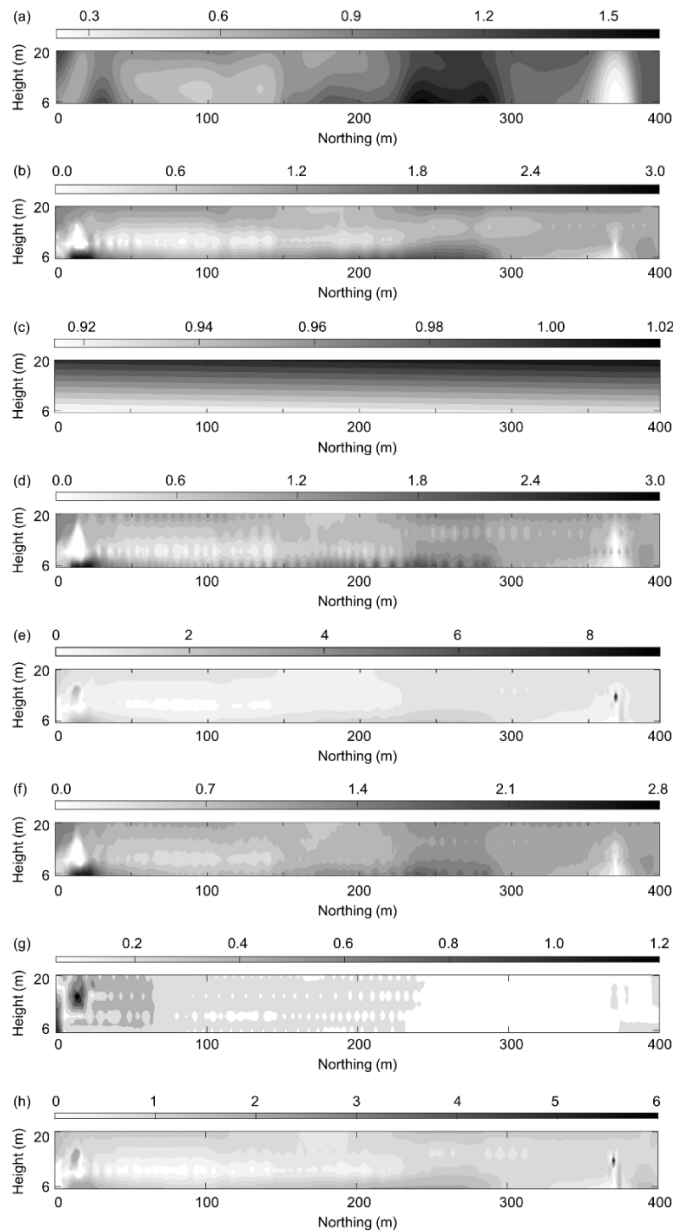


Fig. 3.9. Methane concentration profiles in a vertical plane that was 50 m high and 800 m long depending on spatial interpolation methods: (a) DIB; (b) EBK; (c) GPI; (d) IDW; (e) LPI; (f) RBF; (g) EBK-standard error; and (h) LPI-standard error. The colors indicate methane concentrations. The concentrations are presented in relative values as they are the confidential data of Landfill S, South Korea.

3.3.3 Methane distribution above landfill surface

It was observed from field measurements that the atmosphere near the landfill surface contained methane from < 3 ppmv to a few tens of ppmv. Sample points with methane concentrations indistinguishable from the background were 56.2 % and 85.7 % of the observations in the horizontal and vertical planes, respectively. Elevated concentrations (> 10 ppmv) were recorded at a small number of sample points (17.5 %) in the horizontal plane and at roughly half of the sample points (45.9 %) in the vertical plane.

Given the model selection (Section 3.3.2), the estimated concentration profiles by EBK were analyzed in detail to investigate the methane distribution characteristics. In the case of the horizontal plane (Fig. 3.8b), some regions showed relatively high methane concentrations compared to other areas. The appearances of dense methane regions suggest that the proposed methane measurement system may successfully discriminate spatial heterogeneity in gas emissions. This supports the applicability of the system for hotspot identification. The detection of hotspots is a key issue for accurate LFG estimation, efficient LFG recovery, and utilization. Traditional approaches such as the flux chamber method impose heavy burdens on labor and budget for hotspot identification. The use of a rotary UAV may be a cost-effective alternative. Locations of hotspots may possibly be identified by the proposed measurement system and reverse modeling, although the full description of the procedure is beyond the scope of this study.

For the vertical concentration profile (Fig. 3.9b), intense methane regions were located at low elevations, potentially indicating methane plumes moving near the

ground. A plume centerline rises due to the buoyancy driven by the temperature difference and the momentum driven by the gas exit velocity (Briggs, 1984; Turner, 1994). Assuming the relevant surface LFG flux and temperature for controlled landfills, the height of the rise is predicted to be approximately 1 m regardless of the downwind distance based on an equation by Turner (1994), and approximately 7 m at 150 m downwind based on an equation by Briggs (1984). Although the equations used are empirical and designed for a smoke plume from a stack, their comparisons provide meaningful outcomes. The prediction agrees with those observed in this study that the plume rise from the landfill surface was insignificant, emphasizing the importance of near-ground measurement. The next dense methane at a higher level may be attributed to the methane transported from upstream located sources. One of the commonly employed methods to estimate the total amount of fugitive gas is the downwind plume method. This method assumes that gas would largely transport along with the wind; as such the total gas emitted would pass through a vertical plane downstream of the landfill. To reduce uncertainties in this approach, the concentration variation should be measured upstream and downstream. Similar to the findings for the hotspot, a detailed description of the estimation of gas emission was not presented in this work but will be explored in our prospective study.

3.4 Summary

Many methods have been applied to monitor fugitive methane gas from landfills. Recently, there have been suggestions to use a framework utilizing an unmanned aerial vehicle (UAV) for landfill gas monitoring, and several field campaigns have proved that a rotary UAV-based measurement has advantages of ease of control and

high-resolution concentration mapping on the target planes. However, research on the evaluation of error-inducing factors in the suggested system is limited so far. This study prepared a measurement system with a lightweight methane detector and a rotary UAV to support the applicability of rotary UAV in landfill gas monitoring. Then, the validity of the system was tested experimentally and theoretically. In the detector reliability test, the methane detector had sufficient resolution for field application, and the critical UAV velocity required was obtained to ensure the credibility of the proposed measurement system. When spatial interpolators were applied to field data from the measurement system, the empirical Bayesian kriging demonstrated the best prediction of methane concentrations at unmeasured points. With the verifications provided in this study, this proposed method may contribute to reducing uncertainty in estimating fugitive landfill gas emission.

References

- Allen, G., Hollingsworth, P., Illingworth, S., Kabbabe, K., Perciva, C., 2014. Feasibility of aerial measurements of methane emissions from landfills. Environmental Agency: Rotherham, UK.
- Allen, G., Hollingsworth, P., Kabbabe, K., Pitt, J.R., Mead, M.I., Illingworth, S., Roberts, G., Bourn, M., Shallcross, D.E., Percival, C.J., 2019. The development and trial of an unmanned aerial system for the measurement of methane flux from landfill and greenhouse gas emission hotspots. *Waste Management* 87, 883-892.
- Allen, M., Hollingsworth, P., Mead, I., Kabbabe, K., Roberts, G., Percival, C., 2016.

- Measuring landfill methane emissions using unmanned aerial systems: field trial and operational guidance. Environment Agency: Horizon House, Deanery Road, Bristol, BS1 5AH.
- Amini, H.R., Reinhart, D.R., 2011. Regional prediction of long-term landfill gas to energy potential. *Waste Management* 31, 2020-2026.
- Amini, H.R., Reinhart, D.R., Mackie, K.R., 2012. Determination of first-order landfill gas modeling parameters and uncertainties. *Waste Management* 32, 305-316.
- Börjesson, G., Danielsson, Å., Svensson, B.H., 2000. Methane fluxes from a Swedish landfill determined by geostatistical treatment of static chamber measurements. *Environ. Sci. Technol.* 34, 4044-4050.
- Boyle, W., 1977. Energy recovery from sanitary landfills-a review, *Microbial Energy Conversion*. Elsevier, pp. 119-138.
- Briggs, G.A., 1984. Plume rise and buoyancy effects. *Atmos. Sci. Power Prod.* 850, 327-366.
- Chou, J., 2000. Hazardous gas monitors: a practical guide to selection, operation and applications. McGraw-Hill Professional Publishing.
- Cuadros-Rodríguez, L., Bagur-González, M.G., Sánchez-Vinas, M., González-Casado, A., Gómez-Sáez, A.M., 2007. Principles of analytical calibration/quantification for the separation sciences. *Journal of Chromatography A* 1158, 33-46.

Di Trapani, D., Di Bella, G., Viviani, G., 2013. Uncontrolled methane emissions from a MSW landfill surface: Influence of landfill features and side slopes. *Waste Management* 33, 2108-2115.

ESRI, 2020a. Classification trees of the interpolation methods offered in Geostatistical Analyst, <https://pro.arcgis.com/en/pro-app/help/analysis/geostatistical-analyst/classification-trees-of-the-interpolation-methods-offered-in-geostatistical-analyst.htm> (Access date: December 1, 2020)

ESRI, 2020b. How Diffusion Interpolation With Barriers works, <https://pro.arcgis.com/en/pro-app/help/analysis/geostatistical-analyst/how-diffusion-interpolation-with-barriers-works.htm> (Access date: December 1, 2020)

ESRI, 2020c. How global polynomial interpolation works, <https://pro.arcgis.com/en/pro-app/help/analysis/geostatistical-analyst/how-global-polynomial-interpolation-works.htm> (Access date: December 1, 2020)

Fjelsted, L., Christensen, A., Larsen, J., Kjeldsen, P., Scheutz, C., 2019. Assessment of a landfill methane emission screening method using an unmanned aerial vehicle mounted thermal infrared camera—A field study. *Waste Management* 87, 893-904.

Guo, Q., Zhu, Y., Tang, Y., Hou, C., He, Y., Zhuang, J., Zheng, Y., Luo, S., 2020. CFD simulation and experimental verification of the spatial and temporal distributions of the downwash airflow of a quad-rotor agricultural UAV in hover. *Comput. Electron. Agric.* 172, 105343.

- Ishigaki, T., Yamada, M., Nagamori, M., Ono, Y., Inoue, Y., 2005. Estimation of methane emission from whole waste landfill site using correlation between flux and ground temperature. *Environ. Geol.* 48, 845-853.
- Kersnovski, T., Gonzalez, F., Morton, K., 2017. A UAV system for autonomous target detection and gas sensing. 2017 IEEE aerospace conference, MT, USA, March 4-11, 2017.
- Klenbusch, M., 1986. Measurement of gaseous emission rates from land surfaces using an emission-isolation flux chamber. User's guide. Radian Corp., Austin, TX (USA).
- Lavoie, T.N., Shepson, P.B., Cambaliza, M.O., Stirm, B.H., Karion, A., Sweeney, C., Yacovitch, T.I., Herndon, S.C., Lan, X., Lyon, D., 2015. Aircraft-Based Measurements of Point Source Methane Emissions in the Barnett Shale Basin. *Environ. Sci. Technol.* 49, 7904-7913.
- Massman, W., 1998. A review of the molecular diffusivities of H₂O, CO₂, CH₄, CO, O₃, SO₂, NH₃, N₂O, NO, and NO₂ in air, O₂ and N₂ near STP. *Atmos. Environ.* 32, 1111-1127.
- Matheron, G., 1963. Principles of geostatistics. *Economic geology* 58, 1246-1266.
- Mays, K.L., Shepson, P.B., Stirm, B.H., Karion, A., Sweeney, C., Gurney, K.R., 2009. Aircraft-based measurements of the carbon footprint of Indianapolis. *Environ. Sci. Technol.* 43, 7816-7823.
- Mitas, L., Mitasova, H., 1999. Spatial interpolation. *Geographical Information*

- Mønster, J., Samuelsson, J., Kjeldsen, P., Scheutz, C., 2015. Quantification of methane emissions from 15 Danish landfills using the mobile tracer dispersion method. *Waste Management* 35, 177-186.
- Mønster, J.G., Samuelsson, J., Kjeldsen, P., Rella, C.W., Scheutz, C., 2014. Quantifying methane emission from fugitive sources by combining tracer release and downwind measurements - a sensitivity analysis based on multiple field surveys. *Waste Management* 34, 1416-1428.
- Nathan, B.J., Golston, L.M., O'Brien, A.S., Ross, K., Harrison, W.A., Tao, L., Lary, D.J., Johnson, D.R., Covington, A.N., Clark, N.N., Zondlo, M.A., 2015. Near-Field Characterization of Methane Emission Variability from a Compressor Station Using a Model Aircraft. *Environ. Sci. Technol.* 49, 7896-7903.
- Oonk, H., 2010. Literature review: methane from landfills. *Sustain. Landfill Found.*, 75.
- Rossi, M., Brunelli, D., 2015. Autonomous gas detection and mapping with unmanned aerial vehicles. *IEEE Trans. Instrum. Meas.* 65, 765-775.
- Rypdal, K., Winiwarter, W., 2001. Uncertainties in greenhouse gas emission inventories—evaluation, comparability and implications. *Environmental Science and Policy* 4, 107-116.
- Ryzhikov, A., Labeau, M., Gaskov, A., 2009. Selectivity improvement of semiconductor gas sensors by filters. *Sensors for Environment, Health and*

Security, 141-157.

Scheehle, E.A., Kruger, D., 2006. Global anthropogenic methane and nitrous oxide emissions. *Energy J.*, 33-44.

Shah, A., Pitt, J.R., Ricketts, H., Leen, J.B., Williams, P.I., Kabbabe, K., Gallagher, M.W., Allen, G., 2020. Testing the near-field Gaussian plume inversion flux quantification technique using unmanned aerial vehicle sampling. *Atmospheric Measurement Techniques* 13.

Spokas, K., Bogner, J., Chanton, J., Morcet, M., Aran, C., Graff, C., Moreau-Le Golvan, Y., Hebe, I., 2006. Methane mass balance at three landfill sites: What is the efficiency of capture by gas collection systems? *Waste Management* 26, 516-525.

Stocker, T.F., Qin, D., Plattner, G.-K., Tignor, M., Allen, S.K., Boschung, J., Nauels, A., Xia, Y., Bex, V., Midgley, P.M., 2013. *Climate change 2013: The physical science basis*. Cambridge University Press Cambridge.

Street, R.L., Watters, G.Z., Vennard, J.K., 1996. *Elementary Fluid Mechanics*, 7th ed. ed. John Wiley & Sons, New York.

Sudokwon Landfill Site Management Corporation, 2019. Year 2018 Sudokwon Landfill statistics yearbook. Sudokwon Landfill Site Management Corporation, Incheon, Korea.

Theisen, H., Vigil, S.A., 1993. *Integrated solid waste management: Engineering principles and management issues*. McGraw-Hill.

- Turner, D.B., 1994. Workbook of atmospheric dispersion estimates: an introduction to dispersion modeling. CRC press.
- Wexler, A., 1976. Vapor pressure formulation for water in range 0 to 100 C. A revision. J. Res. Natl. Bur. Stand. A 80, 775-785.
- Williams, C.K., 1998. Prediction with Gaussian processes: From linear regression to linear prediction and beyond, *Learning in Graphical Models*. Springer, pp. 599-621.
- Yacovitch, T.I., Herndon, S.C., Petron, G., Kofler, J., Lyon, D., Zahniser, M.S., Kolb, C.E., 2015. Mobile Laboratory Observations of Methane Emissions in the Barnett Shale Region. *Environ. Sci. Technol.* 49, 7889-7895.
- Zheng, Y., Yang, S., Liu, X., Wang, J., Norton, T., Chen, J., Tan, Y., 2018. The computational fluid dynamic modeling of downwash flow field for a six-rotor UAV. *Frontiers of Agricultural Science and Engineering* 5.

This page is intentionally left blank.

Chapter 4. Assessment of wind estimation using GPS/IMU data of a rotary UAV

4.1 Introduction

Information on wind is essential in quantifying gas emissions by mass balance approach. A common option is the tentative installation of an anemometer on a mast, in which the anemometer has to be portable and therefore there have to be some compromises in measurement accuracies. The accuracies can be aggravated in the course of a temporary installation because it can be hardly guaranteed that the sensors are placed at a certain height, in a certain direction. Another option is to refer to the wind data from verified weather stations, for example, a national meteorological monitoring station. Those data are highly reliable because their instruments are subject to be periodically examined and calibrated, but there is not always such a station near the site of interest. Besides, a common limitation of the two methods above is that they can measure wind only at a fixed height.

Wind speed varies with height because of the surface friction that is often enhanced by buildings or vegetation. As typical gradient heights—which mean the heights above ground where surface friction has a negligible effect on wind speed—are 457, 366, 274, and 213 m for a large city, suburb, open terrain, and open sea, respectively (Chen and Lui, 2005), there should be significant wind gradient below 50 m heights regardless of the type of terrain.

Ground-based remote sensing and weather balloons have been used to monitor meteorological variables over height. The employment of unmanned aerial vehicles

(UAVs) is an option to enable to effectively measure the changes with height. Although the development of UAVs technology has led to growth in meteorological sensors for UAVs mounting, wind sensors for UAVs are not as advanced as other meteorological sensors like temperature and pressure (Barbieri et al., 2019). That is because wind sensing adds a relative complexity in that it requires correcting the fuselage movement. UAV-based wind sensing techniques are classified into two types: direct and indirect methods. While wind sensors are mounted to a UAV in direct methods, indirect methods use the aircraft dynamics to estimate wind vectors. There is no consensus on which method is better. Donnell et al. (2018) showed that indirect methods provide better wind measurements in terms of error and bias whereas Barbieri et al. (2019) reported more consistent results with a direct approach.

This work tried estimating wind vectors using GPS and IMU data of UAV flights, and compared them to the wind data recorded by ground-based mechanical anemometers, to refine the estimation procedure and determine which methods to choose depending on the purpose.

4.2 Materials and Methods

4.2.1 Wind estimation using GPS/IMU of UAV

4.3.1.1 Apparatus

GPS and IMU of a UAV leave records as a log file including the operator's manipulation and the aircraft movement every 0.1 sec during flight. Records on the position, orientation, posture, and velocity of the aircraft were used to estimate wind speed and direction. Matrice 600 Pro (DJI, China) with the attachment for methane

measurement was used in this study.

4.3.1.2 Theory

The detailed estimation procedure was obtained by modifying the procedure suggested in Neumann et al. (2012). Throughout the procedure, directions are expressed as an angle between the direction of interest and the north, and the clockwise counts as the positive angle and vice versa. The method of wind estimation using GPS/IMU of UAV is based on the wind triangle (Fig. 4.1), in which an aircraft movement is determined by a driving force of the aircraft and a flow of the surrounding air:

$$\boldsymbol{w} = \boldsymbol{v} + \boldsymbol{u} \quad (4.1)$$

where \boldsymbol{w} is the ground vector, or the actual velocity; \boldsymbol{v} is the flight vector, that is, the velocity expected with the airframe posture and no external airflow assumed, and \boldsymbol{u} is the wind vector.

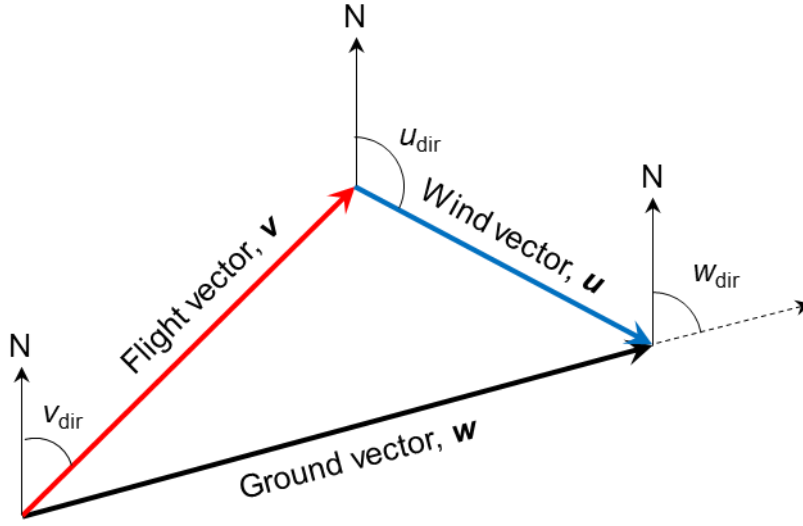


Fig. 4.1. The relationship between ground, flight, and wind vectors.

\mathbf{w} is known in forms of the northward speed, w_x and eastward speed, w_y in the flight log, and \mathbf{v} is inferred from the aircraft posture, i.e. pitch, roll and heading direction. The pitch, θ stands for the longitudinal tilt that is positive with the aircraft tilted backward (Fig. 4.2a). The roll, ϕ stands for the lateral tilt that is positive with the aircraft tilted to the right (Fig. 4.2b).

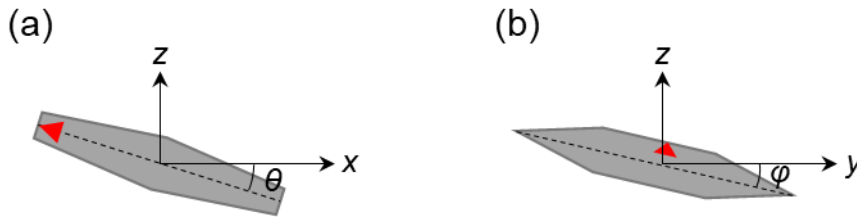


Fig. 4.2. The concept of pitch, θ (a) and roll, ϕ (b) of a UAV. The hexagon represents

a UAV advancing in the direction of the red arrow.

In mathematical expressions, $|\mathbf{v}|$ is related to the extent of the total tilt, ψ while the direction of \mathbf{v} , v_{dir} is related to the upward normal vector to the rotors plane and the heading direction. The detailed procedure is described below:

$$\mathbf{e}_{\text{pitch}} = (\cos\theta, 0, -\sin\theta) \quad (4.2)$$

$$\mathbf{e}_{\text{roll}} = (0, \cos\varphi, -\sin\varphi) \quad (4.3)$$

$$\mathbf{n} = \frac{\mathbf{e}_{\text{pitch}} \times \mathbf{e}_{\text{roll}}}{|\mathbf{e}_{\text{pitch}} \times \mathbf{e}_{\text{roll}}|} \quad (4.4)$$

$$\psi = \arccos(\mathbf{z} \cdot \mathbf{n}) \quad (4.5)$$

where \mathbf{n} is the unit normal vector against the plane with propellers, and \mathbf{z} is the unit vector in the direction of height or the z -axis.

$$\mathbf{n}_{xy} = \frac{(\mathbf{e}_{\text{pitch}} \times \mathbf{e}_{\text{roll}})_{xy}}{|(\mathbf{e}_{\text{pitch}} \times \mathbf{e}_{\text{roll}})_{xy}|} \quad (4.6)$$

$$\lambda = \begin{cases} \arccos(-\mathbf{x} \cdot \mathbf{n}_{xy}) & (n_y > 0) \\ -\arccos(-\mathbf{x} \cdot \mathbf{n}_{xy}) & (n_y < 0) \end{cases} \quad (4.7)$$

where \mathbf{n}_{xy} is the unit vector of \mathbf{n} onto the xy plane, n_y is the y component of \mathbf{n} , λ is the direction of total tilt, or the angular position of \mathbf{n} on the xy plane, and \mathbf{x} is the unit vector in the direction of the x -axis.

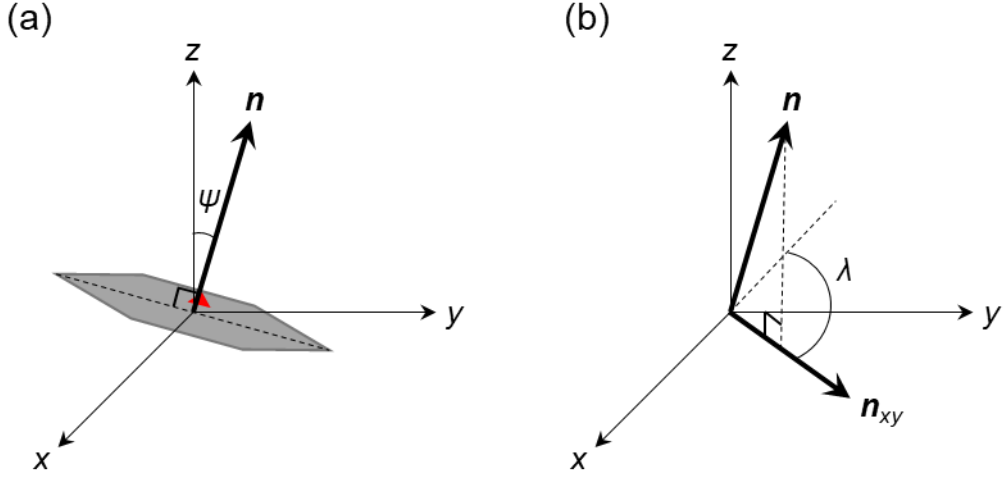


Fig. 4.3. The concept of total tilt, ψ (a) and direction of total tilt, λ (b) of a UAV. The hexagon represents a UAV advancing in the direction of the red arrow.

$$v_{\text{dir}} = \delta + \lambda \quad (4.8)$$

$$v_x = |\mathbf{v}| \cos v_{\text{dir}} \quad (4.9)$$

$$v_y = |\mathbf{v}| \sin v_{\text{dir}} \quad (4.10)$$

where δ is the heading direction, and v_x and v_y are the x and y component of \mathbf{v} , respectively. Then, \mathbf{u} can be obtained via the subtraction of the two vectors:

$$\mathbf{u} = \mathbf{w} - \mathbf{v} \quad (4.11)$$

$$u_{\text{dir}} = \begin{cases} 90^\circ - \arctan(u_x/u_y) & (u_y > 0) \\ 270^\circ - \arctan(u_x/u_y) & (u_y < 0) \\ 90^\circ & (u_x > 0, u_y = 0) \\ 270^\circ & (u_x < 0, u_y = 0) \end{cases} \quad (4.12)$$

where u_{dir} is the direction of the wind vector. Practically, the wind direction at a moment is exactly opposite to u_{dir} as the wind direction commonly refers to the direction from which the wind blows.

The unknown is the relationship between $|\mathbf{v}|$ and ψ , for which real experiments are required with a certain UAV. Theoretically, three types of forces are imposed on a flying UAV: gravitational force, thrust by propellers, and drag force.

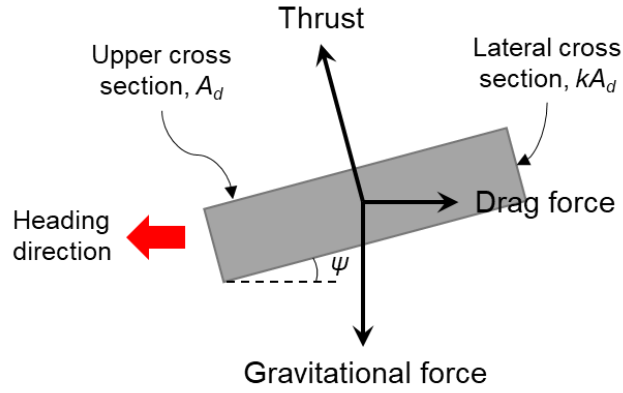


Fig. 4.4. Three types of forces imposed on a UAV flying to the left.

$$\text{Gravitational force} = W \quad (4.13)$$

$$\text{Thrust} = N \rho A v_a^2 \quad (4.14)$$

$$\text{Drag force} = C A_d \sin \psi \rho v^2 / 2 \quad (4.15)$$

where W is the weight of the aircraft, N is the number of rotors, ρ is the air density, A is the area that a propeller covers, v_a is the downward airspeed driven by rotors, C is the drag coefficient, and A_d is the cross-sectional area perpendicular to the flying

direction. If a UAV moves forward at a constant speed, the net force would equal to zero in both vertical and horizontal axis:

$$m g = N \rho A v_a^2 \cos \psi \quad (4.16)$$

$$C A_d (\sin \psi + k \cos \psi) \rho v^2 / 2 = N \rho A v_a^2 \sin \psi \quad (4.17)$$

By considering most parameters constant with a certain instrument and a short time-step, relationship between v_d and ψ can be found as follows:

$$v \propto \sqrt{\frac{\tan \psi}{\sin \psi + k \cos \psi}} \quad (4.18)$$

As more simplification, the thrust and the area under drag force could be additionally assumed as constant. Then, equation (4.18) comes into equation (4.19):

$$v \propto \sqrt{\tan \psi} \quad (4.19)$$

As presented in Fig. 4.5, both equations (4.18) and (4.19) produce curves with minimal disagreement. It is readily expected from the curve form that a UAV would move faster with a higher tilt, but to varying extents. Neumann et al. (2012) showed a similar curve that was obtained by experiments—without any theoretical consideration. Their curve had less curvature than the theoretical result and was fitted to the increasing part of a convex quadratic function. It was also showed that the head orientation and payload do not make a significant difference in the curve.

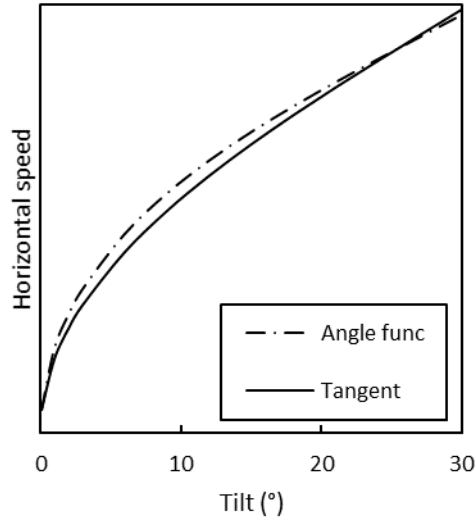


Fig. 4.5. Theoretically expected relation between horizontal speed and tilt of a UAV.

4.3.1.3 Data pretreatment

As a constant flight velocity is assumed in Section 4.3.1.2, datapoints at moments with significant acceleration or direction change were excluded in wind estimation. When wind vectors were estimated without the data screening, there appeared extremely large vectors. Also, most of them showed abnormal directions, which accorded with the direction of inertia expected with acceleration or deceleration.

Positioning and attitude data for each 0.1 s are available in a flight log, and their five-second averages were used for wind estimation to avoid excessive data load and to obscure the effects of immediate reactions of aircraft. Averaging directions like heading and flight directions requires cautions. For example, the arithmetic mean of 10° and 350° is 180° that is just opposite of the given two directions. To avoid that

kind of failure in averaging directions, angle wrapping into an appropriate range, or conversion between polar and Cartesian coordinate systems was employed.

```
% Acceleration
dataSize = size(data,1);
data.accel_mpss(1) = 0;
for i = 2:dataSize
    data.accel_mpss(i) = (data.ground_mps(i) - data.ground_mps(i-1))/0.1;
end

% Conversion head_deg and ground_rad for averaging
dir = data.head_deg;
dir = wrapTo360(dir) - 360 * (dir > 280);
data.head_deg = dir;

dir = data.ground_rad;
dir = wrapTo2Pi(dir) - 2*pi * (dir > 89*pi);
data.ground_rad = dir;
clear dir

% Exclude unnecessary rows
% direction change
for i = 1:dataSize-1
    if abs(data.head_deg(dataSize-i+1) - data.head_deg(dataSize-i)) > 0.2
        data(dataSize-i+1,:) = [];
    end
end

data = data(data.ground_mps > spdLim_mps, :); % too slow
data = data(data.pitch_deg < 0, :); % forwarding position
data = data(abs(data.zSpd_mps) < 0.3, :); % height change
data = data(abs(data.accel_mpss) < 1, :); % acceleration
dataSize = size(data,1);
```

Fig. 4.6. Excerpt of the MATLAB code run for data pretreatment in advance to wind vectors calculation.

```

%% Second averaging
vars = data.Properties.VariableNames;
data = varfun(@mean,data,...
    'InputVariables',vars,...
    'GroupingVariables','t_min');
% dataSize = size(data,1);

% Exclude unnecessary rows (criterion: group count)
data = data(data.GroupCount >= 5 * interval_sec,:);
data = removevars(data,{'t_min','GroupCount'});
data.Properties.VariableNames = vars;
dataSize = size(data,1);

%% Main code %%
for i = 1:dataSize
    % Flight direction
    vPitch = [cosd(data.pitch_deg(i)) 0 -sind(data.pitch_deg(i))];
    vRoll = [0 cosd(data.roll_deg(i)) -sind(data.roll_deg(i))];
    vn = cross(vPitch,vRoll) / norm(cross(vPitch,vRoll)); vn = sign(vn(3)) * vn;
    data.psi_rad(i) = acos(dot([0 0 1], vn));
    vnxy = [vn(1:2) 0]; vnxy = vnxy / norm(vnxy);
    data.lambda_rad(i) = sign(data.roll_deg(i)) * acos(dot([-1 0 0],vnxy));
    data.flight_rad(i) = wrapTo2Pi(deg2rad(data.head_deg(i)) + data.lambda_rad(i));

    % Flight length
    data.flight_mps(i) = flight_coef * rad2deg(data.psi_rad(i));

    % Wind vector
    [nFlight,eFlight] = pol2cart(data.flight_rad(i),data.flight_mps(i));
    nWind = nFlight - data.nSpd_mps(i); eWind = eFlight - data.eSpd_mps(i);
    [data.wind_rad(i),data.wind_mps(i)] = cart2pol(nWind,eWind);
end

```

Fig. 4.7. Excerpt of the MATLAB code for wind vectors calculation.

4.2.2 Mechanical anemometers

Meteorological data were obtained from two different sources using mechanical anemometers. Vantage Pro2 (Davis, USA) was temporarily installed on a three-meter-high mast at target sites. Major instrumental specifications are known as follows: threshold, 0.4 m/s; resolutions, 0.1 m/s and 22.5°; and data display every

one minute. Another dataset was provided by Korea Meteorological Administration (KMA). Most specifications are very similar to those of our temporary anemometer, except for higher resolution (0.1°) in wind direction.

4.2.3 Vertical wind gradient model

The power law is known to have been firstly proposed by Hellmann (1919). It is the most commonly used model to describe vertical wind speed gradient owing to its simplicity. The log-linear law by Monin and Obukhov (1954) is a more theory-based one that is expressed as a function of the friction velocity, the roughness length, and the air stability. Because much information required to determine the parameters in the log-linear equation is not always available, we employed the power law when needed. The power law is expressed as follows:

$$u = u_0 (z/z_0)^\alpha \quad (4.20)$$

where u and u_0 are the wind speeds at z and z_0 above ground, respectively, and α is the Hellman exponent.

4.2.4 Comparative experiments

4.2.4.1 Near-field comparison

The temporary anemometer was installed at the edge of a roof at the Seoul National University (Seoul, Republic of Korea) and the UAV was flown at the same height and the distance < 150 m in December 2020 for a near-field comparison. During the experiments, the air temperature and pressure were $9.0\text{--}12^\circ\text{C}$ and $1,008.4\text{--}1,008.8$ bar.



Fig. 4.8. UAV flight trajectory (yellow line) and Davis installation position (red circle) for preliminary experiments on the Google satellite image.

4.2.4.2 Field campaigns

During field campaigns at a coastal area in Dangjin, the Republic of Korea, in May and October 2020, wind data were collected simultaneously from UAV, Davis, and KMA. A coastal area with sparse buildings was chosen where there would be a relatively consistent wind field. The topography of the site adjacent to the sea in the Northwest says that there would be a high possibility of a northwest wind, parallel to the sea breeze, during the day (Abbs and William, 1992). Davis was installed at the edge of a roof at approximately 10 m height when available, otherwise, on the top of a three-meter mast on the ground. UAV was flown at heights from 5 to 120 m

at distances < 500 m from the location of Davis. KMA provides meteorological data measured at 10 m height at the weather station approximately 10 km away from the site.



Fig. 4.9. Wind measurement locations in the satellite image of the field campaign site. Yellow solid lines include flight trajectories of UAV, and red arrows on vertical sticks indicate the locations for Davis.

4.3 Results and Discussion

4.3.1 Relationship between flight speed and tilt of UAV

We tried to find out the relationship between the flight speed ($|v|$) and total tilt (ψ) of the aircraft using data collected by simultaneously operating the anemometer and UAV. The plot of $|v|$ versus ψ confirmed an obvious trend in which $|v|$ increases with larger ψ (Fig. 4.10). However, it was unexpected that the trend best follows a simple proportional relationship among the types of curves tested. The proportional, linear, power, and tangential equations were fitted to the data with adjusted R^2 of 0.64, 0.52, 0.17, and 0.40, respectively. The proportional form looked most suitable in Fig. 4.10 as well.

Theoretically expected upward convexity could not be found mainly due to the highly scattered data points. Difference in the sampling rate between the UAV and the anemometer is the principal contributor to the deviation. While wind and the airframe attitude constantly change, Davis can provide wind data only at one-minute interval. Additional factors include the reaction time delayed by the heavy airframe relative to rapidly changing wind. Neumann et al. (2012) presented the flight speed-tilt curve with slight convexity and small deviations. It would have been possible because they conducted experiments with a much smaller UAV and air speed controlled in a wind tunnel.

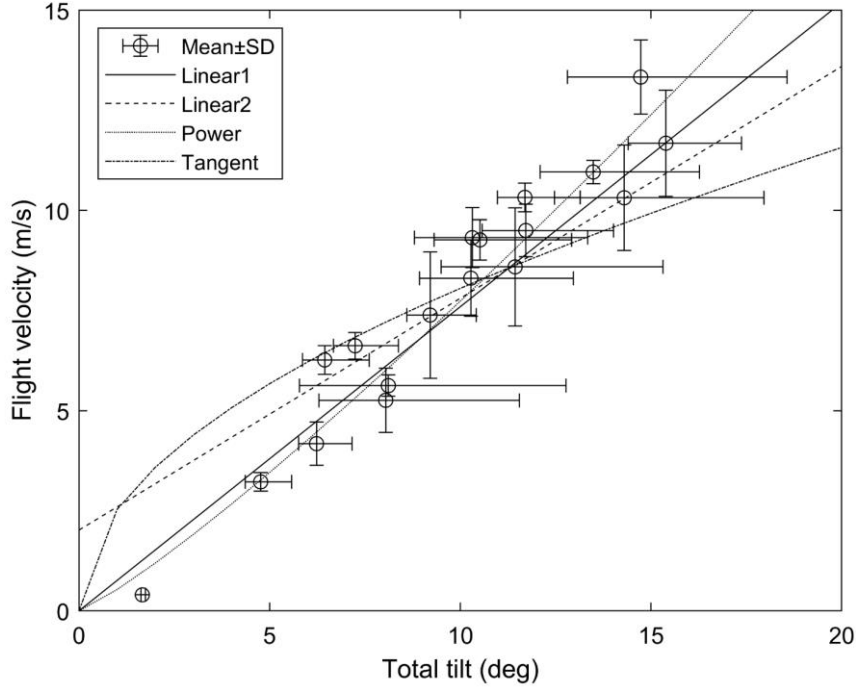


Fig. 4.10. Flight velocity at varying tilt of the UAV resulted from near-field experiments with the UAV and Davis.

4.3.2 Comparison of wind determined by UAV and anemometer

Average wind speeds and directions determined by UAV and Davis in near-field experiments were summarized in Table 4.1. The average directions did not show a significant difference ($p = 0.36$). Average speeds differ with significance ($p = 0.0016$), which is contributed to the starting threshold of Davis. To be detected by a mechanical anemometer, wind need to be stronger than its threshold to overcome the physical friction. The first half of the experimental duration with wind not detected by Davis would be long enough to lower the average speed (Fig. 4.11a). This

speculation appears to make sense in that the average speeds were not statistically different ($p = 0.21$), when excluding the duration when wind was not detected by Davis. Therefore, it could be concluded that the two wind determination methods produce consistent results. Fig. 4.11 shows that trends in wind speed variation with time follow each other as well, which was also supported by the result of paired t -test that the difference was statistically insignificant ($p = 0.77$).

Table 4.1. Average wind determined by different determination methods in near-field experiments.

| | For whole duration | | Excluding duration with zero wind by Davis | |
|-------|--------------------|------------|--|------------|
| | Speed (m/s) | Direction | Speed (m/s) | Direction |
| Davis | 0.5 | 239° (WSW) | 1.0 | 239° (WSW) |
| UAV | 0.8 | 223° (SW) | 1.1 | 251° (WSW) |

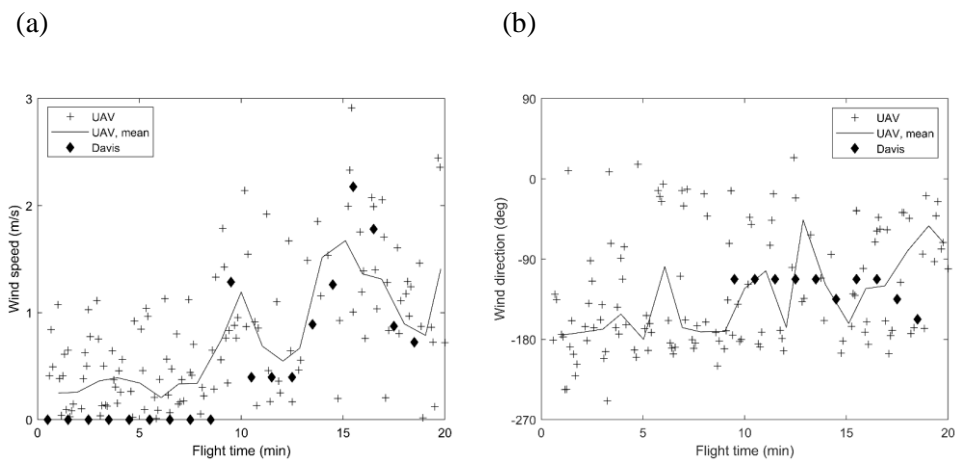


Fig. 4.11. Time variance in wind speed (a) and wind direction (b) determined by UAV-based estimation and Davis anemometer.

It was observed that UAV-estimated wind vectors more strongly deviate (Figs. 4.11 and 4.12). A hypothesis explaining the larger variation is that, despite of data screening against significant acceleration, acceleration in flight directions still could contribute to the estimated wind vectors. The UAV wind rose shows that the aspect of its spread out is consistent with the dominant flight direction (Figs 4.12b and. 4.8). This effect may be more noticeable due to weak wind field during the experiments. The hypothesis will be supported in the following section by comparing wind roses in different cases. Nevertheless, because acceleration took place to both directions during round-trip flight, the false components by acceleration would be cancelled out in averaging wind vectors to result in agreement in the average speed and direction.

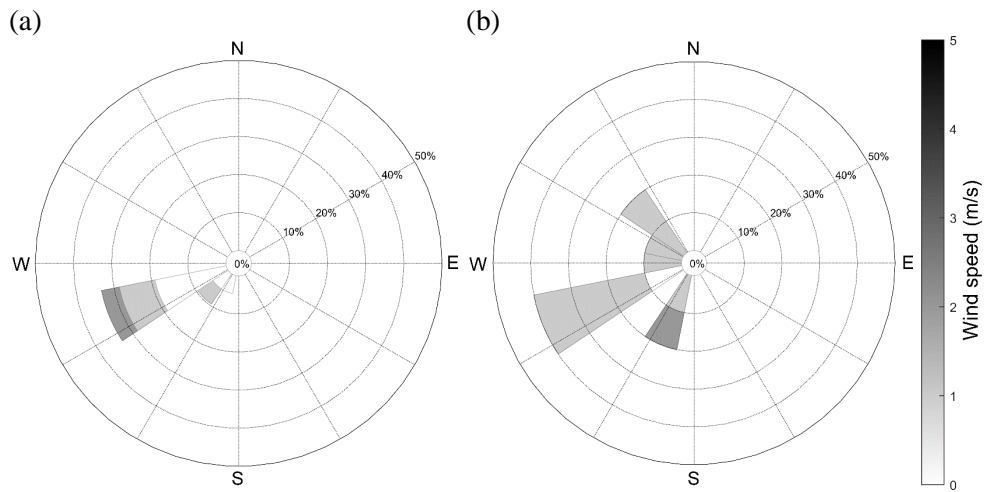


Fig. 4.12. Wind rose measured by Davis (a) and estimated by UAV-based method (b) in near-field experiments.

From the concurrent operations of the UAV and mechanical anemometer in near field, we achieved coherent average values, time variations, and distributions in both wind speed and direction. This says that the method of wind estimation using GPS/IMU data of UAV can replace a ground-based anemometer with a satisfying capability.

4.3.3 Vertical wind gradient by UAV-assisted wind estimation

Using the UAV-based wind estimation method, five-second-averaged wind speeds and directions were calculated from field campaigns. To explore vertical wind gradient, the wind estimates were grouped by heights at five- or ten-meter intervals. Box plots of wind speeds in Fig. 4.13 clearly evidence wind speed increasing with height. An exception is the case of 2020 0219 am (Fig. 4.13a), in which there is no statistical difference in mean wind speeds of different heights (one-way ANOVA, $p = 0.080$). In the whole field campaigns, 13 of 16 cases present significant wind gradient in terms of speed (Table 4.3).

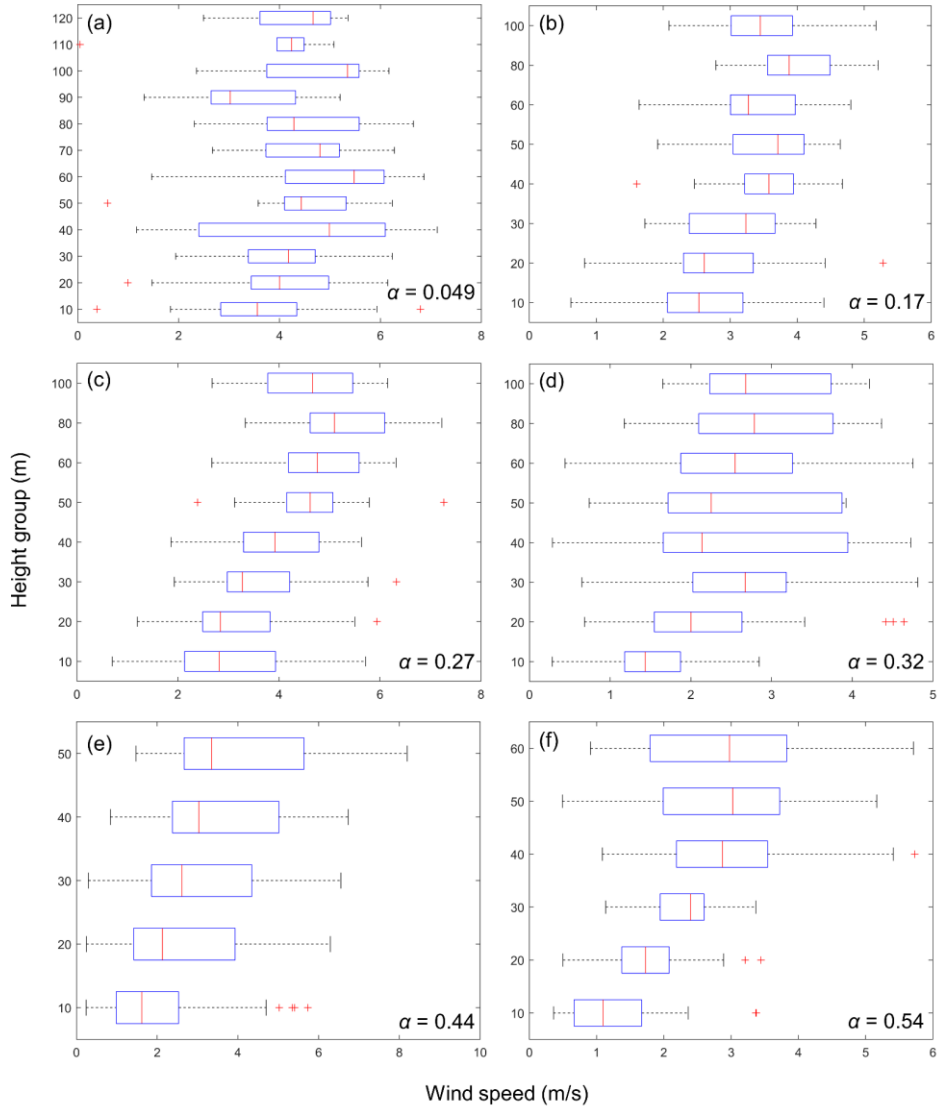


Fig. 4.13. Wind speed at different heights and Hellman exponent, α : (a) 2020 0219 am; (b) 2020 1021 am; (c) 2020 1021 pm; (d) 2020 1020 pm; (e) 2019 0416 pm; and (f) 2020 0218 pm.

Hellman exponents range from a negative value up to 0.65 (Table 4.3). Compared to the typical values of Hellman exponent (Table 4.2), the exponents of

11 cases fall in a probable range for the coastal area with sparse habitation (0.09–0.54). The values estimated in this study have comparatively wide range possibly because the typical Hellman exponents were suggested generally on the basis of long term average. Donnou et al. (2019) investigated month-averaged wind gradient at a coastal area by operating radiosonde at heights from 10 to 60 m for four years, and obtained Hellman exponent in a range of 0.10-0.25. Such a variability of Hellman exponent values that were acquired through 16 measurements at the identical site also emphasize the importance of timely observing wind gradient. It would not be a good option to pick a typical parameter to simulate vertical wind gradient.

Table 4.2. Typical values of the Hellman exponent depending on the location and air stability (Kaltschmitt et al., 2007).

| Air stability | Unstable | Neutral | Stable |
|----------------------|-----------------|----------------|---------------|
| Open water | 0.06 | 0.10 | 0.27 |
| Flat open coast | 0.11 | 0.16 | 0.40 |
| Human inhabited area | 0.27 | 0.34 | 0.60 |

Unlike wind speeds, there was no difference in wind directions between heights in 10 of 16 cases (Table 4.3). Even when there was statistically significant difference, the deviation from the overall average direction rarely exceed 15°.

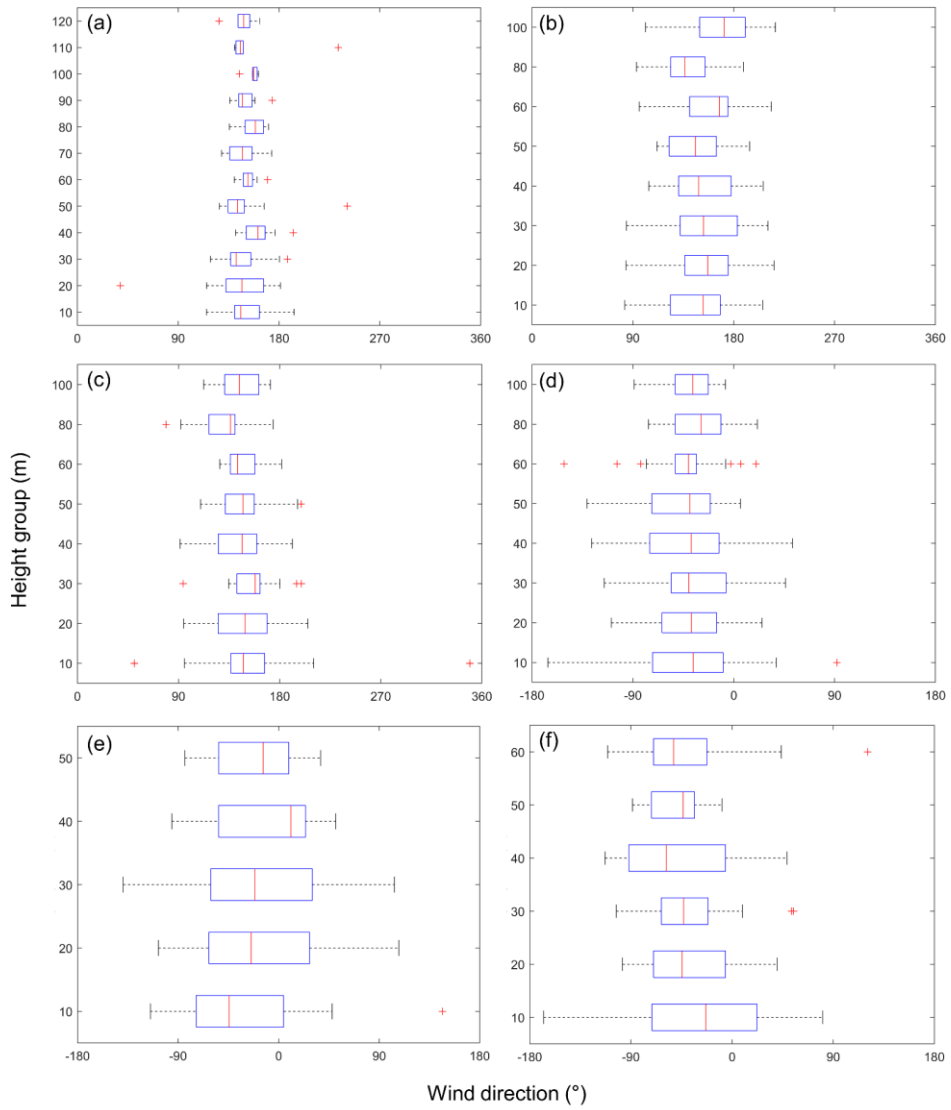


Fig. 4.14. Wind direction at different heights: (a) 2020 0219 am; (b) 2020 1021 am; (c) 2020 1021 pm; (d) 2020 1020 pm; (e) 2019 0416 pm; and (f) 2020 0218 pm.

Table 4.3. Summary of wind estimation from field campaigns.

| Area | Case | T (°C) | P (hPa) | Cloud cover | Average wind | | α | <i>p</i> -value in ANOVA** | |
|---------------------|-----------------|-----------|------------|----------------|-----------------|-----------------|----------|----------------------------|-----------|
| | | | | | Speed* (m/s) | Direction | | Speed | Direction |
| Flat open coast | 2020 0218 am | 0.5 | 1028.3 | 0.16 | 2.3 | 328.4° (NNW) | 0.12 | 2.26e-02* | 1.01e-01 |
| | 2020 0511 am | 18.6 | 1010.4 | 0.50 | 2.1 | 337.1° (NNW) | 0.07 | 2.37e-01 | 7.18e-03* |
| | 2020 1020 am | 19.6 | 1028.0 | 0.40 | 2.7 | 325.3° (NW) | 0.09 | 5.97e-01 | 2.93e-01 |
| Sparse buildings | 2019 0416 pm | 20.0 | 1015.1 | 0.44 | 1.4 | 322.9° (NW) | 0.44 | 1.62e-05* | 1.49e-01 |
| | 2019 0830 am | 24.6 | 1009.6 | 0.35 | 2.2 | 306.2° (NW) | 0.65 | 2.58e-04* | 5.24e-01 |
| | 2020 0218 pm | 1.4 | 1028.0 | 0.16 | 1.0 | 314.2° (NW) | 0.54 | 1.92e-11* | 5.64e-01 |
| | 2020 0219 am | 4.5 | 1030.9 | 0.66 | 3.8 | 150.4° (SSE) | 0.05 | 7.97e-02 | 4.24e-01 |
| | 2020 0219 pm | 7.6 | 1029.3 | 0.66 | 2.6 | 23.5° (NNE) | 0.01 | 2.38e-02* | 2.97e-02* |
| | 2020 0220 am | 7.8 | 1034.8 | 0.40 | 2.1 | 355.7° (N) | -0.26 | 6.02e-05* | 1.75e-03* |
| | 2020 0220 pm | 9.8 | 1033.2 | 0.40 | 1.5 | 340.2° (NNW) | 0.25 | 8.59e-22* | 4.81e-01 |
| | 2020 0511 pm | 19.2 | 1007.9 | 0.50 | 1.6 | 280.5° (W) | 0.26 | 9.43e-05* | 1.62e-02* |
| | 2020 0512 am | 16.9 | 1004.1 | 0.23 | 5.7 | 228.4° (SW) | 0.21 | 1.77e-07* | 8.09e-01 |
| | 2020 0512 pm | 17.6 | 1004.8 | 0.23 | 4.8 | 260.4° (W) | 0.18 | 3.36e-14* | 2.36e-03* |
| | 2020 1020 pm | 18.4 | 1026.0 | 0.40 | 1.4 | 323.7° (NW) | 0.32 | 8.71e-05* | 8.13e-01 |
| | 2020 1021 am | 15.5 | 1021.1 | 0.84 | 2.3 | 154.4° (SSE) | 0.17 | 2.07e-11* | 1.35e-02* |
| | 2020 1021 pm | 17.1 | 1017.3 | 0.84 | 2.6 | 146.5° (SSE) | 0.27 | 5.77e-18* | 7.75e-02 |

* At 10 m height.

** The null hypothesis, “all means are equal throughout heights,” was rejected at a significance level of 0.05.

4.3.4 Correlation analysis

Relationships between multiple variables from the field campaigns were investigated to acquire some insights (Fig. 4.15). A strong correlation was found in cloud coverage versus wind direction. The day with low to moderate cloud coverage tended to have wind blown from the Northwest, which is understandable based on the terrain and the principle of sea breeze. Weak correlations involving cloud coverage may support that with less cloud or northwest wind, there would be higher probability of larger Hellman exponent, and significant height-dependency in wind speed but not in wind direction, which altogether agree with conditions of stable atmosphere with less turbulence. In that these correlations are in line with the well-known theories pertaining to atmospheric dynamics, they add an indirect evidence to validate the wind estimation method.

As another strong correlation, the positive correlation between two p values of ANOVA testing time variability in wind speed and direction would imply that both speed and direction are likely to vary with time when there is significant time variability in wind field. In the light of a weak but meaningful correlation between p values of ANOVA testing wind speed difference relative to time and height, it could be said that a change in wind speed over time would have contributed to the speed difference by height in some cases. In other words, the wind estimation method cannot distinguish time effects and position effects, which may be a limitation of the method. Still, the influence of the limitation can be minimized through the short duration of a single measurement.

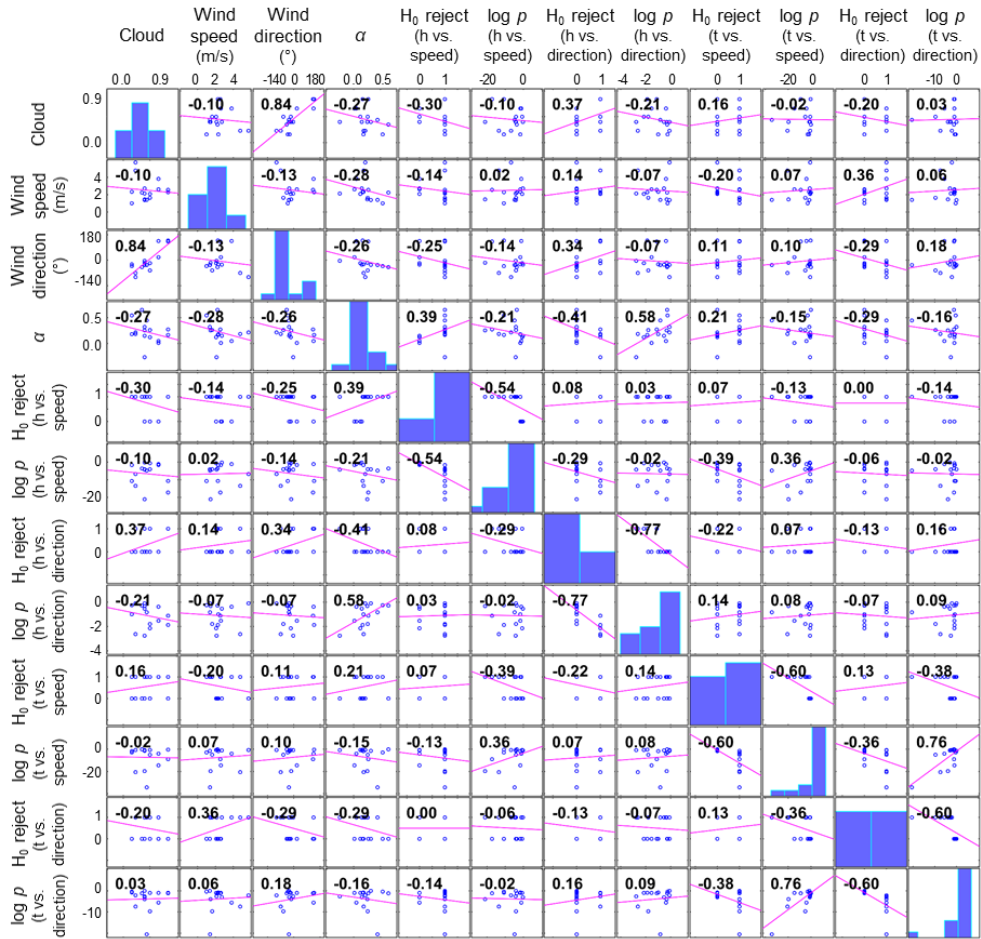


Fig. 4.15. Correlation plots and coefficients between variables from field campaigns.

4.4 Summary

A wind estimation procedure using GPS and IMU data of UAV flights was evaluated in near-field comparative experiments and a series of field campaigns. The near-field experiments showed that the procedure produced wind estimates comparable to the

wind parameters measured by a mechanical anemometer. Field campaigns and following analysis demonstrated advantages and a disadvantage of the method. It was able to offer wind estimates at multiple heights in contrast to a fixed anemometer. Estimated parameters accounting for vertical wind gradient in terms of speed and direction fell in reasonable ranges, and correlations between estimates made sense in view of air dynamics. Also, the observation that the extent of wind gradient varied by cases suggests that direct observations of wind at multiple heights is essential for identifying a vertical wind profile. It is a limitation that the method is vulnerable to time variance, but it can be lessened by taking a minimal time for a single measurement. When wind record, especially including vertical profile, is required but there is no appropriate condition for an anemometer installation, UAV-based wind estimation will be a good alternative. This opinion is reinforced in the current situation where UAVs are widely employed for airborne measurement or remote sensing.

References

- Abbs, D.J., William, L., 1992. Sea-breeze observations and modelling: a review. *sea* 50, 95s.
- Barbieri, L., Kral, S.T., Bailey, S.C., Frazier, A.E., Jacob, J.D., Reuder, J., Brus, D., Chilson, P.B., Crick, C., Detweiler, C., 2019. Intercomparison of small unmanned aircraft system (sUAS) measurements for atmospheric science during the LAPSE-RATE campaign. *Sensors* 19, 2179.
- Chen, W.-F., Lui, E.M., 2005. Handbook of structural engineering. CRC press.

- Donnell, G.W., Feight, J.A., Lannan, N., Jacob, J.D., 2018. Wind characterization using onboard IMU of sUAS. 2018 Atmospheric Flight Mechanics Conference,
- Donnou, H.E., Akpo, A.B., Kouchadé, C.A., Kounouhewa, B.B., Houngue, G.H., Nonfodji, G.F., Djossou, J., 2019. Vertical Profile of Wind Diurnal Cycle in the Surface Boundary Layer over the Coast of Cotonou, Benin, under a Convective Atmosphere. *Advances in Meteorology* 2019.
- Hellmann, G., 1919. Über die Bewegung der Luft in den untersten Schichten der Atmosphäre. *Kgl. Akademie der Wissenschaften [G.] Reimer*.
- Kaltschmitt, M., Streicher, W., Wiese, A., 2007. *Renewable energy: technology, economics and environment*. Springer Science & Business Media.
- Monin, A.S., Obukhov, A.M., 1954. Basic laws of turbulent mixing in the surface layer of the atmosphere. *Contrib. Geophys. Inst. Acad. Sci. USSR* 151, e187.
- Neumann, P.P., Asadi, S., Lilienthal, A.J., Bartholmai, M., Schiller, J.H., 2012. Autonomous gas-sensitive microdrone: Wind vector estimation and gas distribution mapping. *IEEE robotics & automation magazine* 19, 50-61.

This page is intentionally left blank.

Chapter 5. Quantification of methane emission: Field applications and uncertainty analysis

5.1 Introduction

With the development of technology in unmanned aerial vehicles (UAVs), the use of UAVs in gas monitoring has recently been proposed as an up-shooting technology (Kersnovski et al., 2017; Rossi and Brunelli, 2015). Allen et al. reported examples of successful LFG measurement employing UAVs (Allen et al., 2014; Allen et al., 2019; Allen et al., 2016), where they measured carbon dioxide concentrations using a fixed-wing UAV. Then, these concentrations were converted to methane concentrations based on an empirical relationship between the compositions of the two gases. A potential to use the rotary wing UAV in LFG emissions monitoring was tested by Fjelsted et al. (2019) and Shah et al. (2019). Fjelsted et al. (2019) conducted a field study to screen LFG emission hotspot using a thermal infrared camera mounted on a rotary UAV. Shah et al. (2019) showed the applicability of rotary UAV-based platform conveying air samples from 24 ± 3 m above the ground to a gas analyzer on the ground through the 150 m long tubing. The sampling method using tubing connected with a UAV was restricted to a space scale due to the connected tubing length. The limited spatial coverage for a single flight leads to temporal discontinuity between flight missions.

A UAV-mounted detector is able to extend the area of coverage for methane measurements in a single flight; this may enhance the degree of freedom in data acquisition. However, the applicability of direct methane measurement in the air

using a UAV-mounted detector has not been fully assessed despite this potential. Recently, (Shah et al., 2020) tested a prototype analyzer carried by a UAV in exterior experiments with controlled methane emissions. They calibrated the analyzer in the laboratory and reported that the tested instrument yielded successful results in estimating emission. To promote this relatively new method, there is a need for successful showcases. We had multiple field trials in which the rotary UAV-based measurement system and wind estimation method evaluated in Chapters 3 and 4 were deployed around a landfill site to quantify the methane emission rates. Uncertainty analysis was accompanied to assess the accuracy inherent to this methodology, and the results will demonstrate the advantages and challenges of applying the methodology.

5.2 Materials and methods

5.2.1 Apparatus

5.2.1.1 Methane measurement system

Methane concentration was measured using a semiconductor-type real-time gas detector (Testo Gas Detector, Testo SE & Co. KGaA, Germany), and the Matrice 600 Pro (SZ DJI Technology Co., Ltd, People's Republic of China) was used for airborne methane monitoring. The specifications of the detector and UAV are summarized in Table 3.1. During flight missions, the detector was attached to the UAV, and detector readings were recorded by an installed camera. Readings from flights were corrected to account for response time.

The detector was placed at the center, 340 mm below the aircraft. There are a

couple of options for the detector placement to minimize the effects of rotor turbulence. To place a detector or an air inlet outside the range of the rotor turbulence could be ideal options, but those options require compromises in terms of flight instability or response time. Another option is the center above or below the aircraft. Guo et al. (2020) showed through CFD analysis and experimental verification that air turbulence is insignificant at the centerline just above and below an aircraft in hover.

5.2.1.2 Weather data acquisition

Weather data were obtained from the opened database of the Korea Meteorological Administration for the early field campaigns. For the rest campaigns, a weather station (Vantage Pro2, Davis, USA) was temporarily installed within the site. Wind speeds and directions were estimated using GPS and IMU data of UAV flight logs. The estimation method takes advantage of the difference between the velocity expected from aircraft thrust and the actual velocity at a moment. The details were discussed in Chapter 4.

5.2.2 Field campaigns

5.2.2.1 Site description

Field campaigns were conducted around the Dangjin-si Resource Circulation Center, Dangjin, Republic of Korea. It has multiple potential methane sources in and around it: the first landfill cell (Fig. 5.1a), landfill leachate reservoirs (Fig. 5.1b), the second landfill cell which is roof-covered (Fig. 5.1c), a food waste treatment facility (Fig. 5.1d), and a manure treatment facility (Fig. 5.1e) inside the center, and paddy fields around it. Among them, the first landfill cell and the leachate reservoirs were the

methane sources to quantify the emissions. The second landfill cell was not considered, because it has not been received wastes for landfilling. The food waste facility and the manure facility were also excluded. It is expected that emissions from adjacent paddy fields are insignificant relative to those from the landfill, considering their emission rates of 2-6 kg/ha/day estimated using the IPCC guideline and country-specific factors of Korea. The overall topography is a flatland adjacent to the sea in the Northwest. The first landfill cell is a four-hectare managed landfill with passive vents and leachate collection system. It had received municipal solid waste from 2000 to 2014, and afterwards, it has been used for disposal of minimal amounts of some incombustible waste.



Fig. 5.1. Satellite image of the site. A first landfill cell (a) and leachate reservoirs (b)

were the methane source of interest. Another landfill cell (c), food waste treatment facility (d), and manure treatment facility (e) were excluded.

5.2.2.2 Measurement missions

We conducted 13 field campaigns at the site: once each in April and August, 2019; five times in February, 2020; and three times each in May and October, 2020. Methane concentrations were collected throughout virtual, vertical measurement planes at the upstream and downstream of the target sources. Configurations of the planes, measuring platforms, height spacings, and other practical details were adjusted at the site depending on wind direction, physical obstacles, and UAV battery time. When possible, the measurement planes were placed normal to the wind direction, and methane was measured at heights from 5 to 100 m with UAV systems, and on ground with the same detector on a vehicle. The UAV was driven faster than 10 m/s to avoid influences of rotor downwash according to the recommendation in Chapter 3. Height spacings were 5 m at low heights and increased up to 20 m near the upper boundary. The intention of such arrangements was not to lose plumes that were expected to pass lower heights rather than elevated heights.

5.2.3 Computational methods

5.2.3.1 Methane emission

Methane emission rates were computed on the basis of the mass balance.

$$\text{Emission} = \text{Outflow} - \text{Inflow} \quad (5.1)$$

$$\text{Out/inflow} = \int_0^H \int_{x_1}^{x_2} u(h) C(x, h) dx dh \quad (5.2)$$

$$\text{Out/inflow} \approx \sum_{i=1}^n u_i C_i \Delta x \Delta h \quad (5.3)$$

where h is the height above ground (L), H is h at the upper boundary of a measurement plane (L), x is the distance in the direction perpendicular to the wind direction (L), x_1 and x_2 are x at the both boundaries (L), $u(h)$ is the wind speed at the height h (LT^{-1}), $C(x, h)$ is the methane concentration enhancement at the distance x and the height h , n is the number of area elements with the width Δx and the height Δh in a measurement plane, and u_i and C_i are the wind speed and the methane concentration enhancement in the i^{th} element, respectively. The unit of computed emission and out/inflow is L^3T^{-1} or MT^{-1} depending on the unit of $C(x, h)$ and C_i (unitless or ML^{-3}).

5.2.3.2 Uncertainty analysis

An error propagation model was used to compute uncertainties in estimated methane emissions. For the i th area element with the lateral length Δx and the vertical length Δh , the uncertainty σ_i was defined as follows:

$$\sigma_i = (\sigma_{u,i}^2 C_i^2 + u_i^2 \sigma_{C,i}^2)^{1/2} \Delta x \Delta h \quad (5.4)$$

$$\sigma_i = (\sigma_{u1,i}^2 C_i^2 \Delta x_1^2 + \sigma_{u2,i}^2 C_i^2 \Delta x_2^2)^{1/2} \Delta h + (u_i^2 \sigma_{C1,i}^2 + u_i^2 \sigma_{C2,i}^2)^{1/2} \Delta x \Delta h \quad (5.5)$$

where $\sigma_{u,i}$ and $\sigma_{C,i}$ are wind variation and error in methane enhancement, respectively, $\sigma_{u1,i}$ and $\sigma_{u2,i}$ are wind variations in south-north direction and east-west direction, respectively, Δx_1 and Δx_2 are the lengths projected from Δx to east-west and south-north planes, respectively, and σ_{C1} and σ_{C2} are errors in methane detection and interpolation of measured concentrations, respectively. As the amount of total methane flow through a vertical measurement plane equals to the sum of all elements,

the total uncertainty σ is expressed as follows:

$$\sigma = (\sum_{i=1}^n \sigma_i)^{1/2} \quad (5.6)$$

5.3 Results and discussion

5.3.1 Methane captured on the measurement planes

Of 13 field campaigns at the Dangjin-si Resource Circulation Center, nine campaigns were analyzed to compute methane emissions and uncertainties. In the rest four cases, it turned out that the measurement configurations were not properly selected, given the wind direction, and the measurement planes seem unlikely to have included the plume to measure. It can occur when wind direction alters with time, or when wind is so weak that it is difficult to find average wind direction. Statistical tests evidence that there were significant variations in wind direction during measurements in four of the five exclusions (ANOVA, $p < 0.05$).

Fig. 5.4 shows the measurement configuration, wind direction, and methane flux computed on the downstream plane from the eight field campaigns. As the site is adjacent to the sea on its northwest side, northwest wind was dominant at most days. Methane flux through the measurement planes was computed and analyzed first, and Fig. 5.2 shows the flux on the downstream planes. Methane plumes were generally detected near ground ($h < 20$ m). Only in the case of 2020 0512am, there was a plume at approximately 50 m height (Fig. 5.2(e)), which was attributed to a plume rise with moving distance from the suspected emitter. Although it is theoretically expected considering the emission rate and gas temperature (Briggs, 1984; Turner, 1994) that the plume rise would not exceed 1 m above the passive

vents in landfills, our results evidenced that the plume ascended with the moving distance. Looking at patterns in multiple campaigns, it is likely that the plumes detected at higher heights would originate from exterior sources.

There was detectable methane also on the upstream measurement planes, usually near ground (data not shown). However, analogous plumes were never found on the downstream planes, therefore, the methane flux on the upstream planes was not considered in computing emissions, as described in [Equation 5.1](#). It may be a possible explanation that the plumes captured at upstream ascended over the upper boundary of the downstream planes, or dispersed when they reached to the downstream planes so that the resulting enhancement was not detectable by the given instruments. This does not suggest that it is not necessary to conduct missions at upstream. Fig. 5.3 shows an example of preliminary measurements in which a large plume in the middle appeared both at the upstream and downstream. The plume would have been lifted by over 20 m so that the downstream measurement could capture no more than half of it. A comparison of flux computed for the plume showed that 44 % of the plume were captured by the downstream plane. In such a case, it is crucial to subtract the inflow from the outflow, otherwise, exterior methane flux would account for a significant portion of the computed emission estimate, resulting in overestimation.

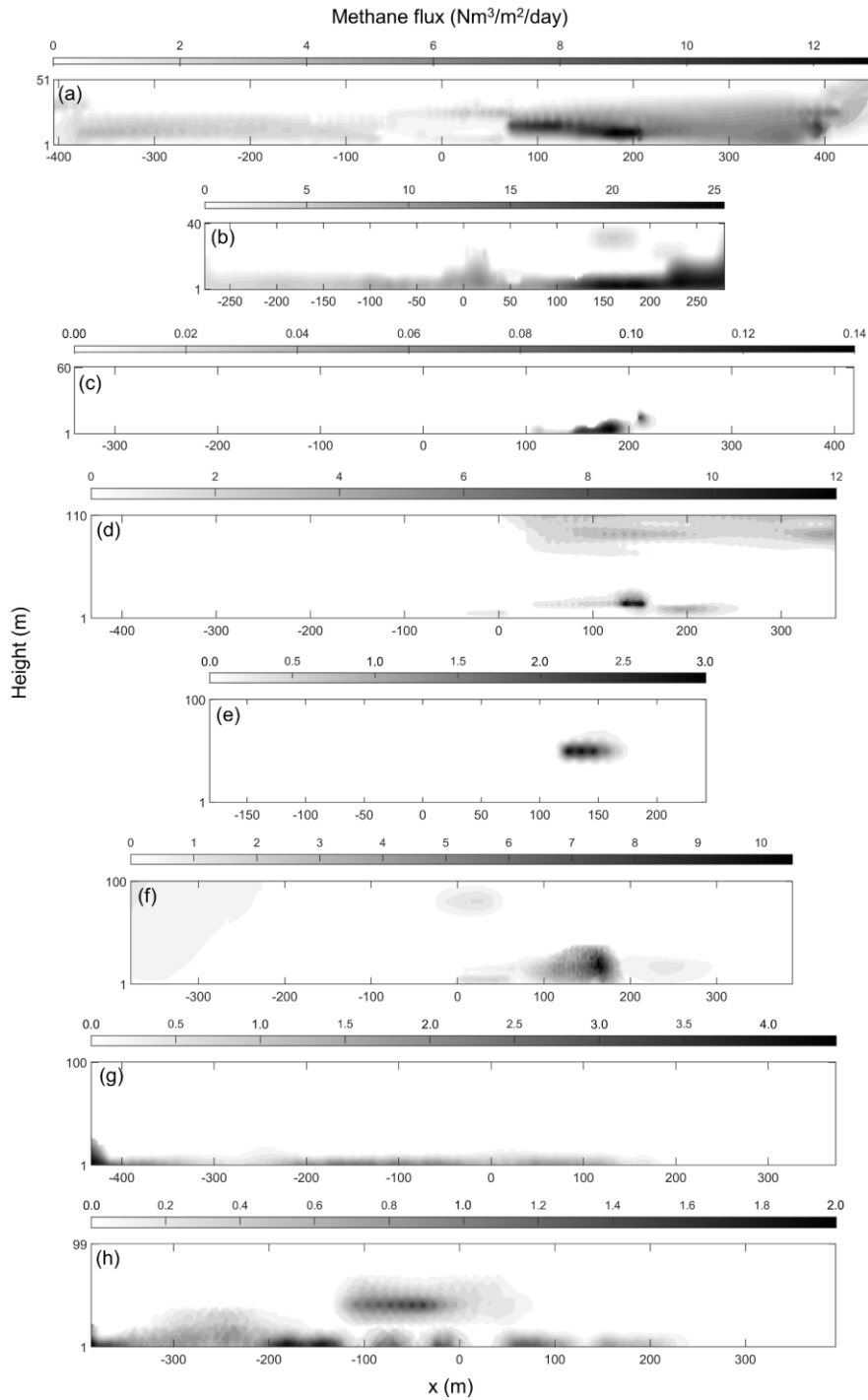


Fig. 5.2. Methane flux at downstream measurement plane at (a) 2019 0416 pm; (b) 2019 0830 am; (c) 2020 0218 pm; (d) 2020 0220 pm; (e) 2020 0512 am; (f) 2020 1020 pm; (g) 2020 1021 am; and (h) 2020 1021 pm.

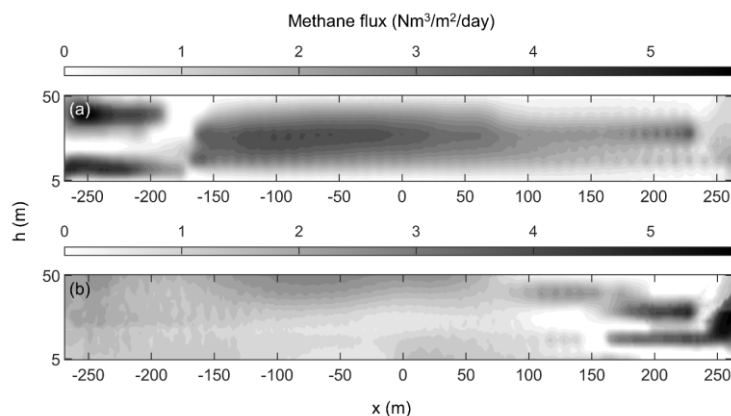


Fig. 5.3. Methane flux from preliminary flights where a single plume appeared at both the upstream (a) and downstream (b) measurement planes.

Overlaying a graph of height-integrated methane flux on the map with the wind direction marked helped to guess where detected methane plumes would have flowed out from (Fig. 5.4). It appears that the food waste treatment facility often emitted considerable amounts of methane. Because the emitter is located right next to the landfill (the distance between borders ~ 20 m), it was difficult to decompose the plumes from the two sources. Still, it was possible, which would not have been possible with advanced but heavy (> 10 kg) gas analyzer. The ability to approximate the source of each distinct plume partly justifies our choice to have compromised the accuracy of the gas detector to obtain two-dimensional flux mapping through a virtual vertical plane.

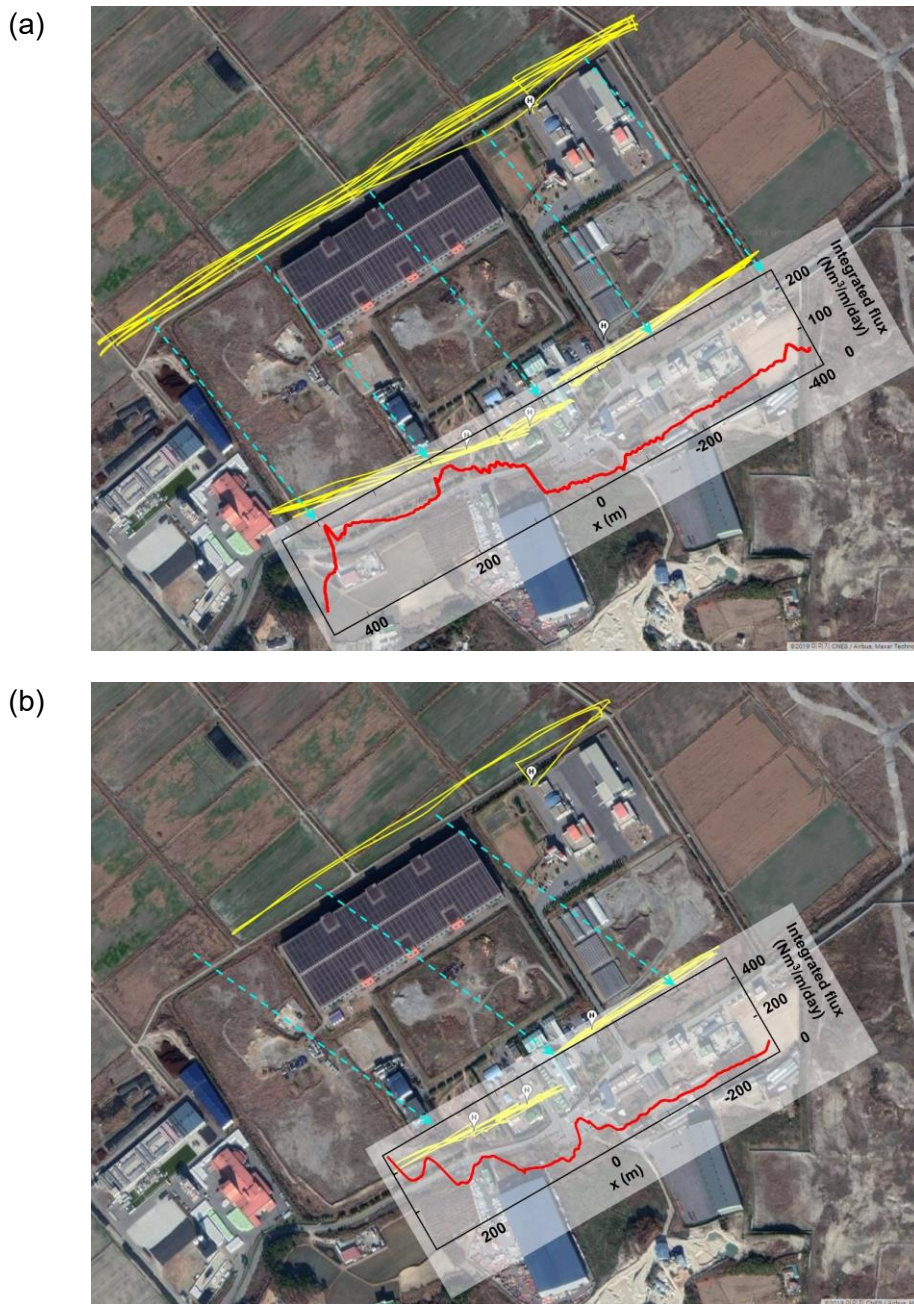


Fig. 5.4. Flight trajectory (yellow lines), wind direction (cyan broken lines), and integrated methane flux on the downstream measurement plane at (a) 2019 0416 pm; (b) 2019 0830 am; (c) 2020 0218 pm; (d) 2020 0220 pm; (e) 2020 0512 am; (f) 2020 0512 pm; (g) 2020 1020 pm; (h) 2020 1021 am; and (i) 2020 1021 pm.

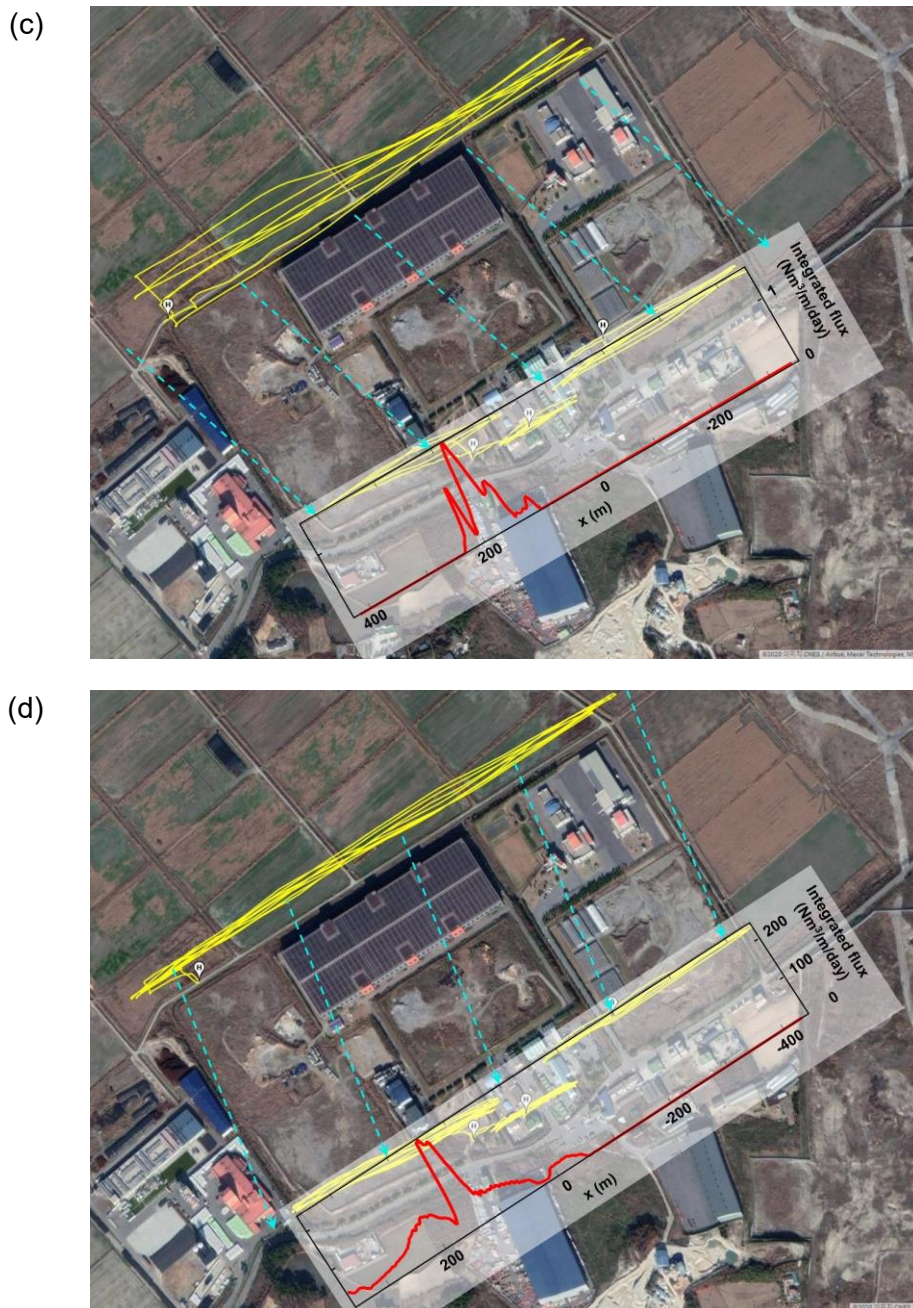


Fig. 5.4. Flight trajectory (yellow lines), wind direction (cyan broken lines), and integrated methane flux on the downstream measurement plane at (a) 2019 0416 pm; (b) 2019 0830 am; (c) 2020 0218 pm; (d) 2020 0220 pm; (e) 2020 0512 am; (f) 2020 0512 pm; (g) 2020 1020 pm; (h) 2020 1021 am; and (i) 2020 1021 pm. (continued)

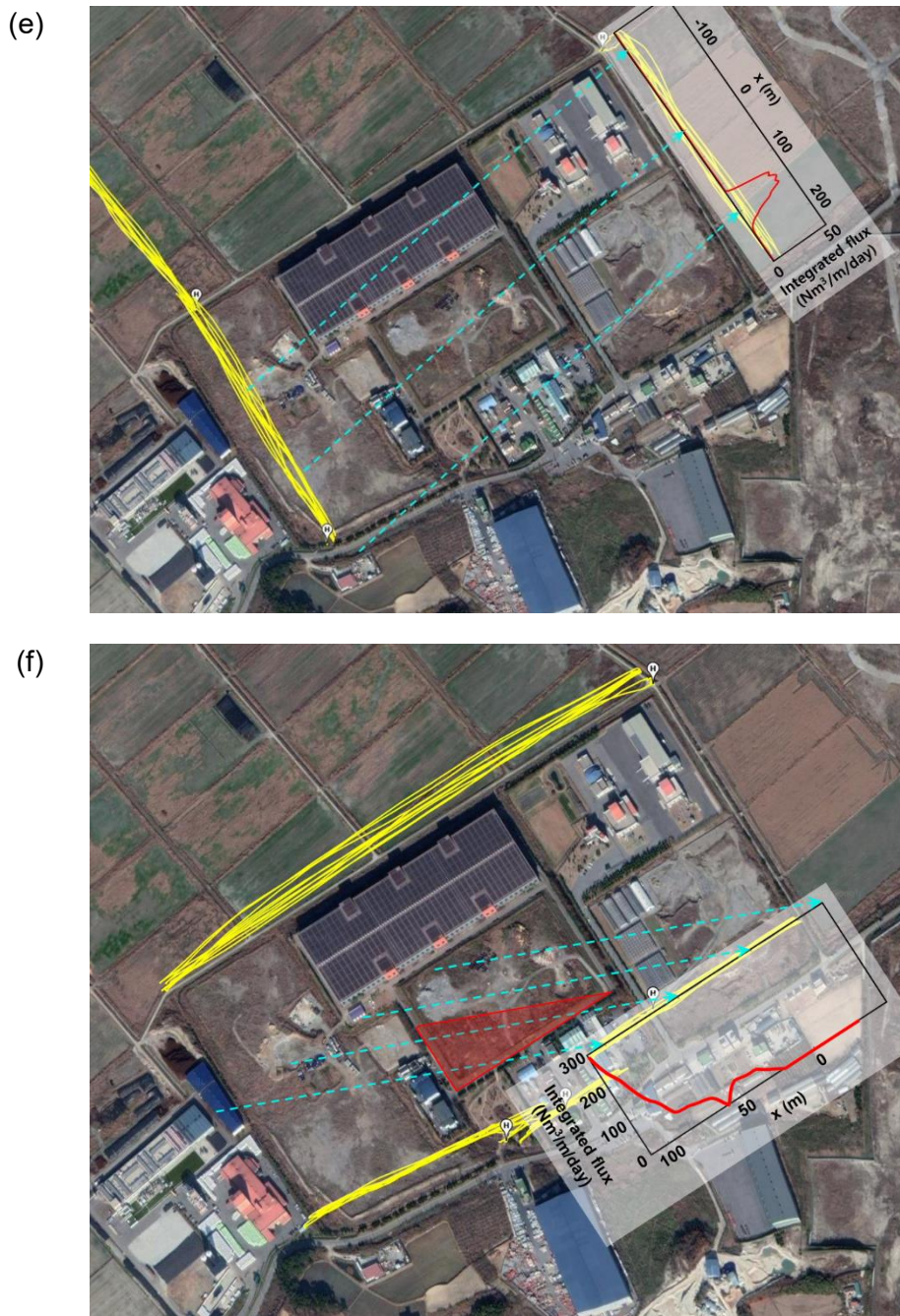


Fig. 5.4. Flight trajectory (yellow lines), wind direction (cyan broken lines), and integrated methane flux on the downstream measurement plane at (a) 2019 0416 pm; (b) 2019 0830 am; (c) 2020 0218 pm; (d) 2020 0220 pm; (e) 2020 0512 am; (f) 2020 0512 pm; (g) 2020 1020 pm; (h) 2020 1021 am; and (i) 2020 1021 pm. (continued)



Fig. 5.4. Flight trajectory (yellow lines), wind direction (cyan broken lines), and integrated methane flux on the downstream measurement plane at (a) 2019 0416 pm; (b) 2019 0830 am; (c) 2020 0218 pm; (d) 2020 0220 pm; (e) 2020 0512 am; (f) 2020 0512 pm; (g) 2020 1020 pm; (h) 2020 1021 am; and (i) 2020 1021 pm. (continued)



Fig. 5.4. Flight trajectory (yellow lines), wind direction (cyan broken lines), and integrated methane flux on the downstream measurement plane at (a) 2019 0416 pm; (b) 2019 0830 am; (c) 2020 0218 pm; (d) 2020 0220 pm; (e) 2020 0512 am; (f) 2020 0512 pm; (g) 2020 1020 pm; (h) 2020 1021 am; and (i) 2020 1021 pm. (continued)

5.3.2 Methane emission rates

In spite of difficulties in decomposing plumes, the methane emission rates from the landfill cell were determined by integrating methane flux in the carefully selected ranges of x and h . As presented in Table 5.2, the estimated methane emissions range in 406.4–3,640 kg/ha/day, except for the case of 2020 0218pm. The exception will be discussed further in the following section, not in this section. It should be noted that in the case of 2020 0512 pm, only a third of area was included by the downstream measurement plane (Fig. 5.4f). With a correction factor explaining the ratio of

covered area, the estimated emission rate fell in the range of the rest estimates. However, such correction is not recommended, because it assumes homogeneous emission—which is hardly true for landfills.

Modeling with the first order decay model in IPCC guidelines (IPCC, 2006, 2019) gave the estimated methane emission of 1,515 and 1,442 kg/ha/day for the year 2019 and 2020, respectively. The amounts of waste disposed in the landfill were mostly obtained from the Statistics Korea. IPCC default values of model parameters were mostly adopted while two parameters were chosen considering the condition of the landfill: $k = 0.05$ (country-specific) (Korea Ministry of Environment, 2014); $F = 0.5$; $MCF = 0.5$ (IPCC value for managed well, semi-aerobic site); $DOC = 0.09$; $DOC_F = 0.5$; $OX = 0.1$. Another estimate is 845 kg/ha/day, which is based on monitoring data reported in Sudokwon Landfill Site Management Corporation (2019). It should be noted that this estimate was obtained by averaging all methane flows through surface emission, passive vents, and gas recovery system. It seems reasonable to include gas flows through passive vents and gas recovery system to compare to the estimates in this study, because our method would measure all fugitive methane regardless of the pathway, and the landfill in the Dangjin-si Resource Circulation Center does not have gas recovery system.

The methane emission rates computed in this study vary within but an order of magnitude, and are comparable to the emission rates acquired from other methods. Except for 2020 0218pm, our estimates equal to 0.3–2.4 times of the value from the IPCC modeling, and 0.5–4.3 times of the average of the Sudokwon Landfill. Considering that the extensive temporal variability of fugitive emission from landfills—up to two orders of magnitude difference—is very common (Gonzalez-

Valencia et al., 2021; Zhang et al., 2013), and that the IPCC model is used to compute year-round emission, not the value at a certain point of time, the difference between our estimates, and that between our estimates and estimates by other methods is highly likely to originate from the actual variation with time. In other words, our results provided another piece of evidence for temporal variability of methane emissions from landfills, which again emphasizes the importance of frequent field measurements to get closer to the true values.

Methane concentrations at the plume center were calculated by means of the Gaussian dispersion model with parameters chosen based on the estimated emission rates and record on the meteorological conditions. As a result, Fig. 5.5 shows that the differences between measured and Gaussian-simulated concentrations at the plume center did not exceed twice. Exact comparisons may be inappropriate, because gas transport from an area source or a combination of several hotspots cannot be approximated to that from a point source that the dispersion model used here assumes. The difference between a point and non-point sources explains the results that the measured concentrations were lower than the modeled concentrations in most cases, and that there was a relatively small plume observed at downstream planes—which could be attributed to a single hotspot—in the two cases with the smallest difference between measured and modeled values. It is believed that a little weak but clear agreement in this comparison supports the validity of the measurement method.

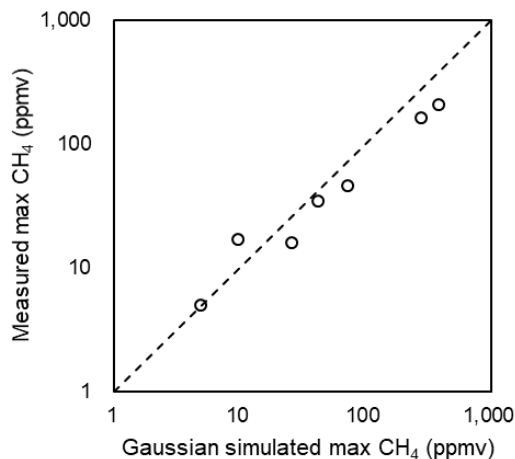


Fig. 5.5. Maximum CH₄ concentrations at downstream measurement planes: measured at site and simulated by the Gaussian dispersion model.

5.3.3 Uncertainties in emission estimates

Uncertainty was calculated for each value of emission estimate. Standard errors from calibration curves of methane detector were used as $\sigma_{C1,i}$, thereby, computed uncertainties can account for errors produced by the randomness in instrumental response, and the limited resolution. For $\sigma_{C2,i}$, standard errors from krigging were adopted to count uncertainties created by spatial interpolation. Wind variations are also a critical uncertainty. Wind variations include time- and height-dependency, which the use of standard error from vertical wind profile could encompass. Dealing separately with northward and eastward components of wind vectors allowed of explaining changes in both speed and direction.

Computed uncertainties were 3.5–17.3 % of estimated methane emissions, still with an exception of 2020 2018pm (Table 5.2). There was not a common

predominant factor of uncertainty. Even though interpolation was the most powerful contributor in most cases (1.8–9.5 %), wind and detection uncertainties were dominant factors for 2019 0416 pm and 2020 0512 am, respectively. Such a difference may be brought about by weather and gas transport varying every event. The case of 2019 0416 pm had the largest wind variation among all the cases in uncertainty analysis, providing an explanation for the large uncertainty related to wind. In the case of 2020 0512 am, methane enhancements were very low (< 5 ppmv) throughout the downstream measurement plane due to high wind speed. With low concentrations, errors in methane detection is bound to be high relative to the concentration range.

Large detection uncertainty of 2020 0512 am arising from strong wind is the opposite case, demonstrating that there would be an upper limit of wind speeds as well as the lower limit. An upper limit of wind speeds in this respect would be determined by methane emission rate from the source, the extent of gas mixing in the atmosphere, and the detection limit of gas analyzer. Applying the Gaussian dispersion model for our cases, the downstream measurement plane has to be located no further than 200 m downwind with 5 m/s wind in unstable atmosphere. Also, there is the maximum wind speed to secure UAV operation, and therefore, the lower value of two maximum speeds will be the practical upper limit of wind speeds.

Table 5.1. Maximum downwind distance of a measurement plane from the source, which was simulated by the Gaussian dispersion model supposed 3,600 kg/day emission rate and the given measurement unit.

| Wind speed (m/s) | Pasquill stability | | | |
|---------------------|--------------------|-----|-------|-------|
| | A | B | C | D |
| 1.5 | 250 | 370 | - | - |
| 2.0 | 220 | 320 | > 500 | - |
| 3.0 | 180 | 260 | 410 | > 500 |
| 4.0 | - | 220 | 350 | > 500 |
| 5.0 | - | 200 | 310 | > 500 |

Large uncertainty by overall low methane also explains the results of 2020 0218pm. Here, the uncertainty exceeded the estimated emission rate, which, in fact, means that our methodology could not detect the emission. It was speculated, at first, that wind was too weak to bring sufficient amounts of methane to the downstream plane, because there was the weakest wind among all the series of field campaigns. This is an example that showed the most critical limitation of downwind plume methods. Downwind plume methods are valid only when advective gas transport overwhelms diffusive transport, in other words, they require wind stronger than a certain speed. Bourn et al. (2017) recommended wind speeds greater than around 2 m/s as a consideration for the UAV mass balance method.

Mathematical simulations with different wind speeds implied that there would be the lower limit of wind speed. A term explaining longitudinal dispersion—parallel to the wind direction—was added to the typical three-dimensional advection-dispersion model, and dispersion coefficients were selected based on the coefficients of the successful campaigns. Looking at the shape of plumes in Fig. 5.6, it is evident

that it is hard to neglect the longitudinal dispersion with the wind of 1 m/s. Especially, near-field measurements are sensitive to the longitudinal dispersion, which is the case of our measurement condition as well as the simulation. Although most dispersion models neglect the longitudinal dispersion, there has been assertion forward its importance (Arya, 1995).

Nevertheless, the failure and large uncertainty could not be attributed to weak wind, because the simulation showed that, even with such weak wind, methane should have been detected in dozens of ppmv at downstream (Fig. 5.6). Instead, it was found that there was a considerably large area without samplings at the downstream plane. As the area was direct downwind of the emitter of interest, and at low heights that was highly likely to include the plume, it seems that we missed the plume between the sampling grid. Experiencing this case left another practical message: Similar circumstances may occur depending on physical obstacles, piloting proficiency, wind direction, arrangement of measurement planes, etc., thus, results should be scrutinized step by step, out of the routine data processing, to ensure proper quantification of emissions.

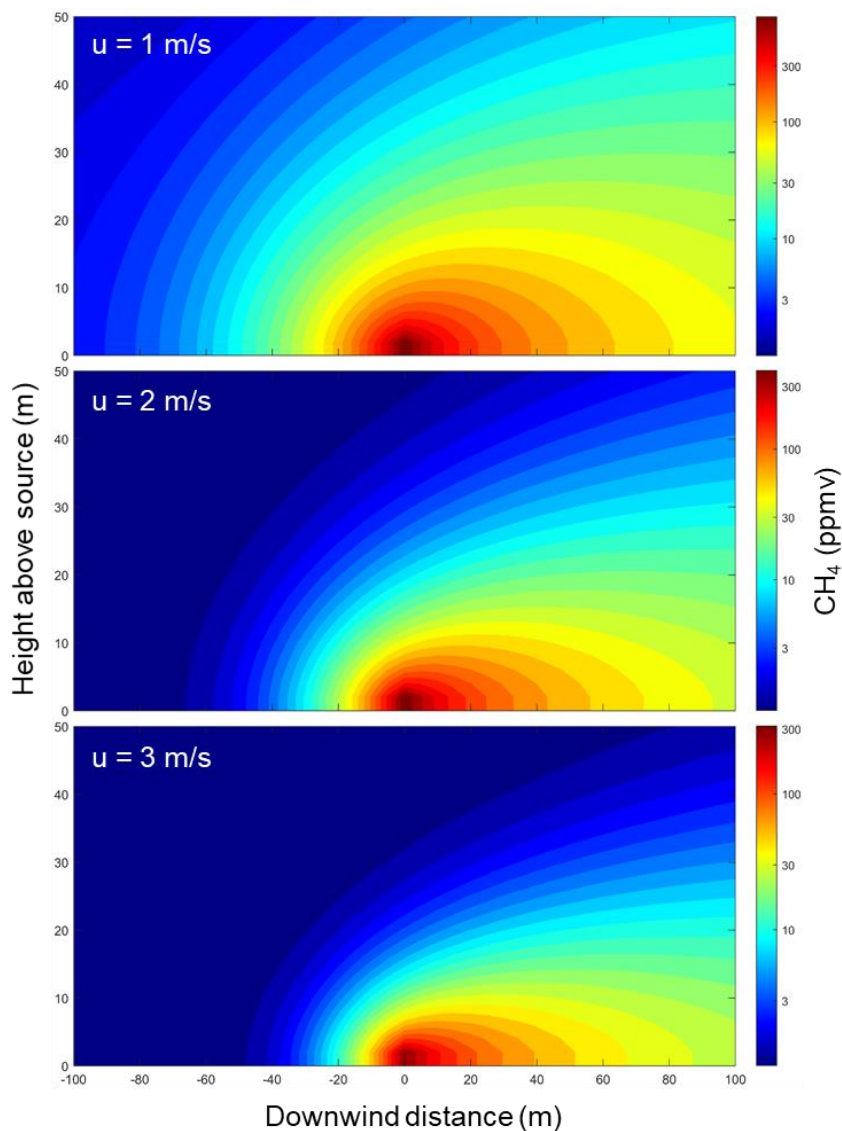


Fig. 5.6. Methane concentrations at steady state simulated by advection-dispersion model with different wind speeds.

This study could not completely consider the following potential error-inducing factors in the computation of uncertainties: detector response rate, GPS positioning, and peaks deconvolution. The methane detector used in this study presented quick

responses with a gradual change in methane concentrations, and the response time was corrected as mentioned in Section 5.2.1.1. However, it was observed that the responses were delayed to a greater extent when it encountered rapid changes. Response time depending on the rate of change needs to be quantified and corrected, which could not be achieved in this study. GPS positioning can involve a systematic error of GPS sensors, and errors occurring in the process of synchronizing positioning data and methane records. Those errors associate with detector response rate and GPS positioning are expected to have little impact on the overall uncertainty. That is because they would be largely compensated or eclipsed by means of denser measurement grids and appropriate spatial interpolation, and will definitely be lessened with the application of improved sensors in the future. It is peaks deconvolution that is thought would significantly add uncertainty. As the study site has multiple methane sources besides a landfill, we tried decomposing plumes manually based on suspected sources. It could not be suggested for now how much difference other options for peaks deconvolution would make in the estimated methane emissions.

Table 5.2. Weather data and estimated methane emissions from successful field campaigns.

| | Weather | | | | | Emission rate (kg/ha/day) | Uncertainty in emission rate (%) | | | |
|--------------|---------|---------|-------|----------------------|-------------------|------------------------------|----------------------------------|-----------|---------------|-------|
| | T (°C) | P (hPa) | Cloud | Wind speed* (m/s) | Wind direction | | Total | Detection | Interpolation | Wind |
| 2019 0416 pm | 20.0 | 1,015.1 | 0.44 | 1.40 | NW | 3,560 | 3.51 | 0.76 | 1.81 | 2.91 |
| 2019 0830 am | 24.6 | 1,009.6 | 0.35 | 2.24 | NW | 3,640 | 3.85 | 0.89 | 2.91 | 2.35 |
| 2020 0218 pm | 1.4 | 1,028.0 | 0.16 | 1.00 | NW | 1.4 | 850 | 847 | 60.57 | 32.36 |
| 2020 0220 pm | 9.8 | 1,033.2 | 0.40 | 1.46 | NNW | 457.0 | 10.38 | 2.90 | 9.54 | 2.89 |
| 2020 0512 am | 16.9 | 1,004.1 | 0.23 | 5.73 | SW | 406.4 | 17.27 | 16.76 | 4.10 | 0.75 |
| 2020 0512 pm | 17.6 | 1,004.8 | 0.23 | 4.80 | W | 1,685.2 | 22.73 | 13.23 | 13.24 | 12.90 |
| 2020 1020 pm | 18.4 | 1,026.0 | 0.40 | 1.38 | NW | 905.5 | 4.74 | 1.81 | 4.19 | 1.28 |
| 2020 1021 am | 15.5 | 1,021.1 | 0.84 | 2.28 | SSE | 705.3 | 5.64 | 3.32 | 4.36 | 1.30 |
| 2020 1021 pm | 17.1 | 1,017.3 | 0.84 | 2.56 | SSE | 934.8 | 5.74 | 3.00 | 4.83 | 0.78 |

* At 10 m height.

5.4 Summary

We tried 13 field campaigns to collect actual data of wind and methane concentration around a waste landfill. Except for five cases in which vertical measurement planes were placed in the wrong way relative to the average wind direction, data from eight campaigns were analyzed to estimate methane emission rates based on downwind plume method and mass balance. The estimates fall in a reasonable range compared to the estimate by the IPCC guidelines and the reported emissions of a larger well-managed landfill in Korea. Only a campaign failed to provide a reliable estimate, which was attributed to weak wind. Uncertainty analysis was accompanied to quantify uncertainties caused by detection errors, interpolation errors, and wind variations. The total uncertainties were below 6 % for five cases, and below 18 % for two cases. It is expected that introduction of improved gas analyzer will be able to greatly lessen the uncertainties of this methodology in the near future. Plumes deconvolution that could not be reflected in the uncertainty analysis in this study is an important challenge for follow-up studies.

References

- Allen, G., Hollingsworth, P., Illingworth, S., Kabbabe, K., Perciva, C., 2014. Feasibility of aerial measurements of methane emissions from landfills. Environmental Agency: Rotherham, UK.
- Allen, G., Hollingsworth, P., Kabbabe, K., Pitt, J.R., Mead, M.I., Illingworth, S., Roberts, G., Bourn, M., Shallcross, D.E., Percival, C.J., 2019. The development and trial of an unmanned aerial system for the measurement of methane flux

- from landfill and greenhouse gas emission hotspots. *Waste Management* 87, 883-892.
- Allen, M., Hollingsworth, P., Mead, I., Kabbabe, K., Roberts, G., Percival, C., 2016. Measuring landfill methane emissions using unmanned aerial systems: field trial and operational guidance. Environment Agency: Horizon House, Deanery Road, Bristol, BS1 5AH.
- Bourn, M., Allen, G., Hollingsworth, P., Kababbe, K., Williams, P.I., Ricketts, H., Pitt, J.R., Shah, A., 2017. The development of an unmanned aerial system for the measurement of methane emissions from landfill. Sardinia 2017, Sixteenth International Waste Management and Landfill Symposium, Italy, 2-6 October 2017.
- Briggs, G.A., 1984. Plume rise and buoyancy effects. *Atmospheric science and power production*, 327-366.
- Fjelsted, L., Christensen, A., Larsen, J., Kjeldsen, P., Scheutz, C., 2019. Assessment of a landfill methane emission screening method using an unmanned aerial vehicle mounted thermal infrared camera—A field study. *Waste Management* 87, 893-904.
- IPCC, 2006. 2006 IPCC guidelines for national greenhouse gas inventories. IGES, Japan.
- IPCC, 2019. Refinement to the 2006 IPCC guidelines for national greenhouse gas inventories. IPCC, Switzerland.

Kersnovski, T., Gonzalez, F., Morton, K., 2017. A UAV system for autonomous target detection and gas sensing. 2017 IEEE aerospace conference, MT, USA, March 4-11, 2017.

Rossi, M., Brunelli, D., 2015. Autonomous gas detection and mapping with unmanned aerial vehicles. IEEE Trans. Instrum. Meas. 65, 765-775.

Shah, A., Allen, G., Pitt, J.R., Ricketts, H., Williams, P.I., Helmore, J., Finlayson, A., Robinson, R., Kabbabe, K., Hollingsworth, P., 2019. A near-field gaussian plume inversion flux quantification method, applied to unmanned aerial vehicle sampling. Atmosphere 10, 396.

Shah, A., Pitt, J.R., Ricketts, H., Leen, J.B., Williams, P.I., Kabbabe, K., Gallagher, M.W., Allen, G., 2020. Testing the near-field Gaussian plume inversion flux quantification technique using unmanned aerial vehicle sampling. Atmospheric Measurement Techniques 13.

Statistics Korea, Waste collection,
http://stat.kosis.kr/statHtml_host/statHtml.do?orgId=705&tblId=DT_02012S_206&conn_path=I3 (Access date: 11.03, 2020)

Sudokwon Landfill Site Management Corporation, 2019. Year 2018 Sudokwon Landfill statistics yearbook. Sudokwon Landfill Site Management Corporation, Incheon, Korea.

Turner, D.B., 1994. Workbook of atmospheric dispersion estimates: an introduction to dispersion modeling. CRC press.

This page is intentionally left blank.

Chapter 6. Conclusions

As an efficient and reliable method is required to quantify methane emissions from waste landfills, this work proposed and assessed the methodology using UAV-based plume measurement and mass balance.

A measurement system was composed of a lightweight methane detector and a rotary UAV, and the validity of the system was tested experimentally and theoretically. In the detector reliability test, the methane detector showed sufficient resolution for field application, and the detection error was evaluated to compute the uncertainty in emission estimates propagated from detection error. While a theoretical examination told that the impact of air flow on the detection is negligible, the stability against vibration during flight, and response rate of the detector are the potential error-inducing factors that this work has not completely tackled. However, their entailing uncertainty is to be lessen with the rapid development of light, high performance sensors in the near future.

Positioning accuracy of the UAV is thought to be a comparatively minor contributor to uncertainty, because the UAV uses three sensors simultaneously, and the great number of sampling points helps reduce the uncertainty. The turbulence induced by the rotors has an insignificant influence on overall concentration fields due to its small scale in terms of time and space. Instead, the turbulence can make a noticeable change in concentration fields close to the airframe. In this regard, the critical UAV velocity and the detector placement were determined to ensure the credibility of the proposed measurement system.

When spatial interpolators were applied to field data from the measurement system, the empirical Bayesian kriging demonstrated the best prediction of methane concentrations at unmeasured points. A tight grid design was applied to reduce uncertainty, but the error resulting from the inevitable discontinuity was included in the interpolation uncertainty.

A wind estimation procedure using GPS and IMU data of UAV flights was evaluated in near-field comparative experiments and a series of field campaigns. The near-field experiments showed that the procedure produced wind estimates comparable to the wind parameters measured by a mechanical anemometer. Field campaigns and following analysis demonstrated advantages and a disadvantage of the method. It was able to offer wind estimates at multiple heights in contrast to a fixed anemometer. Estimated parameters accounting for vertical wind gradient in terms of speed and direction fell in reasonable ranges, and correlations between estimates made sense in view of air dynamics. Also, the observation that the extent of wind gradient varied by cases suggests that direct observations of wind at multiple heights is essential for identifying a vertical wind profile. It is a limitation that the method is vulnerable to time variance, but it can be lessened by taking a minimal time for a single measurement. The UAV-based wind estimation can be a good option in our application that employs a UAV for airborne measurements and requires vertical wind profiles. Furthermore, by fully tracking the wind variability with both time and height with the wind estimator, we were able to quantify the resulting wind uncertainty.

We tried 13 field campaigns to collect actual data of wind and methane concentration around a waste landfill. Except for four cases in which vertical

measurement planes were placed in the wrong way relative to the average wind direction, data from nine campaigns were analyzed to estimate methane emission rates based on downwind plume method and mass balance. The estimates fall in a reasonable range compared to the estimate by the IPCC guidelines and the reported emissions of a larger well-managed landfill in Korea. Only a campaign failed to provide a reliable estimate, which was attributed to weak wind. Uncertainty analysis was accompanied to quantify uncertainties caused by detection errors, interpolation errors, and wind variations. The total uncertainties were below 6 % for five cases, and below 23 % for three cases. It is expected that introduction of improved gas analyzer will be able to greatly lessen the uncertainties of this methodology in the near future. Plumes deconvolution, which could not be reflected in the uncertainty analysis in this study, is an important challenge for follow-up studies.

The strategies for properly applying the proposed methodology were summarized as follows:

- 1) The wind speed must be above the lower limit to satisfy the assumption that the advection is predominant. The limit could not be specified in this study, but is estimated to be between 1.0-1.4 m/s.
- 2) The downstream measurement plane should be carefully determined considering the wind direction as well as the maximum distance determined by mathematical simulation.
- 3) The airspeed should exceed 10 m/s, which is specific for the equipment used here.

- 4) It is necessary to consider the vertical wind gradient.
- 5) The existence of other methane sources nearby requires source apportionments of the measured plumes.
- 6) Denser samplings at lower altitudes are preferable not to miss the plumes of interest.
- 7) It is a good option to operate multiple UAVs simultaneously.

The first five strategies are the essential cautions, while the rest two messages are recommendations to further reduce uncertainty.

국문 초록

폐기물 매립지에서 탈루 메탄 배출량을 산정하기 위해 사용되는 여러 방법들 중, 최근 무인항공기(unmanned aerial vehicle, UAV)를 활용하는 방법이 제안되었다. 회전익 UAV가 조종이 쉽고 고해상도 측정이 가능하다는 장점이 있어 매립지에서 측정을 수행하기에 적합해 보이나, 폐기물 매립지에서 발생하는 메탄 배출량을 산정하기 위해 회전익 UAV의 활용하기에는 아직까지 연구가 부족한 상황이다. 이에 본 연구는 현장 측정 및 데이터 처리 절차를 개발하고, 잠재적 오류 요인을 평가하고, 현장에 직접 적용해 봄으로써 효율적이고 신뢰할 수 있는 산정 방법론을 확립하는 것을 목표로 하였다.

경량 메탄 측정기와 회전익 UAV로 측정 시스템을 구축하고 현장 측정부터 데이터 처리를 포함하는 배출량 산정 절차를 설계하고, 각 과정에 관련된 잠재적 오류 요인을 실험 또는 이론적으로 평가하였다. 측정기 신뢰성 실험에서 측정기가 현장 적용에 충분한 성능을 보임을 확인하였으며, 동역학적으로 검토하여 측정 시스템의 신뢰성을 보장하기 위한 임계 비행속도를 도출하였다. 측정 시스템으로 매립지 현장에서 수집한 메탄 농도에 여러 공간보간법을 적용한 결과, empirical Bayesian kriging이 미측정 지점의 메탄 농도를 가장 잘 예측하는 것으로 나타났다. 바람 측정 방법으로는 UAV의 GPS와 IMU 자료를 이용한 추정 방법을 평가하였다. 근거리 대조 실험에 따르면, 이

방법으로 추정된 풍향, 풍속은 기계식 풍향풍속계로 측정한 풍향, 풍속과 매우 유사하게 나타났다. 현장 측정에서는 이 방법이 고정식 풍향풍속계와 달리 여러 높이에서 바람을 측정할 수 있다는 장점을 확인하였다. 또한, 추정된 매개변수들이 타당한 범위와 상관관계를 보였으므로 현장 측정 결과를 통해 바람 추정 방법의 유효성을 입증할 수 있었다. 오류 요인의 평가 결과 중 일부는 해당 요소의 유효성 확인뿐만 아니라 추후 배출량 산정의 불확도 분석에도 사용되었다.

배출량 산정을 위한 현장 캠페인은 당진시 자원순환센터에서 진행되었다. 일곱 차례의 캠페인을 통해 산정된 메탄 배출량은 406.4–3,640 kg/ha/day로 나타났으며, 이는 IPCC 지침에 따른 모델링 결과와 유사한 수준이었다. 측정 오류, 공간보간 오류 및 바람 변동성을 결합한 총 불확도는 5회에서 6 % 미만, 2회에서 18 % 미만이었다. 대부분 공간보간에 의한 오류가 가장 크게 나타났으나, 근시일 내에 이 방법론의 불확도를 크게 낮출 가능성이 있는 부분은 측정기의 개선일 것이다. 측정면을 잘못 선정하거나 바람이 너무 약해 배출량을 제대로 산정할 수 없었던 경우도 있었다.

본 연구에서는 근거리에서 고해상도 측정을 수행함으로써 성능이 약간 부족한 메탄 측정기를 사용하면서도 산정 불확도를 크게 높이지 않을 수 있었다. UAV에 기반한 바람 추정 방법을 도입해 산정 정확도를 개선하고자 하였다. 여러 차례의 현장 캠페인에서는 방법론의 실제 적용에 필요한 교훈을 얻을 수 있었다. 본 논문에는 방법론, 방법론의 평가, 현장 적용 성공과 실패 사례를 모두 기술하였다. 이 연구는

UAV가 분야를 막론하고 대기 중 측정이나 원격 모니터링에 두루 활용되는 현재 상황에서 UAV를 활용하는 다른 연구자들에게 유용한 정보를 제공할 것으로 기대된다.

주요어 : 온실가스, 탈루 메탄 배출, 무인항공기, 바람 추정방법, 불확도 분석

학 번 : 2018-30709